

**LARGE STRAIN ANALYSIS OF ELECTRO-OSMOSIS
CONSOLIDATION FOR CLAYS**

LARGE STRAIN ANALYSIS OF ELECTRO-OSMOSIS CONSOLIDATION FOR CLAYS

Proefschrift

ter verkrijging van de graad van doctor
aan de Technische Universiteit Delft,
op gezag van de Rector Magnificus prof. ir. K. C. A. M. Luyben,
voorzitter van het College voor Promoties,
in het openbaar te verdedigen op 12 oktober 2015 om 15:00 uur

door

Jiao YUAN

Master of Science in Hydraulic Structure Engineering,
Hohai University, Nanjing, China
geboren te Hunan, China.

Dit proefschrift is goedgekeurd door de promotor:

Prof. dr. M. A. Hicks

Samenstelling promotiecommissie:

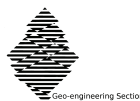
Rector Magnificus,	voorzitter
Prof. dr. M. A. Hicks,	Technische Universiteit Delft, promotor

Onafhankelijke leden:

Prof. dr. ir. T. J. Heimovaara,	Technische Universiteit Delft
Prof. dr. ir. L. J. Sluys,	Technische Universiteit Delft
Prof. dr. A. Scarpas,	Technische Universiteit Delft
Prof. dr. K. Soga,	University of Cambridge
Prof. dr. C. Tamagnini,	Università degli Studi di Perugia

Overige leden:

Prof. dr. C. Jommi,	Technische Universiteit Delft
---------------------	-------------------------------



Keywords: Elasto-plastic, Electro-osmosis consolidation, Finite element analysis, Ground improvement, Large strain

Printed by: Ipskamp Drukker

Author: Jiao YUAN (袁维海)

Copyright © 2015 by Jiao YUAN

Email: j.yuan-1@tudelft.nl; yuanxingyu01@126.com

ISBN 978-94-6186-532-8

An electronic version of this dissertation is available at

<http://repository.tudelft.nl/>.

All rights reserved. No parts of this publication may be reproduced, stored in a retrieval system, or transmitted, in any form or by any means, electronic, mechanical, photocopying, recording, or otherwise, without the prior written permission of the author.

To my parents

CONTENTS

1	Introduction	1
1.1	Background	2
1.2	Motivation	3
1.3	Aims and objectives	3
1.4	Outline of the thesis	4
2	Literature review	7
2.1	Introduction	8
2.2	The mechanics of electro-osmosis	9
2.2.1	Electrical double layer model	10
2.2.2	Electro-chemical reaction	12
2.2.3	Multi-physical coupled flows in electro-osmosis	12
2.3	Electro-osmosis consolidation of soil	14
2.3.1	Esrig's 1D consolidation theory	15
2.3.2	Lewis's 2D FEM solution	15
2.4	Field applications of electro-osmosis	17
2.5	Laboratory studies of electro-osmosis	18
2.5.1	Voltage and electric current density	18
2.5.2	Intermittent current and polarity reversal in electro-osmosis	18
2.5.3	Chemical treatment to improve electro-osmosis consolidation	19
2.5.4	New advances in electrode materials for use in electro-osmosis	19
2.5.5	Effect of zeta potential	20
2.5.6	Using electro-osmosis dewatering in different kinds of materials	21
2.6	Summary	22
3	Large strain elastic electro-osmosis consolidation of clays	23
3.1	Introduction	24
3.2	Theoretical and governing formulations	25
3.2.1	Kinematics and deformations	25
3.2.2	Mechanical equilibrium and effective stress concept	26
3.2.3	Pore water transport	28
3.2.4	Electrical transport	29
3.2.5	Final governing equations	29
3.3	Application of finite element method	29
3.3.1	Finite element discretization	29
3.3.2	Time stepping and solution procedure	31

3.4	Validation and numerical examples	32
3.4.1	1D verification	32
3.4.2	1D electro-osmosis consolidation behaviour	35
3.4.3	1D consolidation as a function of k_{eo}/k_w	37
3.4.4	2D consolidation behaviour of electro-osmosis	40
3.5	Conclusions.	42
4	Numerical simulation of elasto-plastic electro-osmosis consolidation at large strain	45
4.1	Introduction	46
4.2	Theoretical background and governing equations	47
4.2.1	Modelling framework	47
4.2.2	Mechanical equilibrium	48
4.2.3	Balance of water mass	49
4.2.4	Balance of electric charge	49
4.3	Constitutive equations	49
4.3.1	Solid skeleton	50
4.3.2	Pore water transport	51
4.3.3	Electric charge transport	52
4.3.4	Void ratio and conductivity/permeability updates	53
4.3.5	Final governing equations	53
4.4	Numerical simulations	54
4.4.1	Electro-osmosis test on a colloidal silica column.	54
4.4.2	1D electro-osmosis consolidation	56
4.4.3	2D elasto-plastic electro-osmosis consolidation	59
4.4.4	Numerical study of a field test	64
4.5	Conclusions.	68
5	Large strain elasto-plastic electro-osmosis consolidation of unsaturated clays	71
5.1	Introduction	72
5.2	Governing equations at large strain	73
5.2.1	Basic assumptions	73
5.2.2	Kinematic and deformation equations	73
5.2.3	Balance laws	74
5.2.4	Equilibrium equations	75
5.2.5	Mass balance equations	76
5.2.6	Electric current density balance equation	78
5.2.7	Final governing equations	79
5.3	Finite element formulation	79
5.3.1	Weak forms	79
5.3.2	Spatial and time discretization	81
5.4	Validation and numerical simulations	82
5.4.1	Validation of the numerical model	82
5.4.2	Numerical examples and parametric study	85
5.5	Conclusions	98

6	Numerical evaluation of optimal approaches for electro-osmosis consolidation	101
6.1	Introduction	102
6.2	Methodology	103
6.2.1	Modelling framework	103
6.2.2	Power consumption and energy index	103
6.3	Numerical examples	104
6.3.1	Example 1: Electrode configurations	104
6.3.2	Example 2: Current intermittence	107
6.3.3	Example 3: Current reversal	109
6.4	Results and discussion	109
6.4.1	Electrode configurations	109
6.4.2	Current intermittence	113
6.4.3	Current reversal	116
6.5	Conclusions.	120
7	Conclusion and recommendations	123
7.1	Conclusions.	124
7.2	Recommendations for future work	126
	References	129
A	Matrices and vectors for large strain formulations	139
B	Coefficient matrices and load vectors	141
	Summary	143
	Samenvatting	145
	Acknowledgments	147
	Curriculum Vitae	149
	List of publications	151

1

INTRODUCTION

1.1. BACKGROUND

Soft clays are commonly found in many parts of the world. As the population increases, the demand for new land increases at a similar rate; therefore constructions on soft clay soils with low hydraulic permeability and stiffness are inevitable. For example, in recent years reclamation of coastal land for industrial use is becoming popular in Chinese coastal areas. In order to prevent excessive settlements, increase bearing capacities and control seepage, the need for soil improvement techniques becomes significant. Conventional methods such as surcharge or preloading, a combination of preloading with prefabricated vertical drains, and vacuum preloading have been used for many decades to minimize this problem. However, when dealing with deposits of high clay content a long time may be needed to complete the primary consolidation. Furthermore, the clay may be too soft to apply preloading and the use of fill may not be economically feasible. In view of these deficiencies a novel method to accelerate consolidation like electro-osmosis is needed.

Electro-osmosis is found to be more effective in clayey soils because the electro-osmosis permeability is independent of the grain size. Due to the existing negative charges on the surface of the clay particles, the pore water adjacent to the clay particles would have positive charges which move to the cathode when a direct current voltage is applied to the soil via electrodes. The movement of the pore water towards to the cathode dragged by charged particles is known as electro-osmosis flow. If drainage is provided at the cathode and prohibited at the anode, negative pore water pressures will be developed near the anode, resulting in an increase in the effective stress of the soil skeleton. In addition, electro-chemical reactions associated with the electro-osmosis process alter the physical and chemical properties of the soil and lead to further consolidation.

Electro-osmosis was first introduced into geotechnical engineering by [Casagrande \(1949\)](#). Since then, successful field applications of electro-osmosis consolidation have been reported in the literature, such as for improving friction pile capacity ([Soderman and Milligan, 1961](#); [Milligan, 1995](#)), strengthening soft sensitive clays ([Bjerrum et al., 1967](#)), stabilizing excessive foundation deformations ([Fetzer, 1967](#)), strengthening and stabilization of soft clays ([Chappell and Burton, 1975](#); [Casagrande, 1983](#); [Burnotte et al., 2004](#)), consolidation of marine sediments for land reclamations ([Lo et al., 2000](#); [Chew et al., 2004](#)), and dewatering of mine tailings ([Lockhart and Hart, 1988](#); [Shang and Lo, 1997](#); [Fourie et al., 2007](#)). At the laboratory scale, there have been a lot of investigations to study the suitability of its application, the anticipated effects of the treatment, its efficiency and effectiveness, and different treatment costs ([Casagrande, 1952](#); [Nicholls and Herbst, 1967](#); [Gray, 1970](#); [Wan and Mitchell, 1976](#); [Chen et al., 1996](#); [Veal et al., 2000](#); [Mohamedelhassan and Shang, 2001](#); [Fourie et al., 2007](#); [Chien and Ou, 2011](#); [Karunaratne, 2011](#); [Estabragh et al., 2014](#)).

[Esrig \(1968\)](#) first developed a one dimensional analytical model to predict the development of pore water pressure by electro-osmosis. Based on Esrig's equation, many analytical solutions of electro-osmosis consolidation have been developed ([Wan and Mitchell, 1976](#); [Shang, 1998a,b](#)). However, these analytical formulations have been for limited boundary conditions and geometries. Moreover, the nonlinearity of the transport parameters were not accounted for. Later, some numerical models ([Lewis and Garner, 1972](#); [Rittirong and Shang, 2008](#)) were also developed, to simulate electro-osmosis

consolidation problems with complicated geometries and boundary conditions. Although these models were able to predict the coupling effects of the electric field and hydraulic gradients during electro-osmosis consolidation, the force equilibrium for the soil was still included implicitly in the formulation of the pore water transport, following Terzaghi's consolidation approach, and no constitutive relationship was incorporated to account for the nonlinear stress–strain behaviour of the soil skeleton. Finally, large strain has not been considered in the numerical modelling of electro-osmosis consolidation. Large strain consolidation refers to an advanced method of modelling the consolidation behaviour of soil experiencing large deformations. Soft clays are generally deposited at low strength, high compressibility and with a high natural moisture content, and can consolidate significantly thereafter. Small strain consolidation analysis is unsuitable when considering very large deformations.

The purpose of this thesis is to develop a numerical model which can overcome the above mentioned shortcomings. A fully coupled multi-physics finite element formulation for electro-osmosis consolidation in multi-dimensional domains at large strains is presented, in conjunction with elasto-plastic constitutive models for modelling nonlinear stress–strain behaviour. Some empirical expressions are also incorporated to consider the time dependency of the transport parameters.

1.2. MOTIVATION

The mechanical behaviour of the soil skeleton is the major concern when applying a soil improvement method; however, the existing models of electro-osmosis consolidation are not capable of simulating directly the force equilibrium to solve boundary value problems. Moreover, only a linear elastic constitutive relationship for the soil at small strain is included in the existing theories. Furthermore, a multi-dimensional model is needed to simulate complicated geometries and boundary conditions and varying nonlinear material properties, and to optimize approaches, which are crucial points in the engineering design of field applications. Previously, field applications were designed based on laboratory experiments, which are both time and money consuming. Therefore, this research is motivated by the desire to develop a more realistic numerical tool which addresses the main features of electro-osmosis consolidation, and that has potential use in the design and optimization of field applications.

1.3. AIMS AND OBJECTIVES

The overall aim of this research is to develop a numerical model for simulating multi-dimensional and fully coupled multi-physics electro-osmosis consolidation, including the elasto-plastic behaviour of soil and time dependent transport parameters at large strain. As this constitutes a pioneering effort in the modelling of electro-osmosis consolidation, the research progresses from a linear elastic large strain model to a nonlinear elasto-plastic large strain model.

The further objectives of this research are to:

- develop a finite element formulation for large strain electro-osmosis consolidation;

- incorporate elasto-plastic soil models, such as the Modified Cam Clay model for saturated conditions and the Barcelona Basic Model for unsaturated conditions;
- incorporate nonlinear transport parameters (i.e. void ratio dependent conductivity and permeability for saturated conditions; and degree of water saturation dependent conductivity and permeability for unsaturated conditions);
- implement the governing formulation and constitutive models within a finite element code;
- verify and evaluate the numerical model against analytical solutions and data from field case studies;
- identify and evaluate optimum electrode configurations, and approaches such as current intermittence and current reversal, which are often used in laboratory and field tests.

1.4. OUTLINE OF THE THESIS

The thesis contains 7 chapters.

Chapter 2 presents the literature review of the principles of electro-osmosis consolidation. In this chapter several analytical and numerical models for predicting electro-osmosis consolidation, considering the coupling between hydraulic and electrical gradients, are introduced first. Then, field applications of electro-osmosis consolidation are briefly reviewed. Finally, laboratory studies of electro-osmosis are summarized.

Chapter 3 presents the theoretical background of an elastic electro-osmosis consolidation model for saturated soils at large strain. The model considers volumetric strains induced by changes in both the hydraulic and electric driven pore water flows. The proposed model is first verified against a one dimensional analytical solution for electro-osmosis consolidation to demonstrate its accuracy. Then, various numerical examples are investigated to highlight the differences between models based on small strain and large strain theories.

In Chapter 4 the Modified Cam Clay model is employed to describe the elasto-plastic behaviour of clay during a saturated electro-osmosis process at large strain, and some empirical expressions are used to consider the time dependency of the transport parameters. The proposed model is verified via comparison with data from a large strain electro-osmosis laboratory test. Various numerical examples are investigated to study the deformation characteristics and time dependent evolution of the pore water pressure. Finally, a well-documented field application of electro-osmosis is simulated to provide further verification.

Chapter 5 describes a numerical model of elasto-plastic electro-osmosis consolidation for unsaturated clays experiencing large strain. The gas generation at the anode is considered in the governing equations, and the Barcelona Basic Model is employed within the formulation to simulate the elasto-plastic mechanical behaviour of unsaturated clays. The accuracy of the proposed model is evaluated by validating against two well-known numerical examples. Two further examples are investigated to study the capability of the computational algorithm in modelling multiphase flow in electro-osmosis consolidation.

In Chapter 6, the numerical models developed in the previous chapters are used to identify and evaluate optimum electrode configurations, and approaches such as current intermittence and current reversal. The numerical results indicate the need to optimize each approach for a particular application according to the primary objective of the project. Furthermore, the efficiency and economy of the intermittent and reversal currents are shown to be better than that of the continuous current.

Chapter 7 gives a summary of the thesis, the main conclusions and recommendations for future research.

2

LITERATURE REVIEW

2.1. INTRODUCTION

In a porous medium, electro-osmosis is the water flow from the positive electrode to the negative electrode when an electrical gradient is applied. Geotechnical and geo-environmental engineers have been interested in electro-osmosis for many years as a method of soil improvement, which includes electro-osmosis dewatering, ion injection, contaminant removal, electro-bioremediation and electro-chemical remediation. In particular, electro-osmosis as a method of ground improvement for soft soil is receiving much attention. When traditional ground improvement techniques, such as surcharge pre-loading, vertical drains and vacuum pre-loading are not appropriate for a particular situation, innovative techniques such as electro-osmosis need to be considered.

Following the pioneering work of [Casagrande \(1949\)](#) in the 1940s for accelerating the consolidation of natural soft clays, electro-osmosis dewatering has generated much interest in geotechnical engineering. Electro-osmosis dewatering provides a potentially attractive alternative technique for dewatering. Traditional dewatering techniques for soft clay, including vacuum preloading, preloading, well-point dewatering, and vibration compaction, are useful in some ordinary low permeability soft clays. But, when dealing with soft clay with a permeability coefficient less than 10^{-9} m/s, or even less than 10^{-10} m/s, these methods are ineffective. Because the electro-osmosis flow rate is independent of the pore size, it can enhance the transport of water in a low permeability soil. Hence electro-osmosis is a good choice as a kind of special soft ground treatment method.

Electro-osmosis has been successfully applied in various fields as an economical and time saving method, for example to improve friction pile capacity ([Soderman and Milligan, 1961](#); [Milligan, 1995](#)), to control the pore water at excavation sites ([Bjerrum et al., 1967](#)), to stabilize excessive foundation deformations ([Fetzer, 1967](#)), for the strengthening and stabilization of soft clays ([Casagrande, 1983](#); [Burnotte et al., 2004](#)), for the consolidation of marine sediments for land reclamations ([Lo et al., 2000](#)), and for the dewatering of mine tailings ([Lockhart and Hart, 1988](#); [Shang and Lo, 1997](#); [Fourie et al., 2007](#)). At the same time, numerous laboratory studies have been conducted to understand the suitability of its application, the anticipated effects of the treatment, its efficiency and effectiveness, and different treatment costs. These papers include studies of the optimal voltage gradient and current density ([Casagrande, 1952](#); [Nicholls and Herbst, 1967](#); [Veal et al., 2000](#)), the effects of polarity reversal and current intermittence ([Chappell and Burton, 1975](#); [Wan and Mitchell, 1976](#); [Lockhart and Hart, 1988](#); [Mohamedelhassan and Shang, 2001](#)), chemical treatment to improve electro-osmosis consolidation ([Gray, 1970](#); [Alshawabkeh and Sheahan, 2003](#); [Burnotte et al., 2004](#); [Asavadorndeja and Glawe, 2005](#); [Chien and Ou, 2011](#)), different electrode materials ([Segall and Bruell, 1992](#); [Mohamedelhassan and Shang, 2001](#); [Bergado et al., 2003](#); [Fourie et al., 2007](#); [Jones et al., 2011](#)) and the effect of zeta potential ([Chen et al., 1996](#); [Shang and Lo, 1997](#); [West and Stewart, 2000](#)).

However, as noted by some researchers, despite the reporting of numerous successful laboratory studies and case records, the results have generally been such that electro-osmosis is today very seldom used in geotechnical engineering practice. This is mainly because, during the electro-osmosis dewatering process, a larger voltage drop may be generated near the electrode because of serious corrosion of the electrodes (particularly the anode), so that little electrical energy is used on the soil itself. Sometimes, these

factors have led to the electro-osmosis effect not being significant in engineering applications, and they also make electro-osmosis dewatering techniques highly power consuming and inefficient. Other obstacles to the widespread adoption of electro-osmosis dewatering techniques are the limited area of improvement and lack of proven practical implementations.

Compared to the laboratory studies and case records, the theoretical analysis and numerical simulation of electro-osmosis dewatering are far less developed. Electro-osmosis is a very complicated process; it is actually a combination of a series physical, chemical and electrical reactions. The mechanical behaviour, hydraulic and electric properties of a soil are changing rapidly during the electro-osmosis process. This all makes electro-osmosis hard to describe and simulate.

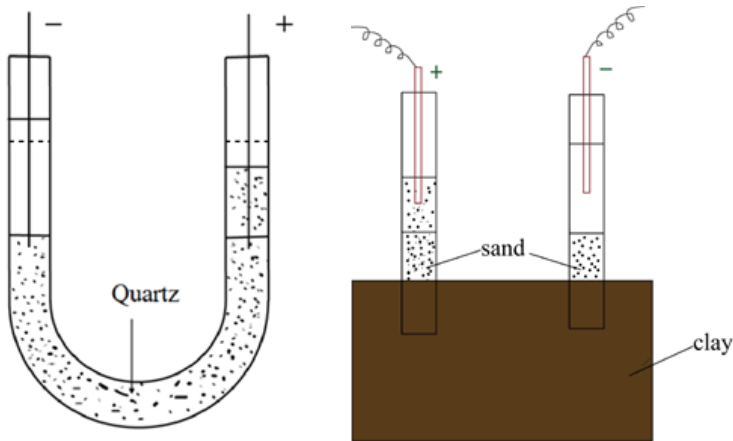


Figure 2.1: Schematic of Reuss's experimental set-ups.

2.2. THE MECHANICS OF ELECTRO-OSMOSIS

In 1809, Reuss, a researcher from Russia, was the first to observe water flow in soils as a result of a direct electric current passing through it (Mitchell, 1993). His experimental set-ups are shown in Figure 2.1, and include a U shaped glass tube containing water and quartz powder (Figure 2.1 left). After putting electrodes into the water and applying a direct current for a moment, he found that the water in the left tube (with the cathode) rose by 2.5 cm; the water in the right tube decreased by the same amount. The phenomenon of pore fluid flow through a porous material due to the application of a direct current is called electro-osmosis.

In the second experimental set-up, shown in the right side of Figure 2.1, Reuss inserted two glass tubes into clay; he then put a layer of sand at the bottom of the two tubes and later filled the tubes with water. After putting electrodes into the water and applying direct current for a moment, he found that the surface of the clay in the left tube rose, and, at the same time, a lot of clay particles migrated into the water. The phenomenon of the dispersed clay particles migrating under the electric field is called electrophoresis. Electro-osmosis and electrophoresis occurred simultaneously, and is

collectively referred to as electro-kinetic.

2.2.1. ELECTRICAL DOUBLE LAYER MODEL

Generally, the soil surface will possess a fixed surface charge when it is brought into contact with water. The major contribution to this surface charge in soil comes from clay particles, whose faces can be charged as a result of several mechanisms, including isomorphous substitution, adsorption of charged ions, and proton association/dissociation reactions. The first layer of cations is considered immobile, whereas the second layer is composed of ions attracted to the surface charge via the Coulomb force, electrically screening the first layer. This second layer is loosely associated with the surface, because it is made of free ions which move in the fluid under the influence of electric attraction and thermal motion, rather than being firmly anchored. It is considered mobile and is thus called the diffuse layer. The charged solid–liquid interfacial region is called the double layer. In this region the fluid possesses a charge density that balances the surface charge on the solid (shown in Figure 2.2).

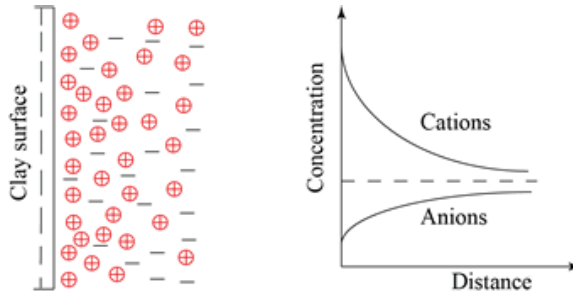


Figure 2.2: Schematic of electrical double layer model.

Since Quincke first described the electrical double layer model in 1861, many researchers have done a lot of work to improve the model. [Von Helmholtz \(1879\)](#) treated the double layer mathematically as a simple capacitor, based on a physical model in which a single layer of ions is adsorbed at the surface and the surface charge is balanced by a layer of oppositely charged ions. Later, [Gouy \(1910\)](#) and [Chapman \(1913\)](#) made significant improvements by introducing a diffuse layer that can be described by a Poisson-Boltzmann distribution, in which the electric potential decreases exponentially away from the surface. However, the Gouy–Chapman model fails for highly charged double layers. In order to resolve this problem [Stern \(1924\)](#) suggested the combination of the Helmholtz and Gouy–Chapman models, giving an internal Stern layer and an outer diffuse layer (shown in Figure 2.3).

The movement of liquid results from the applied electric field acting on the charged interface between the water and the clay. As shown schematically in Figure 2.4, the applied electric field produces a force on the charged fluid in the double layer, which causes the cations in the mobile parts of the double layer near the surface of the clay particles to migrate to the cathode and drag water with them, causing water flow towards the cathode.

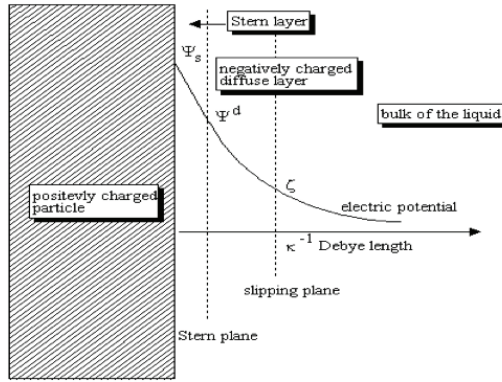


Figure 2.3: Schematic of Stern–Gouy double layer model.

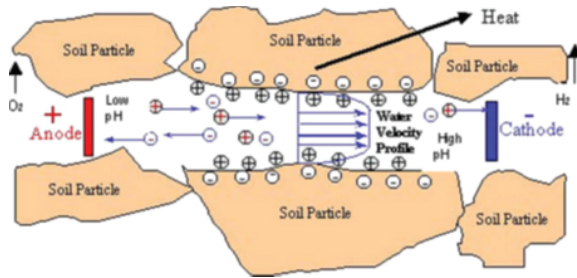


Figure 2.4: Schematic of electro-osmosis in soil (Jones et al., 2011).

In 1879, Helmholtz demonstrated a model to describe the principle of electro-osmosis flow in fine soil (Von Helmholtz, 1879). The electro-osmosis flow in a liquid filled capillary can be expressed by

$$q_e = \frac{EDr^2\zeta}{4\eta} \quad (2.1)$$

where E is the electric field intensity (V/m), D is the permittivity of the pore water, η is the liquid viscosity of water, r is the radius of the capillary and ζ is the zeta potential.

Smoluchowski (1921) developed the classical model to a more common situation; his formulation of the problem being based on the assumption of a large electro-kinetic diameter. The contribution due to the double layer thickness is neglected and the electro-osmosis flow can then be expressed by

$$v_e = \frac{ED\zeta}{4\pi\eta} \quad (2.2)$$

This is called the Helmholtz–Smoluchowski model (H–S model), and is a commonly accepted model for interpreting electro-osmosis in soils (Mitchell, 1993).

2.2.2. ELECTRO-CHEMICAL REACTION

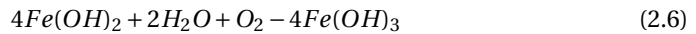
Some of the physico-chemical processes that take place during the electro-osmosis treatment of clay include: simple ion exchange, ion diffusion, the buildup of osmotic and pH gradients, desiccation, decomposition of primary soil minerals, precipitation of secondary minerals, electrolysis, hydrolysis, oxidation, reduction, physical and chemical adsorption, and reorientation of clay particles or fabric changes. The electro-chemical reactions during this process are quite complex, but the main reactions can be simplified below. At the anode:



The presence of anions in the soil-water electrolyte system can react with freed H^+ to form acids, and oxygen gas will also be generated. At the same time, high acidity and oxidation can cause rapid deterioration of the anodes, altering the anode to the aluminum or iron form depending on the anode material as follows:



Then, iron precipitates are formed as follows (Segall and Bruell, 1992):



Iron hydroxide is a kind of natural cementing agent, which will lead to cementation between soil particles strengthening the soil mass. Chlorine may also form in a saline environment and this is highly probable in local marine clay because of its contact with seawater. The reaction is expressed by



At the cathode, hydrogen gas is generated by hydrolysis:



The generated OH^- will cause the pH value to rise and alkaline conditions will develop in an area around the cathode. Some alumina and silica may go into solution in this high pH environment. Note that the presence of extraneous ions such as Fe^{2+} or Cl^- may not be favourable for environmental reasons.

2.2.3. MULTI-PHYSICAL COUPLED FLOWS IN ELECTRO-OSMOSIS

Mitchell (1991) described several types of direct and coupled flows through soil. When a soil mass is subjected to various kinds of gradients, such as hydraulic, electrical, chemical and thermal gradients, things in the soil mass will move. Weak and compressible soil skeletons can be deformed by gradients, while strong and incompressible soil skeletons experience mass and energy flow through them. One type of gradient can cause flow of the same type, for example, a hydraulic gradient can cause hydraulic flow; furthermore, it is also well known that a gradient of one type may cause a flow of another type, such as a hydraulic flow being caused by an electrical gradient. Electro-osmosis flow is a kind of coupled flow.

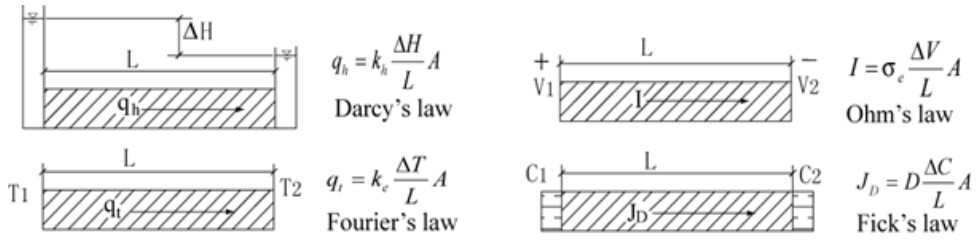


Figure 2.5: Four types of direct flow through a soil mass (Mitchell, 1993).

As mentioned in the previous sections, electro-osmosis consolidation is quite a complex process. Some electro-physico-chemical reactions take place during the electro-osmosis consolidation. There are at least four kinds of direct flow in the electro-osmosis process; they are hydraulic flow, electric flow, thermal flow and chemical flow.

As shown in Figure 2.5, Darcy's, Fourier's, Ohm's and Fick's laws are used to describe water, heat, electrical and chemical flows, respectively, due to gradients of the same type. Assuming that the flow process does not change the state of the soil, each flow rate J_i is linearly related to its corresponding driving force X_j according to

$$J_i = L_{ij} X_j \quad (2.9)$$

in which L_{ij} is the conductivity coefficient for the flow. If $i = j$, it is direct flow and Eq. (2.9) can be written as below:

for water flow

$$q_w = k_w i_w \quad (2.10)$$

for electrical flow

$$I = k_{\sigma e} i_e \quad (2.11)$$

for heat flow

$$q_t = k_t i_t \quad (2.12)$$

for chemical flow

$$J_D = D i_c \quad (2.13)$$

where q_w , I , q_t , J_D are the water, electrical, heat and chemical flow rates, respectively. The coefficients k_w , $k_{\sigma e}$, k_t and D are the hydraulic, electrical, and thermal conductivities, and the diffusion coefficient, respectively.

As discussed above, one type of gradient may cause another type of flow. Hence considering coupled flow, Eq. (2.9) can be written as

$$\begin{aligned} q_w &= L_{11} \nabla H + L_{12} \nabla E + L_{13} \nabla T + L_{14} \nabla C \\ I &= L_{21} \nabla H + L_{22} \nabla E + L_{23} \nabla T + L_{24} \nabla C \\ q_t &= L_{31} \nabla H + L_{32} \nabla E + L_{33} \nabla T + L_{34} \nabla C \\ J_D &= L_{41} \nabla H + L_{42} \nabla E + L_{43} \nabla T + L_{44} \nabla C \end{aligned} \quad (2.14)$$

However, in the case of electro-osmosis, not all types of flow are necessarily influential, and so some of the gradients may be considered not so important. For example, if simple electro-osmosis under isothermal conditions and with no chemical reactions is considered, then Eq. (2.9) can be written as

$$q_w = k_w i_w + k_{eo} i_e \quad (2.15)$$

$$I = k_{\sigma w} i_w + k_{\sigma e} i_e \quad (2.16)$$

where k_{eo} is the electro-osmosis conductivity, $k_{\sigma w}$ is the electrical conductivity due to hydraulic flow, and some of the coupling flows may be significantly smaller than the direct flow and therefore assumed to be zero. In this case, the coupling coefficient $k_{\sigma w}$ can be considered to be zero, since normally the electrical current caused by hydraulic flow is extremely small, so Eq. (2.16) can be simplified as

$$I = k_{\sigma e} i_e \quad (2.17)$$

Eqs. (2.15) and (2.17) are the two most common equations in electro-osmosis, considering that the water flow is mainly caused by both the hydraulic gradient and electrical potential gradient.

2.3. ELECTRO-OSMOSIS CONSOLIDATION OF SOIL

Due to its demonstrated practical significance, the electro-osmosis consolidation of soil has received considerable interest in the past, and the consolidation theory of electro-osmosis has been studied for several decades (Corapcioglu, 1991). A large part of the early literature on electro-osmosis is associated with efforts to describe the performance of field techniques used in soil stabilization processes; for example, Casagrande (1949) was the first to apply electro-osmosis in soil consolidation.

Casagrande found, through a lot of experimental work, that the water flow towards the cathode is proportional to the electrical gradient applied to the soil, so that the electro-osmosis flow rate can be expressed by (Casagrande, 1952)

$$Q_{eo} = k_{eo} \frac{V}{L} A \quad (2.18)$$

where Q_{eo} is the electro-osmosis flow rate under the voltage gradient, V/L is the electric gradient and A is the cross-sectional area.

Based on Casagrande's work, the theory of one dimensional (1D) electro-osmosis consolidation was first developed by Esrig (1968), and Wan and Mitchell (1976) presented an analytical solution for 1D electro-osmosis consolidation with preloading. Feldkamp and Belhomme (1990) later derived a solution for large strain 1D electro-osmosis consolidation. Lewis and his co-workers (Lewis and Garner, 1972; Lewis and Humphe-son, 1973) presented a two dimensional (2D) finite element solution for modelling the coupling effect of the electric and hydraulic gradients. Shang (1998a,b) developed a 2D analytical model combining preloading and the electro-osmosis consolidation of clay soils. Rittirong and Shang (2008) presented a 2D finite difference model to analyse indirectly the subsurface settlement and undrained shear strength. Iwata and Jami (2010)

presented a numerical model to simulate the combined electro-osmosis dewatering and mechanical response, using the Terzaghi-Voigt combined model to consider creep deformation.

In the following two sections, Esrig's 1D analytical solution and the 2D finite element solution developed by Lewis are introduced in detail.

2.3.1. ESRIG'S 1D CONSOLIDATION THEORY

Esrig (1968) developed a 1D electro-osmosis consolidation theory, based on the hypothesis of a uniform electric field and that the flow of fluid due to electrical and hydraulic gradients may be superimposed to obtain the total flow. Based on these assumptions, the total fluid flux q can be expressed by

$$q = q_w + q_{eo} = -k_w \nabla H - k_{eo} \nabla V \quad (2.19)$$

where H is the hydraulic head and V is the voltage. The maximum negative pore water pressure (assuming that the cathode and anode are at the same level) that can be developed at the anode, u , is defined by

$$u = \frac{k_{eo}}{k_w} \gamma_w V \quad (2.20)$$

where γ_w is the unit weight of water.

For the 1D case, the flow equation can be written as

$$q = -\frac{k_w}{\gamma_w} \frac{\partial u}{\partial x} - k_{eo} \frac{\partial V}{\partial x} \quad (2.21)$$

Introduction of this equation, in place of Darcy's law, in the derivation of the diffusion equation governing consolidation in one-dimensional flow, leads to

$$\frac{k_w}{\gamma_w} \frac{\partial^2 u}{\partial x^2} + k_{eo} \frac{\partial^2 V}{\partial x^2} = m_v \frac{\partial u}{\partial t} \quad (2.22)$$

where m_v is the coefficient of compressibility.

2.3.2. LEWIS'S 2D FEM SOLUTION

In the early 1970s, Lewis and his co-workers (Lewis and Garner, 1972; Lewis and Humpherson, 1973) presented a numerical solution for electro-osmosis consolidation, which considers the coupling effect of the electric and hydraulic gradients.

The 2D flow of fluid in a porous medium is given by Darcy's law as

$$\begin{aligned} q_{wx} &= -k_{wx} \frac{\partial H}{\partial x} \\ q_{wy} &= -k_{wy} \frac{\partial H}{\partial y} \end{aligned} \quad (2.23)$$

where q_{wx} and q_{wy} are the two component discharge velocities caused by the hydraulic gradients $\frac{\partial H}{\partial x}$ and $\frac{\partial H}{\partial y}$ respectively, and k_{wx} and k_{wy} are the hydraulic conductivities in

the co-ordinate directions. Based on Casagrande's work (Casagrande, 1952), the electro-osmosis flow can be expressed by

$$\begin{aligned} q_{eox} &= -k_{eox} \frac{\partial V}{\partial x} \\ q_{eoy} &= -k_{eoy} \frac{\partial V}{\partial y} \end{aligned} \quad (2.24)$$

where q_{eox} and q_{eoy} are the component discharge velocities caused by the electrical potential gradients $\frac{\partial V}{\partial x}$ and $\frac{\partial V}{\partial y}$ respectively, and k_{eox} and k_{eoy} are the electro-osmosis conductivities of the soil in the co-ordinate directions.

Based on the same assumptions as used by Esrig, the combined fluid flow can be given by

$$\begin{aligned} q_x &= -k_{wx} \frac{\partial H}{\partial x} - k_{eox} \frac{\partial V}{\partial x} \\ q_y &= -k_{wy} \frac{\partial H}{\partial y} - k_{eoy} \frac{\partial V}{\partial y} \end{aligned} \quad (2.25)$$

Assuming that, in a similar manner, the two dimensional flow of electric current is governed by Ohm's law, then

$$\begin{aligned} j_{ex} &= -k_{\sigma ex} \frac{\partial V}{\partial x} \\ j_{ey} &= -k_{\sigma ey} \frac{\partial V}{\partial y} \end{aligned} \quad (2.26)$$

where j_{ex} and j_{ey} are the current densities, and $k_{\sigma ex}$ and $k_{\sigma ey}$ are the electric conductivities in the respective co-ordinate directions. As mentioned before, the hydraulic gradient can also cause electric flow, as governed by Quincke's law:

$$\begin{aligned} j_{wx} &= -G_x \frac{\partial H}{\partial x} \\ j_{wy} &= -G_y \frac{\partial H}{\partial y} \end{aligned} \quad (2.27)$$

where j_{wx} and j_{wy} are the streaming currents produced due to the hydraulic gradients in the respective co-ordinate directions. G may be expressed as the current flux produced per unit hydraulic gradient.

Hence, the coupled equations of current flow are

$$\begin{aligned} j_x &= -k_{\sigma x} \frac{\partial V}{\partial x} - G_x \frac{\partial H}{\partial x} \\ j_y &= -k_{\sigma y} \frac{\partial V}{\partial y} - G_y \frac{\partial H}{\partial y} \end{aligned} \quad (2.28)$$

For a fully coupled system the continuity equation gives

$$\begin{aligned} \nabla \cdot \mathbf{q} &= -m_v \gamma_w \frac{\partial H}{\partial t} \\ \nabla \cdot \mathbf{j} &= -\frac{\partial Q}{\partial t} \end{aligned} \quad (2.29)$$

where Q is the electric charge density. Combined with Eqs. (2.25), (2.28) and (2.29), results in

$$\begin{aligned} \frac{\partial}{\partial x}(k_{wx} \frac{\partial H}{\partial x} + k_{eox} \frac{\partial V}{\partial x}) + \frac{\partial}{\partial y}(k_{wy} \frac{\partial H}{\partial y} + k_{eoy} \frac{\partial V}{\partial y}) &= m_v \gamma_w \frac{\partial H}{\partial t} \\ \frac{\partial}{\partial x}(G_x \frac{\partial H}{\partial x} + k_{\sigma ex} \frac{\partial V}{\partial x}) + \frac{\partial}{\partial y}(G_y \frac{\partial H}{\partial y} + k_{\sigma ey} \frac{\partial V}{\partial y}) &= -\frac{\partial Q}{\partial t} \end{aligned} \quad (2.30)$$

These two equations are the governing equations of the completely coupled fluid flow and electrical flow in electro-osmosis consolidation, in which both the hydraulic and electric properties are time dependent, and they may be solved by the finite element method.

2.4. FIELD APPLICATIONS OF ELECTRO-OSMOSIS

Large-scale field applications of electro-osmosis are still very seldom, partly due to its being economically impractical in some situations (primarily due to the high energy consumption) and partly due to uncertainty in its practical effectiveness. This section reviews several successful projects reported by researchers. They reflect the application of electro-osmosis to problems of a varying nature, including the use of electro-osmosis treatment in different soil types.

The first application of electro-osmosis to improve friction pile capacity in soft clay and silt soils was reported in [Soderman and Milligan \(1961\)](#) and [Milligan \(1995\)](#). The main problem encountered was founding the Big Pic River Bridge on around 100 m of soft varved clay and loose silt deposits. Due to the presence of an excess hydrostatic head at depth, the capacity of long friction piles was markedly less than that of short piles. Consequently, it was decided to found the structure on short, steel H-section piles within the upper clay and to apply electro-osmosis treatment.

[Bjerrum et al. \(1967\)](#) reported field electro-osmosis treatment as a measure to improve Norwegian quick clay in a basement excavation for a sewage treatment plant. With the low shear strength of the quick clay, it would have caused a bottom heave failure in a deep excavation. In order to carry out the excavation, the shear strength of the clay had to be increased; a total of 190 electrodes of 10 m length and 19 mm diameter were installed to improve the quick clay, over 10 m depth and covering a test area of 200 m².

[Lo et al. \(1991b\)](#) used fieldwork to assess the effectiveness of electro-osmosis in improving soft sensitive clay with an original average shear strength of 20 kPa. Perforated copper pipes had a varnish coating over the top 1.8 m were served as the electrodes. Nine electrodes were installed to study the effect of spacing and polarity reversal on clay treated by electro-osmosis, at two spacings of 6 m and 3 m. The experiment lasted for 32 days and the voltage was applied to the 1.8-5.8 m depth of soft clay. Ground settlement, vane shear strength and voltage distributions were measured, before, during, and after the electro-osmosis treatment.

[Burnotte et al. \(2004\)](#) considered the electro-osmosis treatment of soft clay, with chemical treatment to improvement the soil-electrode contact, for a site in in Canada. The large field demonstration test involved over 700 m³ of clay being treated by means of 24 electrodes. In order to improve the effectiveness of the electro-osmosis consolidation, the 12 anodes were treated by chemical injection before the test. One of the purposes of

the field test was to demonstrate that the clay foundation of an existing embankment could be consolidated by electro-osmosis, to eliminate long-term settlements adjacent to a bridge or overpass founded on piles.

Chew et al. (2004) reported a field trial for soft clay stabilization using electro-osmosis consolidation in Singapore. A large area of dredge reclaimed marine soft clay land was treated by installing electrical vertical drains (EVD), and the feasibility of electro-osmosis on the consolidation of a soft marine clay was examined. The results illustrated that the soft clay, beneath the 18 m of sand fill, could be reached effectively by EVD. The shear strength improved significantly after electro-osmosis treatment. The time taken by the conventional method (prefabricated vertical drains (PVD)) to achieve the equivalent shear strength would have been 10 times longer compared to EVD.

2.5. LABORATORY STUDIES OF ELECTRO-OSMOSIS

Since the 1960s, laboratory devices have been constructed to measure electro-osmosis in clays, although, due to their mechanical and hydraulic properties, clays are not easy to work with. Numerous laboratory tests have been carried out to study the required parameters or to provide necessary information for assessing the potential field application. Fundamental studies of electro-osmosis include investigating the effects of electricity on the mechanical and physical-chemical properties of soil. The possibility for cost savings in practice, through optimization of energy consumption with respect to strength gain in soil by using the techniques of polarity reversal and current intermittence, as well as varying the materials of the electrodes, have also been investigated.

2.5.1. VOLTAGE AND ELECTRIC CURRENT DENSITY

Voltage gradient and current density are the main factors that have affected the performance of electro-osmosis dewatering. The electro-osmosis drainage volume is proportional to the voltage gradient (Casagrande, 1952), and so some extremely high voltage gradients were used in early laboratory research, e.g. 330 V/m (Esrig, 1968), 140 V/m (Arnold, 1973), and also current densities up to 7.3 A/m^2 (Bjerrum et al., 1967). As mentioned by Bjerrum et al. (1967), excessive current density tends to dry out the soil near the anode very rapidly, thereby reducing the voltage gradient applied to the soil. Nicholls and Herbst (1967) and Lockhart (1983) found that electro-osmosis is much more energy efficient at lower voltage gradients. Moreover, a lower voltage gradient also reduces the pH rise of the drainage water at the cathode (Veal et al., 2000). But, on the other hand, a lower voltage gradient results in a lower rate of dewatering than at high voltage gradient.

2.5.2. INTERMITTENT CURRENT AND POLARITY REVERSAL IN ELECTRO-OSMOSIS

To improve the effectiveness of electro-osmosis treatment, polarity reversal and intermittent current have been investigated. A clear benefit of intermittently switching off the power supply for a short period was reported by Sprute and Kelsh (1976). Moreover, Micic et al. (2001) reported that, during an electro-osmosis experimental programme on marine sediment, the power consumption and electrode corrosion were reduced by using intermittent current. However, as discussed by Lockhart and Hart (1988), intermittent current will produce no real benefit if the free water near the cathode is not removed.

As investigated by [Mohamedelhassan and Shang \(2001\)](#), with current intermittence a higher electro-osmosis permeability was found than when a continuous current was applied. [Glendinning et al. \(2008\)](#) applied current intermittence in a field trial involving the dewatering of sludge using electro-osmosis.

[Shang et al. \(1996\)](#) demonstrated an improvement in shear strength of 383 % when using polarity reversal, compared with 363 % when not using polarity reversal. [Wan and Mitchell \(1976\)](#) showed that, with polarity reversal, electro-osmosis consolidation was much more uniform between the electrodes. Additional reported benefits include reduced soil desiccation and cracking at the anode ([Abiera et al., 1999](#)), reduced anode corrosion ([Shang et al., 1996](#)) and the balancing of the water pH value at the electrodes ([Shang, 1997a](#)).

2.5.3. CHEMICAL TREATMENT TO IMPROVE ELECTRO-OSMOSIS CONSOLIDATION

To enhance the effect of electro-osmosis improvement, the injection of chemical solutions into the soil during electro-osmosis has been adopted. [Gray \(1970\)](#) used the electro-osmotic technique to inject aluminum ions into mixes of silica flour with illitic soils and montmorillonitic soils. The results showed the liquid limit of montmorillonite dropping to about half its initial value, while the liquid limit for illite was not significantly changed. Their results clearly indicate that it is possible to alter the clay properties and cause mineralization by electrochemical methods. [Lefebvre and Burnotte \(2002\)](#) and [Burnotte et al. \(2004\)](#) used the initial electro-injection of a conductive solution to maintain a good soil–anode contact during electro-osmosis treatment. [Alshawabkeh and Sheahan \(2003\)](#) applied this technique to inject phosphoric acid at the cathode to stabilize a marine illitic soil over a period of 14 days. The results showed that the shear strength increased by 160% near the cathode. [Asavadorndeja and Glawe \(2005\)](#) applied chemical injection using the anode depolarization method and the shear strength of the soil was increased by interparticle cementation caused by the electro-chemical injection of phosphate into the soil under a DC field. [Chien and Ou \(2011\)](#) developed a novel technique of installing a supply pipe (for the chemical injection) between the anode and cathode, to expand the region of electro-osmosis improvement. The results showed that electro-osmosis with injection through the relay pipe was superior to that with injection through the anode; nearly 1.5 times better in terms of cementation area and 2 times better in terms of average cone resistance.

2.5.4. NEW ADVANCES IN ELECTRODE MATERIALS FOR USE IN ELECTRO-OSMOSIS

Many attempts have been made to develop new materials for use as electrodes. [Segall and Bruell \(1992\)](#) used graphite electrodes to evaluate the conditions that affect electro-osmosis in the removal of soil contaminant. The results showed that, in order to generate the same average flow rate, a graphite electrode consumes twice as much power than that of an iron electrode because of the greater electrical resistance. [Mohamedelhassan and Shang \(2001\)](#) used carbon-coated metal electrodes as anodes, but found that they resulted in the largest voltage drop at the electrode. [Bergado et al. \(2003\)](#) reported on the use of metal or carbon rod electrodes inserted into prefabricated vertical drains. The

carbon electrodes performed better initially, but disintegrated with time, and the metal anodes still had corrosion problems. Some of the newly developed materials include electrically conductive geosynthetics (EKGs) and a polymeric electrical vertical drain (EVD).

The EKGs have a great advantage over conventional metallic electrodes used in soil improvement applications, because they overcome the difficulties of corrosion, while maintaining sufficient electrical contact and physical removal of water from the system (Lamont-Black, 2001). Nettleton et al. (1998) presented an electro-osmosis treatment using EKG electrodes in two dimensions in the laboratory. Hamir et al. (2001) described the development of these EKGs and, in comparative tests, they performed as well as copper electrodes; a filter test showed no clogging of the EKGs or loss of material through them. Fourie and his co-workers (Fourie et al., 2002, 2004, 2007; Fourie and Jones, 2010) reported laboratory and field tank tests involving electro-osmosis dewatering of mine tailings using EKGs. The EKGs showed no sign of corrosion, even after 2 months of applying a continuous current in a large outdoor experiment. The form of EKG used as the cathode, being a conductive core enveloped by a geotextile sheet, also facilitated the collection and removal of water. Glendinning and her co-workers (Glendinning et al., 2005, 2007, 2008) studied the treatment of sludge using EKGs. Lamont-Black, Jones and their co-workers (Jones et al., 2006; Lamont-Black et al., 2005; Jones et al., 2008; Lamont-Black and Weltman, 2010; Jones et al., 2011; Lamont-Black et al., 2012) reported several geotechnical case applications using EKGs.

Vertical drains manufactured with a conducting polymer, called electric vertical drains (EVD), have been used in some laboratory and field tests in Singapore (Karunaratne et al., 2002; Chew et al., 2004; Karunaratne, 2011). With EVDs installed for passing DC voltage, the consolidation of soft clay can be further accelerated compared to conventional prefabricated vertical drains (PVD). The effectiveness of the electro-osmosis consolidation depends on the EVD–soil system resistivity. Cumulative electric energy is strongly correlated with the system resistance (Karunaratne, 2011). Besides electro-osmosis consolidation, EVDs provide electrokinetic attraction of ions, and can also be used in remediation work and dewatering of industrial waste. Electrical prefabricated vertical drains (ePVD) consist of a galvanized steel pipe, a flexible drainage pipe and an insulated soft copper wire, and have been used in the strength reclamation of soft clay in a Chinese coastal area (Liu et al., 2014). The ePVD has huge potential for the application of electro-osmosis consolidation due to the following traits: (1) high compressibility and hydraulic conductivity; (2) good electric conductivity; (3) low cost and easy availability (much cheaper than EKGs and EVD); (4) high strength for field installation in rough conditions.

2.5.5. EFFECT OF ZETA POTENTIAL

Zeta potential is quite an important property in electro-osmosis dewatering, which is defined as the electrical potential at the junction between the fixed and mobile parts of the electrical double layer. According to the Helmholtz–Smoluchowski model, the electro-osmosis permeability is dependent on the zeta potential.

As reported by Chen et al. (1996), the volume of water removed during the electro-osmosis dewatering of fine gold tailings was directly proportional to the zeta poten-

tial. [Shang \(1997b\)](#) also presented similar findings that the electro-osmosis permeability is proportional to the zeta potential, based on 10 tests on 6 different soils. [West and Stewart \(2000\)](#) found that electro-osmosis dewatering will lose effectiveness when meeting highly saline soils because of the drop in the zeta potential. Although high salinity (lower zeta potential) is detrimental to electro-osmosis, [Lockhart \(1992\)](#) suggested that there was an accelerated dewatering rate for salinity rates up to a moderate level. [Mohamedelhassan and Shang \(2002\)](#) also found there was an optimum salinity in the electro-osmosis test. [Asadi et al. \(2009\)](#) reported that the zeta potential was also highly related to the pH value in electro-osmosis tests on peat, and that the high degree of decomposition also leads to a higher zeta potential in peat.

2.5.6. USING ELECTRO-OSMOSIS DEWATERING IN DIFFERENT KINDS OF MATERIALS

Much early work on the use of electro-osmosis for the dewatering of different materials was done by a number of researchers. [Van Gassen and Sege \(1991\)](#) carried out an electro-osmosis experiment in frozen soil; the results showed that the electro-osmosis conductivity of frozen soil is a function of temperature, and that, if the temperature is below -0.4 C , the electro-osmosis conductivity decreases rapidly. The US Bureau of Mines pioneered the research of electro-osmosis dewatering of mine tailings in the 1960s and several successful field applications were reported ([Stanczyk and Feld, 1964](#); [Sprute et al., 1982](#)). The commonwealth Scientific and Industrial Research Organization in Australia took the concept further, and studied water content reduction and power consumption during electro-osmosis dewatering in coal washery tailings and sand washery tailings ([Lockhart and Stickland, 1984](#); [Lockhart, 1992](#)). [Shang and Lo \(1997\)](#) investigated an electro-osmosis dewatering test on an extremely fine phosphatic clay waste and showed that the solids content increased from 13% to 34%. [Fourie and Jones \(2010\)](#) reported electro-osmosis dewatering tests at different scales on different mine tailings materials; they found that the power consumption rate of a large outdoor tank test was up to 30 times lower than the laboratory test, and it was also shown in these experiments that not all mine tailings will respond to electro-osmosis dewatering ([Fourie et al., 2007](#)).

Soils with an organic content greater than 20% are generally termed organic soils. Electro-osmosis consolidation experiments on organic soil have been done in recent years. Studies have shown the potential for the application in dewatering this type of material. [Asadi et al. \(2009\)](#) investigated electro-osmosis phenomena in organic soils, and found that the pH value and degree of decomposition strongly affect the electro-osmosis in peat; it was also experimentally found that electro-osmosis flow in peat is feasible. [Kaniraj and Yee \(2011\)](#) and [Kaniraj et al. \(2011\)](#) carried out a series of electro-osmosis consolidation tests on organic soil. The influence of operational conditions, such as voltage gradient, organic content, initial water content, electrode configuration and the method of drainage were instigated. The results showed that electro-osmosis was effective in the strengthening of soft peat. Some optimum approaches which are used in normal clay, such as polarity reversal, are also useful in organic soils.

2.6. SUMMARY

Since Casagrande first introduced electro-osmosis into civil engineering in the 1930s, successful field applications have been reported in the dewatering, strengthening, and stabilization of both soft clays and mine tailings. The success of these applications increased the confidence in applying electro-osmosis to fieldwork in general. On the other hand, a lot of laboratory investigations have also been done to improve the economics and efficiency of electro-osmosis treatment. The technique of polarity reversal, intermittent current and chemical solution injection were considered, and new materials like EKGs were developed to prevent electrode corrosion. Different materials were subjected to electro-osmosis with a view to extending the application of this technique.

So far, several numerical models of electro-osmosis consolidation have been developed; however, the mechanical behaviour and nonlinear properties of the soil were not considered in these models. Electro-osmosis consolidation is a very complicated process, as the mechanical behaviour, hydraulic and electrical properties of the soil are changing rapidly during the treatment process. A new numerical model which considers the nonlinear properties of hydraulic flow, electrical flow, and soil mechanical behaviour, as well as, geometric nonlinearity, is needed, and this forms the basis of this thesis.

3

LARGE STRAIN ELASTIC ELECTRO-OSMOSIS CONSOLIDATION OF CLAYS

This chapter presents the theoretical background of an elastic electro-osmosis consolidation model for saturated soils experiencing large strains, which considers volumetric strains induced by changes in both the hydraulic and electric driven pore water flows. Three fully coupled governing equations, considering the soil mechanical behaviour, pore water transport and electrical field, and their numerical implementation within an updated Lagrangian finite element formulation, are presented. The proposed model is first verified against a classical one-dimensional analytical solution for electro-osmosis consolidation to demonstrate its accuracy and efficiency. Then, various numerical examples are investigated to study the deformation characteristics and time dependent evolution of excess pore pressure. Finally, the importance of considering large strains in a consistent and proper way is demonstrated, and differences compared to models based on small strain theory are highlighted.

Parts of this chapter have been published in *Computers and Geotechnics* **54**, 60-68 (2013) (Yuan and Hicks, 2013).

3.1. INTRODUCTION

In geotechnical consolidation problems, the deformation is usually coupled with the flow of pore fluids based on the consolidation theory of Biot (1941). Carter et al. (1977, 1979) presented a model for large deformation elastic and elastoplastic consolidation for the first time, whereas Prévost (1980, 1982) proposed a generalized incremental form of large deformation consolidation involving material nonlinearity under both static and dynamic loadings. Zienkiewicz and Shiomi (1984) and Meroi et al. (1995) derived a numerical model of dynamic large deformation consolidation in saturated and unsaturated porous media. Borja and Alarcón (1995) and Borja et al. (1998) developed a mathematical model for large deformation elastoplastic consolidation of fully saturated soil media and then implemented it into a finite element program. Li et al. (2004) presented a dynamic hyperelastic consolidation model under finite strain. Andrade and Borja (2007) proposed an elastoplastic large deformation model for partially saturated consolidation. Nazem et al. (2008) presented an arbitrary Lagrangian–Eulerian method for analysing large deformation elastoplastic consolidation problems.

The electro-osmosis consolidation of soft clay is a coupled process involving mechanical behaviour, hydraulic flow and electrical flow under large deformation. The conceptual basics and theory of electro-osmosis consolidation have been studied by many of the above authors, but few analytical and numerical studies have considered the fully coupled process of soil mechanical behaviour, pore water flow and electrical flow. Furthermore, the geometric nonlinearity of the solid skeleton has not been considered in the numerical modelling of electro-osmosis consolidation, although much of the previous experimental work mentioned in chapter 2 reported large scale deformations during tests.

This chapter develops a numerical model for the finite element solution of hydro-mechanical–electrical processes in fully saturated porous media, assuming isotropic elastic soil skeleton behaviour at large strains. Three fully coupled governing equations considering force equilibrium, pore water transport and electrical current flow are presented and solved, via the finite element method in the space domain and an implicit integration scheme in the time domain, and an updated Lagrangian (UL) method is employed to solve for large deformations.

The chapter is organized as follows. In section 3.2 the governing equations of electro-osmosis consolidation, as well as the kinematics and deformations for UL formulations, are recalled. Furthermore, the Jaumann stress rates used in large deformation analysis which consider the effect of rigid body rotations are discussed. Then the linearization of weak formulations of the equilibrium condition is briefly introduced. Section 3.3 addresses the finite element procedure in detail, and the discretization of the governing equations in space and time are briefly described. Thus a classical finite element formulation is obtained, comprising increments of displacements, pore water pressure and electrical potential as the primary variables. The nonlinear finite element equations are solved using the modified Newton–Raphson scheme and the numerical algorithm has been implemented into a finite element code. In section 3.4, the proposed methodology is first validated against the analytical solution developed by Esrig (1968). This is followed by a series of numerical examples, to investigate both the performance of large strain electro-osmosis consolidation, as well as the differences between small and large

strain solutions.

3.2. THEORETICAL AND GOVERNING FORMULATIONS

In this chapter, an isotropic fully saturated soil with an incompressible pore liquid and soil particles is considered. The governing equations for the equilibrium of force, electric potential and hydraulic head are derived based on the following assumptions: the temperature in the soil is constant during the simulation; the effect of electrical–chemical reactions is negligible; the current due to the electrophoresis of the fine grained particles is negligible (Esrig, 1968); the flow of fluid due to the electrical and hydraulic gradients may be superimposed to obtain the total flow (Esrig, 1968); Ohm's law is valid; Darcy's law is valid; and the electrical gradient caused by the movement of ions is negligible compared to the applied electrical field. Note that during the electro-osmosis process heat is generated locally near the electrodes; however, heat generation has generally not been observed during laboratory electro-osmosis consolidation due to large heat dissipation at the boundaries of the specimen.

3.2.1. KINEMATICS AND DEFORMATIONS

To deal with large deformation problems, some assumptions and different configurations need to be discussed first. If the initial (i.e. reference) configuration of a physical body is denoted by Ω_0 , an arbitrary point in the body is often represented by its initial coordinates X_i . Let Ω denote the current configuration of the body and x_i represent the current coordinates of the arbitrary point. The mapping function φ is a key relationship between Ω_0 and Ω , which relates the initial and current position vectors. Hence, for a typical time-step, the updated configuration of the body at time $t + \Delta t$ may be written as a function of the configuration at time t and the incremental displacement during the time-step Δt , i.e. (Bathe, 1996)

$$x_i^{t+\Delta t} = \varphi_i(X_i, t + \Delta t) \quad (3.1)$$

The current and fixed reference configurations are related to each other by the displacement, so that an updated position vector can be written as

$$x_i^{t+\Delta t} = X_i + u_i = x_i^t + \Delta u_i \quad (3.2)$$

whereas the increments in the displacement over the time steps are given by

$$\Delta u_i = u_i^{t+\Delta t} - u_i^t = x_i^{t+\Delta t} - x_i^t \quad (3.3)$$

During the motion of a body, its volume, surface area, stresses and strains are changing continuously. A fundamental measure of the deformation is given by the deformation gradient, defined as

$$F_{ij} = \frac{\partial \varphi_i}{\partial X_j} = \frac{\partial x_i}{\partial X_j} = \delta_{ij} + \frac{\partial u_i}{\partial X_j} \quad (3.4)$$

where δ_{ij} is the Kronecker delta and the incremental deformation map is described as $\varphi_i^{t+\Delta t} + \Delta u_i$. Consequently, the deformation gradient at time $t + \Delta t$ can be obtained as

$F_{ij}^{t+\Delta t} = f_{ij}^t F_{ij}^t$, where F_{ij}^t is the deformation gradient at time t , and f_{ij}^t is the incremental deformation gradient from time t to $t + \Delta t$, defined as

$$f_{ij}^t = \frac{\partial x_i^{t+\Delta t}}{\partial x_j^t} = \delta_{ij} + \frac{\partial \Delta u_i}{\partial x_j^t} \quad (3.5)$$

The volume change between the reference and current configurations can be established as

$$d\Omega^{t+\Delta t} = \det F^{t+\Delta t} d\Omega^0 = J^{t+\Delta t} d\Omega^0 \quad (3.6)$$

where J is the Jacobian determinant, which is the determinant of the deformation gradient F . The Green strain tensor is given as (Bathe, 1996; Lewis and Schrefler, 1998)

$$E_{ij} = \frac{1}{2}(F_{ik}F_{jk} - \delta_{ij}) = -\frac{1}{2}(u_{i,j} + u_{j,i} + u_{k,i} \cdot u_{k,j}) \quad (3.7)$$

With regard to the fluid phases, it is common to assume the motion of the solid as a reference and to describe the fluid relative to the solid. Hence, the velocity of the pore water and electrical particles can be written with reference to the current configuration of the solid body (Meroi et al., 1995; Lewis and Schrefler, 1998). When doing this, some care needs to be taken regarding changes in the permeability tensors due to rigid body rotation (Carter et al., 1977, 1979; Nazem et al., 2008), when the material is anisotropic.

By employing the expressions above, the quantities of interest can be transferred to a known configuration where the governing equations can be solved.

3.2.2. MECHANICAL EQUILIBRIUM AND EFFECTIVE STRESS CONCEPT

The stress equilibrium equation, at time $t + \Delta t$, can be expressed as

$$\int_{V^{t+\Delta t}} \sigma_{ij}^{t+\Delta t} \cdot \delta \varepsilon_{ij} \cdot dV^{t+\Delta t} = R^{t+\Delta t} \quad (3.8)$$

where $\delta \varepsilon_{ij}$ is the variation of the strain tensor, V is the volume of the body, σ_{ij} is the Cauchy stress tensor, and R is the external work resulting from the body forces and surface tractions. In order to solve this equation, all quantities must be transferred to a known configuration, which is the current configuration in this chapter. So the equilibrium equation can be expressed as

$$\int_{V^t} S_{ij}^{t+\Delta t} \cdot \delta E_{ij}^{t+\Delta t} \cdot dV^{t+\Delta t} = R^{t+\Delta t} \quad (3.9)$$

where S_{ij} is the second Piola–Kirchhoff stress tensor and E_{ij} is the Green strain tensor. The second Piola–Kirchhoff stress tensor is related to the Cauchy stress tensor by the deformation gradient F_{ij} as follows:

$$\sigma_{ij}^t = \frac{1}{J^t} F_{ik}^t S_{kl}^t F_{jl}^t \quad (3.10)$$

Moreover, the incremental decompositions of the second Piola–Kirchhoff stress tensor can be expressed as

$$S_{ij}^{t+\Delta t} = S_{ij}^t + \Delta S_{ij} \quad (3.11)$$

where $S_{ij}^t = \sigma_{ij}^t$ in updated Lagrangian formulations. The incremental decompositions of the Green strain tensor can be written as

$$\Delta E_{ij}^t = \Delta e_{ij}^t + \Delta \eta_{ij}^t \quad (3.12)$$

$$\Delta e_{ij}^t = -\frac{1}{2}(u_{i,j} + u_{j,i}) \quad (3.13)$$

$$\Delta \eta_{ij}^t = -\frac{1}{2}u_{k,i} \cdot u_{k,j} \quad (3.14)$$

where Δe_{ij} and $\Delta \eta_{ij}$ are the linear and non-linear incremental Green strain tensors, respectively. By substituting Eqs. (3.11) and (3.12) into Eq. (3.9) and ignoring the high order terms, the linearized governing equation for the equilibrium of force is obtained as (Bathe, 1996)

$$\int_{V^t} \bar{C}_{ijkl} de_{kl} \delta e_{ij} dV^t + \int_{V^t} \sigma_{ij}^t \delta \eta_{ij} dV^t = R^{t+\Delta t} - \int_{V^t} \sigma_{ij}^t \delta e_{ij} dV^t \quad (3.15)$$

where \bar{C}_{ijkl} is the stress–strain matrix derived from the constitutive relationship $dS_{ij} = \bar{C}_{ijkl} dE_{ij}$.

When dealing with large deformation effects, involving also large rotations, care must be taken to ensure the material frame invariance of the model. To do that, a frame-independent stress rate, such as the Jaumann stress rate, needs to be introduced (Carter et al., 1977), i.e.

$$d\sigma_{ij}^J = d\sigma'_{ij} - \sigma'_{ik} d\Omega_{kj} - \sigma'_{jk} d\Omega_{ki} = C_{ijkl} \cdot de_{kl} \quad (3.16)$$

where C_{ijkl} is the stress–strain matrix derived from the constitutive relations in terms of the Cauchy stresses and the linear strain. The Jaumann stress rate is related to the Cauchy stress rate by the non-objective spin tensor Ω_{ij} , which may be given by

$$\Omega_{ij} = \frac{1}{2} \left(\frac{\partial u_i}{\partial x_j} - \frac{\partial u_j}{\partial x_i} \right) \quad (3.17)$$

According to the principle of effective stress, the incremental total stress can be written as

$$d\sigma_{ij} = d\sigma'_{ij} + dp \delta_{ij} \quad (3.18)$$

Using Eq. (3.16), the incremental stress can be rewritten as

$$d\sigma_{ij} = C_{ijkl} \cdot de_{kl} + \sigma'_{ik} d\Omega_{kj} + \sigma'_{jk} d\Omega_{ki} + \delta_{ij} dp \quad (3.19)$$

Equation (3.19) implies that the total stress rate can be decomposed into a stress rate (Jaumann) due to straining, a stress rate due to rigid body rotation and a contribution

due to pore water pressure change. By substituting Eq. (3.19) into the virtual work equation, Eq. (3.15), the following equilibrium equation for the updated Lagrangian method based on the Jaumann stress rate can be obtained:

$$\begin{aligned}
& \int_{V^t} C_{ijkl} d e_{kl} \delta e_{ij} d V^t + \int_{V^t} (\sigma'_{ik} d \Omega_{kj} + \sigma'_{jk} d \Omega_{ki}) \delta e_{ij} d V^t \\
& + \int_{V^t} \delta_{ij} p^t \delta \eta_{ij} d V^t + \int_{V^t} \sigma'_{ij} \delta \eta_{ij} d V^t + \int_{V^t} \delta_{ij} d p \delta e_{ij} d V^t \\
& = R^{t+\Delta t} - \int_{V^t} \sigma'_{ij} \delta e_{ij} d V^t - \int_{V^t} \delta_{ij} p^t \delta e_{ij} d V^t
\end{aligned} \quad (3.20)$$

3.2.3. PORE WATER TRANSPORT

The mass conservation of the pore water can be expressed by

$$\frac{\partial v_{si}}{\partial t} + \frac{\partial v_i}{\partial x_i} = 0 \quad (3.21)$$

where v_{si} is the velocity of the soil particles and v_i is the velocity of the pore water in the soil, which comprises two components. One is the hydraulic flow caused by the gradients of pore water pressure and the other is the electro-osmosis flow caused by electrical potential gradients. From Darcy's law, the hydraulic flow can be expressed as

$$v_{wi} = -\frac{k_{wij}}{\gamma_w} \frac{\partial}{\partial x_j} (p + \gamma_w z) \quad (3.22)$$

where k_w , γ_w and z are the coefficient of hydraulic conductivity, the unit weight of water and the elevation, respectively. The fluid flux due to electro-osmosis is (Esrig, 1968; Mitchell and Soga, 2005)

$$v_{eoi} = -k_{eoi} \frac{\partial V}{\partial x_j} \quad (3.23)$$

where k_{eo} is the coefficient of electro-osmosis conductivity and V is the electrical potential. According to Esrig's assumption, these two independent flows can be combined to give the total flow:

$$v_i = v_{wi} + v_{eoi} = -\frac{k_{wij}}{\gamma_w} \frac{\partial}{\partial x_j} (p + \gamma_w z) - k_{eoi} \frac{\partial V}{\partial x_j} \quad (3.24)$$

Consequently, the equation of pore water mass conservation can be written in the following form by substituting Eqs. (3.24) into Eq. (3.21):

$$\frac{\partial v_{si}}{\partial t} + \frac{\partial}{\partial x_i} \left(-\frac{k_{wij}}{\gamma_w} \left(\frac{\partial p}{\partial x_j} + \gamma_w z \right) \right) + \frac{\partial}{\partial x_i} \left(-k_{eoi} \frac{\partial V}{\partial x_j} \right) = 0 \quad (3.25)$$

3.2.4. ELECTRICAL TRANSPORT

According to Ohm's law, the flow of electrical current can be expressed by

$$j_i = -k_{\sigma eij} \frac{\partial V}{\partial x_j} \quad (3.26)$$

where j is the electrical current density and $k_{\sigma e}$ is the electrical conductivity of the soil. By applying the conservation of charge and assuming the current is steady state:

$$-\frac{\partial j_i}{\partial x_i} = C_p \frac{\partial V}{\partial t} \quad (3.27)$$

where C_p is the electrical capacitance per unit volume. The electrical capacitance of the soil can be considered negligible, and so C_p is assumed to be zero (Alshawabkeh and Acar, 1996; Tamagnini et al., 2010). Substituting Eq. (3.26) into Eq. (3.27) gives the governing equation of the electric current flow:

$$\frac{\partial}{\partial x_i} (k_{\sigma eij} \frac{\partial V}{\partial x_j}) = 0 \quad (3.28)$$

3.2.5. FINIAL GOVERNING EQUATIONS

The primary variables, namely the displacements, pore pressure and electrical potential, are coupled through the governing equations at large strain for mechanical equilibrium, pore water transport and electrical current transport, i.e. Eqs. (3.20), (3.25) and (3.28), respectively.

3.3. APPLICATION OF FINITE ELEMENT METHOD

3.3.1. FINITE ELEMENT DISCRETIZATION

For a quantitative solution, Eqs. (3.20), (3.25) and (3.28) are discretized in space by finite elements using a Galerkin procedure. The method starts by discretizing the unknown dependent variables over the whole domain using the shape function matrices \mathbf{N}_u , \mathbf{N}_p and \mathbf{N}_V , as functions of the respective nodal value vectors \mathbf{u}_e , \mathbf{p}_e and \mathbf{V}_e , i.e.

$$\begin{aligned} u &= \mathbf{N}_u \mathbf{u}_e \\ p &= \mathbf{N}_p \mathbf{p}_e \\ V &= \mathbf{N}_V \mathbf{V}_e \end{aligned} \quad (3.29)$$

where u , p and V are the respective dependent variables of displacement, excess pore pressure and electrical potential. By introducing the shape functions, the equilibrium Eq. (3.20) can be written as

$$[\mathbf{K}_e + \mathbf{K}_g] \mathbf{u} + \mathbf{Lp} = \mathbf{F}^{ext} \quad (3.30)$$

where \mathbf{K}_e is the elastic stiffness matrix for small deformations, given by

$$\mathbf{K}_e = \int_{V^t} \mathbf{B}_L^T \mathbf{D} \mathbf{B}_L dV^t \quad (3.31)$$

in which \mathbf{D} is the elastic strain–stress matrix, and \mathbf{K}_g is the geometric stiffness matrix, which is determined from the effective stresses σ^{tt} and pore pressure p^t at the beginning of the load step:

$$\mathbf{K}_g = \int_{V^t} \mathbf{B}_L^T \bar{\sigma}^t \bar{\mathbf{B}}_L dV^t + \int_{V^t} \mathbf{B}_{NL}^T \mathbf{p}^t \mathbf{B}_{NL} dV^t + \int_{V^t} \mathbf{B}_{NL}^T \hat{\sigma}^t \mathbf{B}_{NL} dV^t \quad (3.32)$$

where \mathbf{B}_L , \mathbf{B}_{NL} and $\bar{\mathbf{B}}_L$ are the strain–displacement operators for the linear strain increment Δe_{ij} , the nonlinear strain increment $\Delta \eta_{ij}$ and the spin increment $\Delta \Omega_{ij}$, respectively. Moreover, $\bar{\sigma}^t$, $\hat{\sigma}^t$ and \mathbf{p}^t are the stress matrix caused by rotation, the initial stress matrix and the pore pressure matrix, respectively, which are based on the effective stresses and pore pressure at the beginning of the load step (Nazem et al., 2008), and are given in Appendix A. \mathbf{L} is the global coupling matrix given by

$$\mathbf{L} = \int_{V^t} \mathbf{B}_L^T \mathbf{I} \mathbf{N}_p dV^t \quad (3.33)$$

where $\mathbf{I} = [1, 1, 1, 0, 0, 0]^T$ and \mathbf{F}^{ext} is the external loads vector derived from the body loads and surface tractions:

$$\mathbf{F}^{ext} = \int_{S^t} \mathbf{N}_u^T \mathbf{t} dS^t + \int_{V^t} \mathbf{N}_u^T \mathbf{b} dV^t \quad (3.34)$$

where \mathbf{t} are the prescribed surface tractions and \mathbf{b} are the body forces.

The continuity equation for pore water, Eq. (3.25), becomes

$$\mathbf{L}^T \dot{\mathbf{u}} + \mathbf{K}_c \mathbf{p} + \mathbf{K}_{eo} \mathbf{V} = \mathbf{Q}_p^{ext} \quad (3.35)$$

where \mathbf{K}_c is the hydraulic flow matrix, given by

$$\mathbf{K}_c = - \int_{V^t} \gamma_w^{-1} \cdot \mathbf{B}_p^T \mathbf{k}_w \mathbf{B}_p dV^t \quad (3.36)$$

and where γ_w is the unit weight of the pore fluid, \mathbf{B}_p is the matrix containing the gradients of the pore pressure shape functions \mathbf{N}_p , and \mathbf{k}_w is the hydraulic permeability matrix. Also, \mathbf{K}_{eo} is the electro-osmosis flow matrix given by

$$\mathbf{K}_{eo} = - \int_{V^t} \mathbf{B}_p^T \mathbf{k}_{eo} \mathbf{B}_V dV^t \quad (3.37)$$

where \mathbf{B}_V is the matrix of the gradients of the electric potential shape functions \mathbf{N}_V , and \mathbf{k}_{eo} is the electro-osmosis permeability matrix. \mathbf{Q}_p^{ext} is the external fluid supply vector, given by

$$\mathbf{Q}_p^{ext} = \int_{S^t} \mathbf{N}_p^T \mathbf{q}_w dS^t \quad (3.38)$$

where \mathbf{q}_w is the prescribed surface flux.

The continuity equation for electric potential, Eq. (3.28), becomes

$$\mathbf{K}_{\sigma e} \mathbf{V} = \mathbf{Q}_V^{ext} \quad (3.39)$$

where $\mathbf{K}_{\sigma e}$ is the current flux matrix given by

$$\mathbf{K}_{\sigma e} = \int_{V^t} \mathbf{B}_V^T \mathbf{k}_{\sigma e} \mathbf{B}_V dV^t \quad (3.40)$$

in which $\mathbf{k}_{\sigma e}$ is the electrical conductivity matrix and \mathbf{Q}_V^{ext} is the external current supply vector:

$$\mathbf{Q}_V^{ext} = \int_{S^t} \mathbf{N}_V^T \mathbf{q}_e dS^t \quad (3.41)$$

where \mathbf{q}_e is the prescribed surface current flux.

The discretized governing equation for the coupled system of deformation, fluid flow and current flow can be written in rate form as

$$\begin{bmatrix} \mathbf{K}_{nl} & \mathbf{L} & \mathbf{0} \\ \mathbf{L}^T & \mathbf{0} & \mathbf{0} \\ \mathbf{0} & \mathbf{0} & \mathbf{K}_{\sigma e} \end{bmatrix} \begin{Bmatrix} \dot{\mathbf{u}} \\ \dot{\mathbf{p}} \\ \dot{\mathbf{V}} \end{Bmatrix} + \begin{bmatrix} \mathbf{0} & \mathbf{0} & \mathbf{0} \\ \mathbf{0} & \mathbf{K}_c & \mathbf{K}_{eo} \\ \mathbf{0} & \mathbf{0} & \mathbf{0} \end{bmatrix} \begin{Bmatrix} \mathbf{u} \\ \mathbf{p} \\ \mathbf{V} \end{Bmatrix} = \begin{Bmatrix} \dot{\mathbf{F}}^{ext} \\ \mathbf{Q}_p^{ext} \\ \dot{\mathbf{Q}}_V^{ext} \end{Bmatrix} \quad (3.42)$$

where $\mathbf{K}_{nl} = [\mathbf{K}_e + \mathbf{K}_g]$.

3.3.2. TIME STEPPING AND SOLUTION PROCEDURE

The governing equation of the coupled system, Eq. (3.42), can be written as

$$\mathbf{C}\dot{\mathbf{X}} + \mathbf{K}\mathbf{X} = \dot{\mathbf{W}}^{ext} \quad (3.43)$$

where

$$\mathbf{C} = \begin{bmatrix} \mathbf{K}_{nl} & \mathbf{L} & \mathbf{0} \\ \mathbf{L}^T & \mathbf{0} & \mathbf{0} \\ \mathbf{0} & \mathbf{0} & \mathbf{K}_{\sigma e} \end{bmatrix}, \quad \mathbf{K} = \begin{bmatrix} \mathbf{0} & \mathbf{0} & \mathbf{0} \\ \mathbf{0} & \mathbf{K}_c & \mathbf{K}_{eo} \\ \mathbf{0} & \mathbf{0} & \mathbf{0} \end{bmatrix}, \quad \mathbf{X} = \begin{Bmatrix} \mathbf{u} \\ \mathbf{p} \\ \mathbf{V} \end{Bmatrix}$$

$$\dot{\mathbf{X}} = \begin{Bmatrix} \dot{\mathbf{u}} \\ \dot{\mathbf{p}} \\ \dot{\mathbf{V}} \end{Bmatrix}, \quad \dot{\mathbf{W}}^{ext} = \begin{Bmatrix} \dot{\mathbf{F}}^{ext} \\ \mathbf{Q}_p^{ext} \\ \dot{\mathbf{Q}}_V^{ext} \end{Bmatrix}$$

Various time stepping schemes can be employed to solve Eq. (3.43) (Lewis and Schrefler, 1998; Sheng and Sloan, 2003), but in this study the commonly used θ method is employed. Applying this method, the dependent state variable and force vector can be defined as

$$\begin{aligned} \mathbf{X} &= \theta \mathbf{X}_n + (1 - \theta) \mathbf{X}_{n-1} \\ \dot{\mathbf{W}}^{ext} &= \theta \dot{\mathbf{W}}_n^{ext} + (1 - \theta) \dot{\mathbf{W}}_{n-1}^{ext} \end{aligned} \quad (3.44)$$

where n is the time step, θ is an integration parameter in the range $0 \leq \theta \leq 1$ and with $\theta \geq 0.5$ for unconditional stability. Using the finite difference time stepping scheme, the time derivative of the state variable is

$$\dot{\mathbf{X}} = \frac{\mathbf{X}_n - \mathbf{X}_{n-1}}{\Delta t} \quad (3.45)$$

where Δt is the time step size. Substituting Eqs. (3.44) and (3.45) into Eq. (3.43) gives

$$\begin{aligned} & \mathbf{C}\{\mathbf{X}_n - \mathbf{X}_{n-1}\} + \Delta t \mathbf{K}\{(1 - \theta)\mathbf{X}_{n-1} + \theta\mathbf{X}_n\} \\ & = \Delta t\{\theta \dot{\mathbf{W}}_n^{ext} + (1 - \theta)\dot{\mathbf{W}}_{n-1}^{ext}\} \end{aligned} \quad (3.46)$$

If $\theta = 1.0$ the method gives the classical backward Euler scheme, given by

$$\mathbf{C}\{\mathbf{X}_n - \mathbf{X}_{n-1}\} + \Delta t \mathbf{K}\mathbf{X}_n = \Delta t \dot{\mathbf{W}}_n^{ext} \quad (3.47)$$

Due to the geometric non-linearity in \mathbf{C} , this equation must be solved by iteration. Using the modified Newton–Raphson method, the residual vector of the coupled system is defined as

$$\mathbf{R}(\mathbf{X}_n) = \Delta t \dot{\mathbf{W}}_{n-1+\theta}^{ext} - (\mathbf{C} + \Delta t \theta \mathbf{K})\{\mathbf{X}_n - \mathbf{X}_{n-1}\} - \Delta t \mathbf{K}\mathbf{X}_{n-1} \quad (3.48)$$

The iterative updating scheme is then

$$\begin{aligned} \delta \mathbf{X}^j &= (\mathbf{C}(\mathbf{X}_n^{j-1}) + \Delta t \theta \mathbf{K}(\mathbf{X}_n^{j-1}))^{-1} \mathbf{R}_n(\mathbf{X}_n^{j-1}) \\ \Delta \mathbf{X}_n^j &= \Delta \mathbf{X}_n^{j-1} + \delta \mathbf{X}^j \\ \mathbf{X}_n^j &= \mathbf{X}_{n-1} + \Delta \mathbf{X}_n^j \end{aligned} \quad (3.49)$$

where the superscript j indicates the iteration number. During the iteration process within each time step, the displacement, pore pressure and electric potential are continuously updated, but the matrices \mathbf{C} and \mathbf{K} are kept constant, i.e. these are only updated for the very first iteration. The iterations are terminated once the unbalanced forces are small enough. Moreover, due to the nonlinear geometric matrix and the electro-osmosis permeability matrix, the matrix system to be solved is non-symmetric, so that a non-symmetric matrix solver must be employed.

3.4. VALIDATION AND NUMERICAL EXAMPLES

In this section, the proposed large deformation model is first validated with respect to a 1D analytical solution for electro-osmosis consolidation. This is followed by 1D and 2D plane strain examples, highlighting the difference between small and large deformation analyses of fully saturated electro-osmosis consolidation. These examples emphasize the importance of considering large deformation analyses for practical situations where small deformation assumptions are not appropriate. For this purpose, two finite element codes are used: one based on the small deformation electro-osmosis formulation, in which geometric nonlinearities are ignored, and a second based on the proposed large deformation model. Details of the small deformation electro-osmosis consolidation theory are given by [Yuan et al. \(2012\)](#).

3.4.1. 1D VERIFICATION

It has been shown that, when the compression is small, both small and large deformation models predict essentially the same consolidation behaviour ([Meroi et al., 1995](#); [Li et al., 2004](#); [Lewis and Schrefler, 1998](#)). Therefore, the proposed approach is first verified against a classical 1D analytical solution for electro-osmosis consolidation.

Esrig (1968) developed a 1D electro-osmosis consolidation theory, in which the governing equation can be expressed as

$$\frac{k_w}{\gamma_w} \frac{\partial^2 p}{\partial x^2} + k_{eo} \frac{\partial^2 V}{\partial x^2} = m_v \frac{\partial p}{\partial t} \quad (3.50)$$

Analytical solutions of this equation have been obtained for several cases. For the 1D case, assuming an open cathode and closed anode, the pore pressure is given by (Mitchell and Soga, 2005)

$$p(x, t) = -\frac{k_{eo}}{k_w} \cdot \gamma_w \cdot V(x) + \frac{2k_{eo} \cdot \gamma_w \cdot V}{k_w \pi^2} \cdot \sum_{n=0}^{\infty} \frac{(-1)^n}{m^2} \sin\left(\frac{m\pi x}{L}\right) \cdot \exp(-m^2 \pi^2 T_v) \quad (3.51)$$

where $m = n + 1/2$ is the time factor, m_v is the coefficient of compressibility and L is the distance between the anode and cathode. The average degree of consolidation U as a function of time is (Mitchell and Soga, 2005)

$$U = 1 - \frac{4}{\pi^3} \sum_{n=0}^{\infty} \frac{(-1)^n}{m^3} \exp(-m^2 \pi^2 T_v) \quad (3.52)$$

Furthermore, the maximum negative excess pore pressure developed at the anode is given by

$$p_{\max} = -\frac{k_{eo}}{k_w} \cdot \gamma_w \cdot V \quad (3.53)$$

From Eq. (3.53), the effectiveness of electro-osmosis consolidation is controlled by the ratio k_{eo}/k_w , with the effect of electro-osmosis dewatering increasing with an increase in

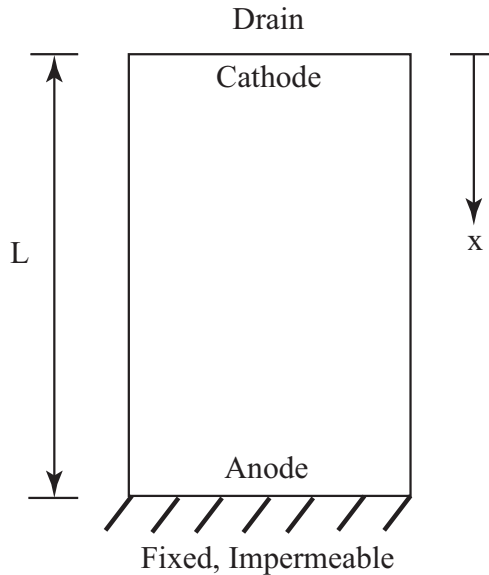


Figure 3.1: 1D electro-osmosis consolidation.

this ratio. To generate electro-osmosis consolidation effects of engineering significance, the ratio k_{eo}/k_w should be higher than 0.1 m/V.

The 1D model is shown in Figure 3.1 and is initially 1.0 m thick (i.e. $L = 1.0$ m). The following material parameters are assumed: electro-osmosis permeability of 2.0×10^{-9} m²/V·s, hydraulic conductivity of 2.0×10^{-8} m/s, coefficient of compressibility of 1.0×10^{-6} Pa⁻¹, electric conductivity of 0.1 S/m and Poisson's ratio of 0.3. These have been used for Esrig's solution and for the presented finite element analysis. For the latter, a 2D plane strain FEM model has been used, but with suitable boundary conditions to impose the 1D condition. The Young's modulus E can be obtained from the 1D relationship

$$E = n(1 - 2\nu)(1 + \nu)/(m_v(1 + (n - 2)\nu)) \quad (3.54)$$

where $n = 1$ is the dimension of the consolidation problem, and where $m_v = 1.0 \times 10^{-6}$ Pa⁻¹ and $\nu = 0.3$ for this problem. Hence the Young's modulus for the FEM model is $E = 7.4 \times 10^5$ Pa.

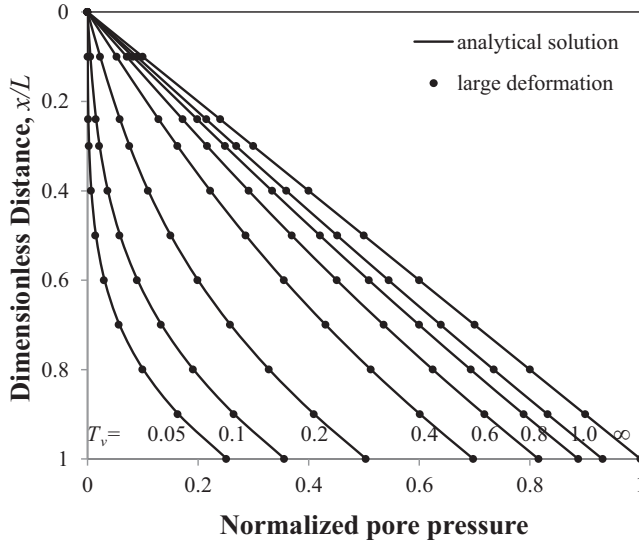


Figure 3.2: Normalized pore pressure versus time factor and normalized distance for 1D consolidation by electro-osmosis.

The initial excess pore pressure and initial electrical potential are set to zero throughout the problem domain. The displacement boundary conditions are that the bottom of the sample is fixed, whereas the left and the right boundaries are restrained only in the horizontal direction, and the top of the sample is free. The hydraulic boundary conditions are that there is free drainage at the top surface and that the remaining three boundaries are impermeable. The cathode is the top boundary and the anode is the bottom boundary, as seen in Figure 3.1. The electrical potential is maintained at 10 V at the anode throughout the analysis. The left and right boundaries are impermeable with

respect to electrical potential. An eight-node quadratic finite element is adopted for displacements and this is coupled to a four node quadrilateral for modelling excess pore water pressures and electrical potential. The gravity effect is neglected and 10 elements with a uniform size of 0.1×0.1 m are used to discretize the domain.

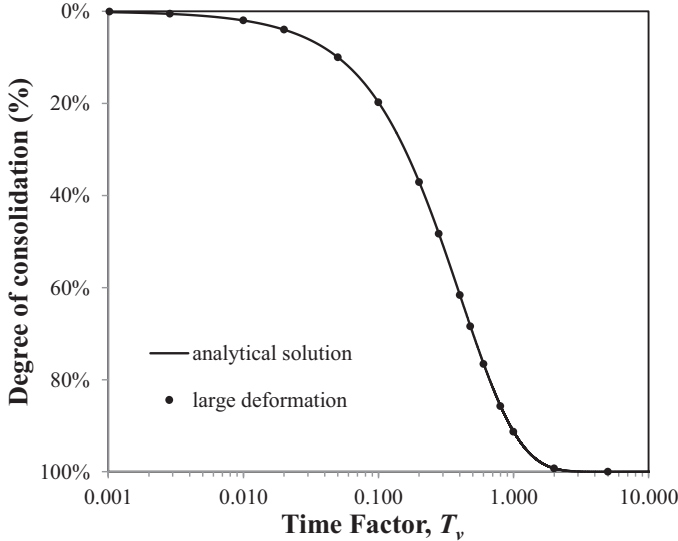


Figure 3.3: Average degree of consolidation versus time factor for one-dimensional consolidation by electro-osmosis.

The analytical solution presented by Mitchell and Soga (2005) is used to verify the numerical results. Profiles of normalized excess pore pressure (i.e. with respect to the maximum negative excess pore pressure) between the two electrodes at time factors of 0.05, 0.1, 0.2, 0.4, 0.8, 1.0 and at the steady state, are shown in Figure 3.2. The average degree of consolidation against time factor relationship is plotted in Figure 3.3. The figure shows excellent agreement between the results of the proposed approach and the theoretical solution under small strain compression, indicating that the new formulation is correctly modelling the coupling behaviour in electro-osmosis consolidation.

3.4.2. 1D ELECTRO-OSMOSIS CONSOLIDATION BEHAVIOUR

In order to study the time dependent behaviour of saturated clay under electro-osmosis consolidation and the difference between small and large deformation theories, the 1D FEM model from the previous section is subjected to a uniform surcharge load of $q = 100$ kPa for various voltage levels. The small deformation results are obtained using the numerical model of Yuan et al. (2012). Hence the material parameters are as follows: Young's modulus $E = 1.0$ MPa, Poisson's ratio $\nu = 0.3$, electro-osmosis permeability $k_{eo} = 5.0 \times 10^{-9}$ m²/V·s and hydraulic permeability $k_w = 2.0 \times 10^{-9}$ m/s.

Figures 3.4 and 3.5 show the numerical results obtained for small strain and large strain models when applying a voltage of 0, 10, 20 and 30 V in the first time step. In

Figure 3.4, the time behaviour of the excess pore pressure shows the difference between the small and large deformation models increasing with voltage level. The excess pore pressure develops faster in the large strain model compared to the small strain model, although both models reach the same excess pore pressure at the steady state. This is because the geometry change is accounted for in the large strain model, and so the electrical gradient is greater than that in the small strain model in which it is constant. Therefore, from Eq. (3.51) the pore water is driven out faster from the system, so that the pore pressure develops faster in the large strain model than in the small strain model. However, the final pore pressure developed at the anode is controlled by the potential applied according to Eq. (3.53), which is the same for both models when the system reaches the steady state.

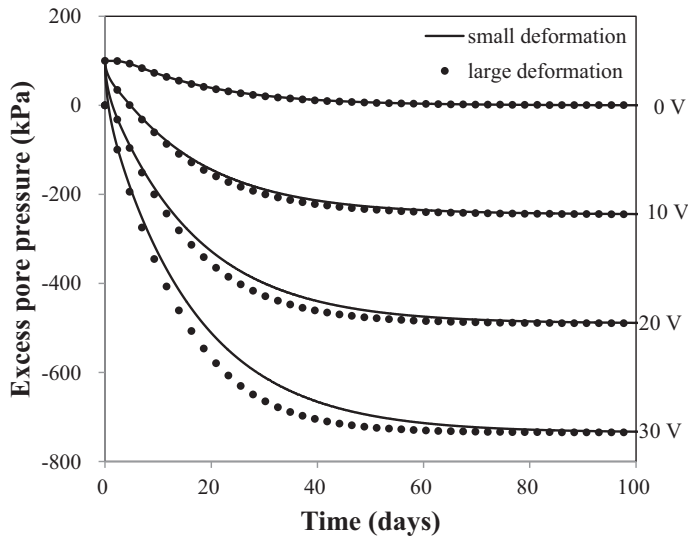


Figure 3.4: Excess pore pressure at the anode versus time relationship for different voltage levels (0, 10, 20, 30 V).

In Figure 3.5, the numerical results for vertical settlement are presented. The small deformation model predicts the final settlements to be proportional to the magnitude of the applied voltage, as expected for a linear elastic constitutive model. In contrast, the large deformation model gives final settlements that are not proportional to the voltage magnitude. The large deformation model gives lower absolute settlements at equilibrium compared to the small strain solution, due to the increasing geometric stiffness of the soil skeleton, which is inherent in the large strain model. With increasing voltage these differences become noticeable to such an extent that they cannot be neglected. The vertical settlement at the equilibrium state for the various voltage levels, for both small and large deformations, are listed in Table 3.1. It clearly shows the increasing difference in solution with growing voltage level.

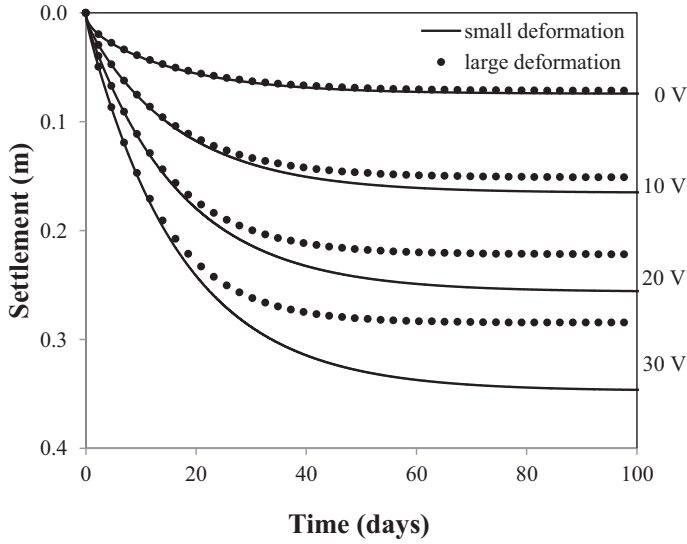


Figure 3.5: Vertical settlement versus time relationship for different voltage levels (0, 10, 20, 30 V).

Table 3.1: Vertical settlement at equilibrium state

Voltage (V)	Small deformation (m)	Large deformation (m)	Difference (%)
0	0.074	0.072	2.8
10	0.165	0.151	9.3
20	0.256	0.222	15.3
30	0.347	0.285	21.8

3.4.3. 1D CONSOLIDATION AS A FUNCTION OF k_{eo}/k_w

The ratio of electro-osmosis permeability and hydraulic permeability k_{eo}/k_w is a key factor in electro-osmosis consolidation. The 1D FEM model discussed above is now subjected to a uniform voltage and surcharge load for various ratios of k_{eo}/k_w . In this example, the electro-osmosis permeability $k_{eo} = 2.0 \times 10^{-8} \text{ m}^2/\text{V}\cdot\text{s}$, $V = 10 \text{ V}$ and a surcharge load of $q = 100 \text{ kPa}$ is kept constant throughout the simulation, whereas ratios of k_{eo}/k_w of 0.1, 1.0 and 10 are considered. Moreover, Young's modulus $E = 1.0 \text{ MPa}$ and Poisson's ratio $\nu = 0.3$.

Figures 3.6-3.8 show the linear small deformation solution for the electro-osmosis consolidation problem compared to the numerical results of the large deformation model, for different ratios of k_{eo}/k_w . In Figure 3.6 the excess pore pressure response of both models is almost the same for small ratios of k_{eo}/k_w (0.1, 1.0). As expected, the difference between the models increases with an increase in the ratio k_{eo}/k_w . The excess pore pressure develops quicker in the large strain model due to the strain dependent stiffness of the soil skeleton and the greater electrical gradient. However, both models develop the same amount of excess pore pressure at the steady state, since the development of

the final excess pore pressure is controlled by the ratio of k_{eo}/k_w .

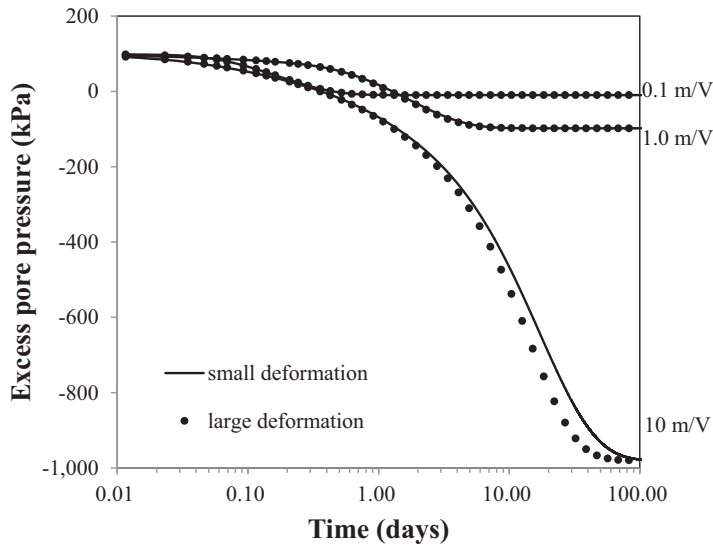


Figure 3.6: Excess pore pressure at the anode versus time relationship for different ratios of k_{eo}/k_w (0.1, 1.0, 10 m/V).

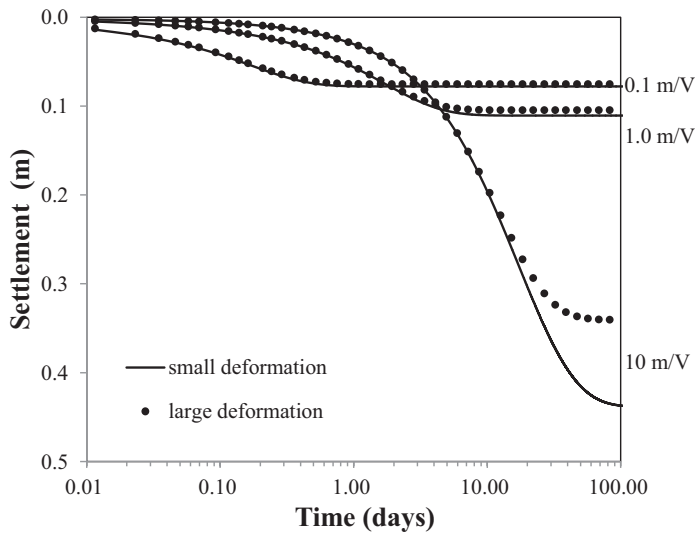


Figure 3.7: Vertical settlement versus time relationship for different ratios of k_{eo}/k_w (0.1, 1.0, 10 m/V).

The variation of surface settlement with time for different ratios of k_{eo}/k_w is shown

in Figure 3.7. As for the previous figure, the numerical results for the small and large deformation models deviate from each other with increasing ratio of k_{eo}/k_w . As expected from the strain dependent stiffness of the soil skeleton, the large deformation simulation predicts smaller settlement values at equilibrium compared to the small deformation model. The increasing difference between results for increasing ratio of k_{eo}/k_w illustrates the necessity of the large deformation model. Table 3.2 compares the vertical settlement at the equilibrium state for various ratios of k_{eo}/k_w for large and small deformation solutions.

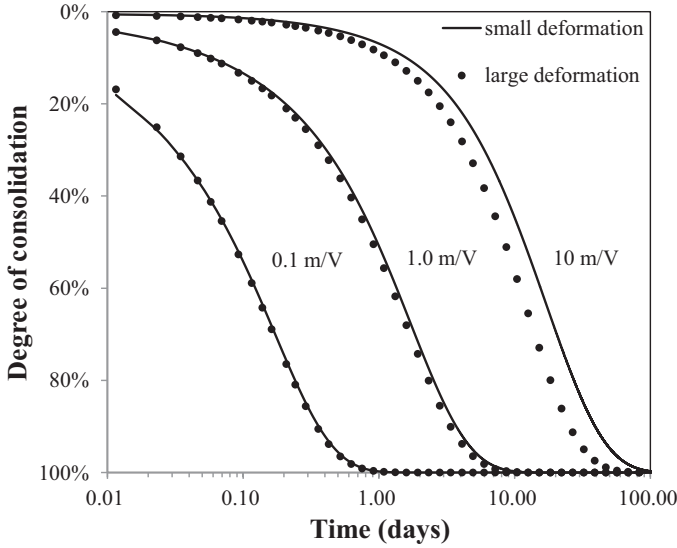


Figure 3.8: Average degree of consolidation versus time relationship for different ratios of k_{eo}/k_w (0.1, 1.0, 10 m/V).

Figure 3.8 shows the average degree of consolidation versus time relationship. The consolidation rate of the large deformation model is faster than the small deformation simulation and this difference increases with increasing of ratio of k_{eo}/k_w . As seen from Figures 3.6-3.8, the difference between the small and large deformation solutions increases with increasing strain (deformation) and, for high strains, the difference becomes large and should not be neglected.

Table 3.2: Vertical settlement at equilibrium state

Ratio of k_{eo}/k_w	Small deformation (m)	Large deformation (m)	Difference (%)
0.1	0.078	0.075	4.0
1.0	0.111	0.105	5.7
10.0	0.438	0.341	28.5

3.4.4. 2D CONSOLIDATION BEHAVIOUR OF ELECTRO-OSMOSIS

A square domain of side length 1 m is presented in Figure 3.9. In order to investigate the coupled soil behaviour, a surcharge load is applied on the top surface. The boundary conditions are as follows: the anode is along the left edge, which is also set as impermeable and on rollers allowing only vertical movement; the right edge is the cathode, which is also free draining and on rollers allowing only vertical movement; the bottom boundary is impermeable and fixed; the top surface is free draining and a uniform surcharge pressure, $q = 100$ kPa, is applied. An electric potential of 10 V is applied at the anode. The material parameters are: Young's modulus $E = 1.0$ MPa, Poisson's ratio $\nu = 0.3$, electro-osmosis permeability $k_{eo} = 5.0 \times 10^{-9}$ m²/V·s and hydraulic permeability $k_w = 2.0 \times 10^{-9}$ m/s. Quadrilateral elements with a uniform size of 0.1×0.1 m are used to discretize the domain.

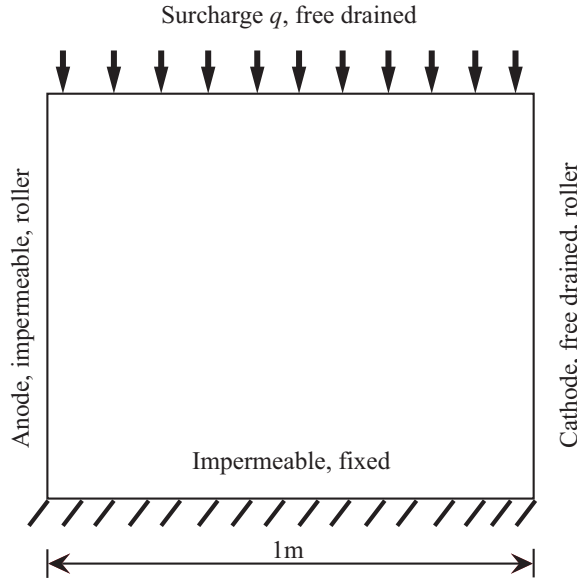


Figure 3.9: 2D electro-osmosis consolidation model.

The excess pore pressure versus time relationship at the base of the anode is shown in Figure 3.10. As for the 1D examples, both the small and large deformation models predict the same final negative excess pore pressure. However, the large deformation model predicts faster pore pressure development, especially for higher voltage magnitudes, due to the larger stiffness of the soil skeleton. The computed surface settlement versus time behaviour at the anode is shown in Figure 3.11. As for the 1D case, the large deformation model predicts smaller final settlements, with the difference in final settlement between the two models increasing with increasing voltage magnitude.

Figure 3.12 shows the final surface settlement as a function of the distance to the anode for different voltage magnitudes. For a voltage of 0 V, the difference between the small and large deformation models is small and the vertical settlement between the electrodes is uniform. As the voltage increases, the difference between the models be-

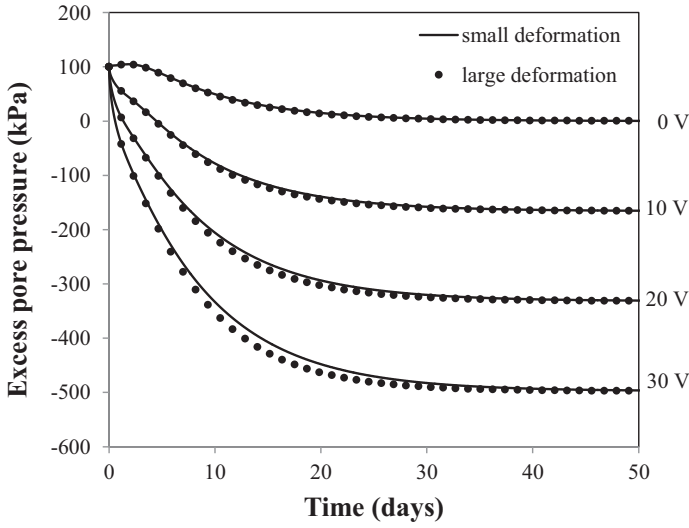


Figure 3.10: Excess pore pressure at the base of the anode versus time relationship for different voltage levels (0, 10, 20, 30 V).

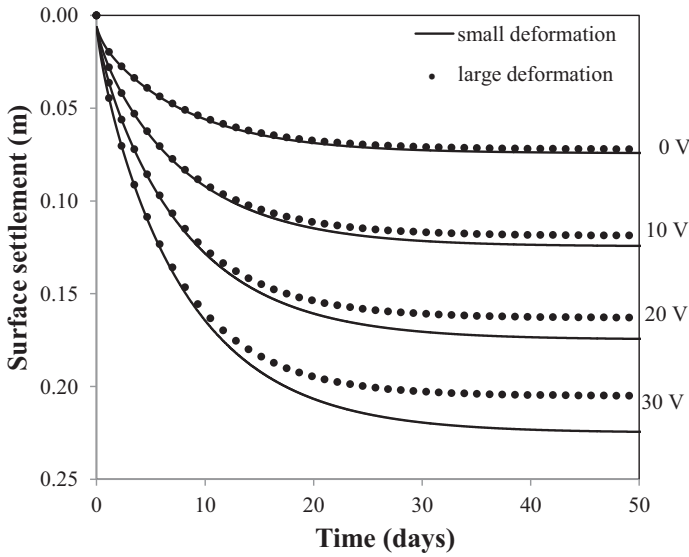


Figure 3.11: Surface settlement at the anode versus time relationship for different voltage levels (0, 10, 20, 30 V).

comes larger. Since negative excess pore pressures are developed near the anode, the vertical settlement at the anode is larger than at the cathode at the steady state, and this

difference increases with the voltage level. Note that, due to the 2D effect, the settlements are different at the cathode for different applied voltages, even though the excess pore pressure remains at zero due to the boundary condition. The surface settlements adjacent to the anode at the equilibrium state for various voltage levels, comparing small and large deformation models, are listed in Table 3.3 and show noticeable differences between the two sets of results. Consequently, the results are a further demonstration that the modelling of electro-osmosis consolidation has to be performed carefully and that large deformation consolidation theory is often necessary.

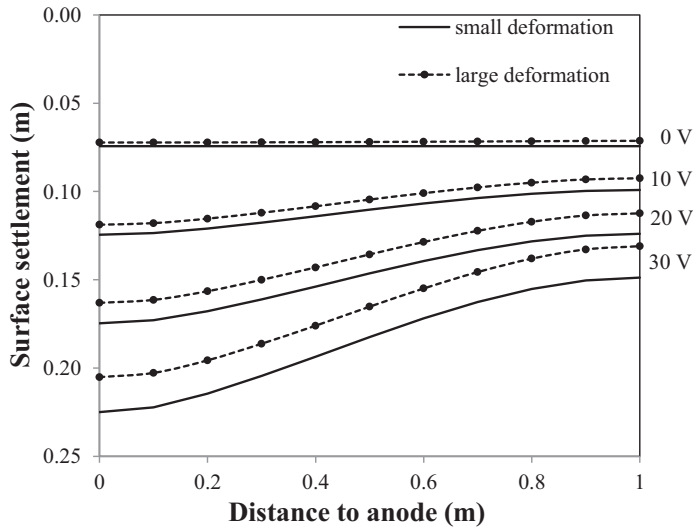


Figure 3.12: Final surface settlement relative to the anode for different voltage levels (0, 10, 20, 30 V).

Table 3.3: Surface settlement at equilibrium state (adjacent to top of anode)

Voltage (V)	Small deformation (m)	Large deformation (m)	Difference (%)
0	0.074	0.072	2.8
10	0.125	0.119	5.0
20	0.175	0.163	7.4
30	0.225	0.205	9.8

3.5. CONCLUSIONS

A finite strain formulation is necessary to accurately predict the time dependent response of electro-osmosis consolidation in soft soils, since large scale deformations (e.g. strains over 10 %) have been observed during previous laboratory and field tests. Small deformation models are not suitable for this purpose, since they do not account for the changing configuration and rigid body rotation that could have a significant effect on

predicted results. With this in mind, a formulation for considering the electro-osmosis consolidation of a soil incorporating large deformation effects has been presented. In developing the numerical model, attention has been restricted to linear elastic constitutive behaviour for the soil. Three coupled governing equations for force equilibrium, pore water transport and electrical transport have been written in an updated Lagrangian form based on the current configuration. These have been approximated using a finite element formulation and applied to a series of simple illustrative examples.

The numerical results for a 1D example of electro-osmosis consolidation show good agreement with an analytical solution. In comparison to small deformation solutions, the presented results of a second 1D example show the importance of considering large deformation theory in a consistent way. Then, a third 1D example has been used to show that an appropriate large deformation model is required (especially at high ratios of k_{eo}/k_w). An idealized 2D electro-osmosis consolidation problem considering surcharge load was then investigated. The numerical results for settlement and excess pore pressure demonstrate that the effectiveness of electro-osmosis consolidation is significant compared to the normal surcharge consolidation. The excess pore pressures develop faster in the large deformation model than in the small deformation model, finally reaching the same value at the steady state. On the other hand, the final settlements predicted by the large deformation model are always smaller than those predicted by the small deformation model. The noticeable differences between the two models illustrates the necessity of using large deformation models.

Using the same general formulation, it is possible to extend the numerical model to analyse the elasoplastic behaviour of clay during electro-osmosis consolidation. Furthermore, the nonlinear variations in soil parameters can easily be incorporated into the proposed approach by introducing a dependence of the absolute soil permeability (hydraulic, electro-osmosis and electrical) on void ratio.

4

NUMERICAL SIMULATION OF ELASTO-PLASTIC ELECTRO-OSMOSIS CONSOLIDATION AT LARGE STRAIN

In this chapter, a numerical solution for the electro-osmosis consolidation of clay in multi-dimensional domains at large strains is presented, with the coupling of the soil mechanical behaviour, pore water transport and electrical fields being considered. In particular, the Modified Cam Clay model is employed to describe the elasto-plastic behaviour of clay, and some empirical expressions are used to consider the nonlinear variation of the hydraulic and electrical conductivities of the soil mass during the consolidation processes. The implementation of the theoretical model in a finite element code allows for analysis of the evolution of the transient response of the clay subjected to electro-osmosis treatment. The proposed model is verified via comparison with data from a large strain electro-osmosis laboratory test, to demonstrate its accuracy and effectiveness. Various numerical examples are also investigated to study the deformation characteristics and time dependent evolution of the excess pore pressure. Finally, a well-documented field application of electro-osmosis is simulated to provide further verification. The results show that the numerical solution is effective in predicting the nonlinear behaviour of clay during electro-osmosis consolidation.

4.1. INTRODUCTION

In most of the previous approaches, the electro-osmosis consolidation is limited to the consideration of 1D problems. Moreover, force equilibrium and a linear elastic constitutive relationship for the soil are included implicitly in the formulation of the pore water transport, following Terzaghi's approach. As such, only two coupled/uncoupled partial differential equations for pore water transport and electrical current transport are solved, using either analytical approaches or numerical methods. In contrast, [Yuan et al. \(2012\)](#) presented a fully coupled solution considering force equilibrium, pore water transport and electrical transport, assuming that hydraulic and electrical properties remain constant during the simulation. [Tamagnini et al. \(2010\)](#) presented a numerical model for electro-osmosis processes in fine grained soils, accounting for gas generation and transport under unsaturated conditions. [Yuan and Hicks \(2013\)](#) presented an elastic electro-osmosis consolidation model for saturated soils experiencing large strains, and considered volumetric strains induced by changes in both the hydraulic and electric driven pore water flows. However, these approaches only incorporated an elastic constitutive relationship for the soil. In contrast, [Yuan et al. \(2013\)](#) developed a numerical model for electro-osmosis consolidation at small strain, coupling displacement, pore-water flow and electrical field, and incorporated the Modified Cam Clay (MCC) model for modelling nonlinear material behaviour.

The main objective of this chapter is to extend the theory of large strain elastic electro-osmosis consolidation to elasto-plasticity, by employing the Modified Cam Clay model to describe the elasto-plastic behaviour of clays. Moreover, some empirical expressions are incorporated to consider the nonlinear variation, with void ratio, of the hydraulic and electrical conductivities, and of the electro-osmosis permeability, of the soil mass, as these are considered to be more realistic than constant transport properties for describing the highly nonlinear processes. Three fully coupled governing equations, considering force equilibrium, pore water transport and electrical conduction are presented, and solved via the finite element method in the space domain and an implicit integration scheme in the time domain. Since no suitable numerical solutions of simple problems are available for validation purposes, a numerical simulation is compared with Feldkamp and Belhomme's (1990) experiment of large strain electro-osmosis consolidation of a vertical column. Furthermore, other numerical examples of electro-osmosis consolidation are presented. The results of these analyses suggest that the differences between large and small strain models are noticeable and should not be neglected, and that considering the nonlinear variation of the soil properties, especially the elasto-plastic constitutive relationships, has a significant impact on the deformation characteristics and time dependent evolution of the process. Finally, a well-documented field application of electro-osmosis treatment reported by [Bjerrum et al. \(1967\)](#) is simulated, for further verification of the numerical model.

The chapter is organized as follows. In Section 4.2 the governing equations of electro-osmosis consolidation, as well as the background of large strain theory, are recalled. Section 4.3 addresses the constitutive laws for the stress tensor, hydraulic conductivity, electro-osmosis permeability and electrical conductivity. In Section 4.4, several numerical examples are solved, which are used for validation of the code based on the outlined approach. These examples demonstrate the importance of proper numerical modelling

of the nonlinear soil behaviour during electro-osmosis consolidation.

4.2. THEORETICAL BACKGROUND AND GOVERNING EQUATIONS

4.2.1. MODELLING FRAMEWORK

The governing equations for the equilibrium of force, hydraulic head and electric potential are derived based on the following assumptions: (1) an isotropic fully saturated soil with an incompressible pore fluid and soil particles; (2) the coupled conduction processes occur under isothermal conditions; (3) the effect of electrical–chemical reactions is negligible; (4) electrophoresis and streaming currents are negligible (Esrig, 1968); (5) the flow of fluid due to the electrical and hydraulic gradients may be superimposed to obtain the total flow (Esrig, 1968); (6) Darcy's law is valid; (7) Ohm's law is valid.

The kinematics and deformations for large strain updated Lagrangian formulations are provided in detail in Chapter 3 and therefore only summarized here. Consider an arbitrary reference configuration \mathbf{X} , which has position \mathbf{x} at time t . The mapping function φ relates the initial and current position vectors. Hence, for a typical time step, the updated configuration of the body may be written as

$$\mathbf{x} = \varphi(\mathbf{X}, t) \quad (4.1)$$

A fundamental measure of the deformation is given by the deformation gradient, defined as

$$\mathbf{F} = \frac{\partial \varphi}{\partial \mathbf{X}} = \frac{\partial \mathbf{x}}{\partial \mathbf{X}} \quad (4.2)$$

The change in volume between the reference and current configurations can be established as

$$dV = JdV_0 \quad (4.3)$$

where V_0 and V are the reference and current volumes respectively, and J is the Jacobian determinant which is the determinant of the deformation gradient \mathbf{F} . The Green strain tensor is given as

$$\mathbf{E} = \frac{1}{2}(\mathbf{F}^T \mathbf{F} - \mathbf{I}) \quad (4.4)$$

where \mathbf{I} is a unit tensor. In order to compute the Cauchy stress $\boldsymbol{\sigma}$ the second Piola–Kirchhoff stress \mathbf{S} measured at the reference configuration has to be computed first. The Cauchy stress is related to the second Piola–Kirchhoff (PK2) stress by the deformation gradient as follows:

$$\boldsymbol{\sigma} = \frac{1}{J} \mathbf{F}^T \mathbf{S} \mathbf{F} \quad (4.5)$$

The spatial velocity \mathbf{v} of the material point \mathbf{x} is given by

$$\mathbf{v} = \mathbf{v}(\mathbf{x}, t) = \frac{\partial \mathbf{x}}{\partial t} \quad (4.6)$$

For an arbitrary scalar valued function $f^\pi(\mathbf{x}, t)$, its material time derivative, relative to its spatial description and referring to a moving particle of the π^{th} phase, is defined by

$$\frac{D^\pi f^\pi}{Dt} = \frac{\partial f^\pi}{\partial t} + \nabla f^\pi \cdot \mathbf{v}^\pi \quad (4.7)$$

In a multiphase porous medium, it is common to take the motion of the solid configuration as a reference and to describe the motion of, for example, the water (w) phase particles relative to those of the solid (s). Hence the water relative velocity can be written as

$$\mathbf{v}^{ws} = \mathbf{v}^w - \mathbf{v}^s \quad (4.8)$$

By considering the above relative velocity, the material time derivative of f^w with respect to the moving solid phase is given by

$$\frac{D^s f^w}{Dt} = \frac{D^w f^w}{Dt} + \nabla f^w \cdot \mathbf{v}^{sw} \quad (4.9)$$

4.2.2. MECHANICAL EQUILIBRIUM

The stress equilibrium equation can be expressed by

$$\nabla \cdot \boldsymbol{\sigma} + \mathbf{b} = \mathbf{0} \quad (4.10)$$

where $\boldsymbol{\sigma}$ represents the total Cauchy stress vector and \mathbf{b} represents the body force vector. In an updated Lagrangian (UL) formulation, in order to solve the above equation, all quantities must be transferred to the current configuration. So the equilibrium equation, at time $t + \Delta t$, can be written in its weak form as (Bathe, 1996)

$$\int_{V^t} \mathbf{S}^{t+\Delta t} \cdot \delta \mathbf{E}^{t+\Delta t} dV^t = \int_{V^t} \mathbf{b}^{t+\Delta t} \cdot \delta \mathbf{u}^{t+\Delta t} dV^t + \int_{S^t} \mathbf{t}^{t+\Delta t} \cdot \delta \mathbf{u}^{t+\Delta t} dS^t \quad (4.11)$$

where \mathbf{S} is the PK2 stress tensor, $\delta \mathbf{u}$ is the virtual displacement, \mathbf{t} are the boundary traction components and V is the volume of the body. Moreover, the incremental decomposition of the PK2 stress tensor can be expressed as

$$\mathbf{S}^{t+\Delta t} = \mathbf{S}^t + \Delta \mathbf{S} \quad (4.12)$$

when referenced to the current configuration at time t , for which $\mathbf{S}^t = \boldsymbol{\sigma}^t$ in the UL formulations. The decomposition of the Green strain tensor can be written as

$$\begin{aligned} \mathbf{E} &= \boldsymbol{\varepsilon} + \boldsymbol{\eta} \\ \boldsymbol{\varepsilon} &= -\frac{1}{2}(\nabla \mathbf{u} + (\nabla \mathbf{u})^T) \\ \boldsymbol{\eta} &= -\frac{1}{2}((\nabla \mathbf{u})^T \cdot \nabla \mathbf{u}) \end{aligned} \quad (4.13)$$

where $\boldsymbol{\varepsilon}$ and $\boldsymbol{\eta}$ are the linear and nonlinear parts of the Green strain tensor. By substituting Eqs. (4.12) and (4.13) into Eq. (4.11), and ignoring the high order terms, the linearized governing equation for equilibrium is obtained as

$$\begin{aligned} \int_{V^t} \bar{\mathbf{D}} \cdot d\boldsymbol{\varepsilon} \cdot \delta \boldsymbol{\varepsilon} dV^t + \int_{V^t} \boldsymbol{\sigma}^t \cdot \delta \boldsymbol{\eta} dV^t = \\ \int_{V^t} \mathbf{b}^{t+\Delta t} \cdot \delta \mathbf{u} dV^t + \int_{S^t} \mathbf{t}^{t+\Delta t} \cdot \delta \mathbf{u} dS^t - \int_{V^t} \boldsymbol{\sigma}^t \cdot \delta \boldsymbol{\varepsilon} dV^t \end{aligned} \quad (4.14)$$

where $\bar{\mathbf{D}}$ is the stress-strain matrix derived from the constitutive relationship $d\mathbf{S} = \bar{\mathbf{D}} \cdot d\mathbf{E}$ (Nazem et al., 2006).

4.2.3. BALANCE OF WATER MASS

The mass balance law for the solid phase in the current configuration may be written as

$$\frac{D^s(1-n)\rho^s}{Dt} + (1-n)\rho^s\nabla\cdot\mathbf{v}^s = 0 \quad (4.15)$$

where n is the porosity and ρ^s is the density of the solid particles. By taking account of the incompressibility of the solid particles, the mass balance equation becomes

$$-\frac{D^s n}{Dt} + (1-n)\nabla\cdot\mathbf{v}^s = 0 \quad (4.16)$$

The mass balance law for the water phase in the current configuration may be written as

$$\frac{D^w(n\rho^w)}{Dt} + n\rho^w\nabla\cdot\mathbf{v}^w = 0 \quad (4.17)$$

By introducing the relative velocity from Eq. (4.8) and the material time derivative with respect to the moving solid from Eq. (4.9), the water mass balance equation becomes

$$\frac{D^s(n\rho^w)}{Dt} + \nabla\cdot(n\rho^w\mathbf{v}^{ws}) + n\rho^w\nabla\cdot\mathbf{v}^s = 0 \quad (4.18)$$

By taking account of the incompressibility of the water, and by substituting Eq. (4.16) into Eq. (4.18), the material time derivative of n vanishes, so that

$$\nabla\cdot(\mathbf{v}^s + \bar{\mathbf{v}}) = 0 \quad (4.19)$$

where $\bar{\mathbf{v}} = n\mathbf{v}^{ws}$ is the filtration velocity of the water relative to the soil skeleton.

4.2.4. BALANCE OF ELECTRIC CHARGE

By applying the conservation of charge and assuming the current is steady state, the governing equation for the electric field can be represented as follows:

$$-\nabla\cdot\mathbf{j} = C_p \frac{\partial V}{\partial t} \quad (4.20)$$

where \mathbf{j} is the electrical current density, C_p is the electrical capacitance per unit volume and V is the electrical potential. As the electrical capacitance of the soil can be considered negligible, $C_p = 0$ is assumed.

4.3. CONSTITUTIVE EQUATIONS

The soil properties and electrical fields change during the electro-osmosis consolidation. The elasto-plastic soil behaviour causes nonlinear deformation of the soil. Moreover, the flow of water causes a non-uniform decrease in the water content and void ratio of the soil mass. These factors lead to changes in the hydraulic and electrical conductivities, and in the electro-osmosis permeability. Accordingly, the solution of the nonlinear coupled system can be solved numerically if suitable constitutive relationships are chosen.

4.3.1. SOLID SKELETON

The Cam Clay model was developed in the 1960s and is intended to capture the basic features of normally consolidated, as well as lightly over consolidated clay (Roscoe et al., 1963; Roscoe and Burland, 1968). There are two well-known versions of this model. The first is the so-called original Cam Clay model, while the other is the Modified Cam Clay model. In this study, the Modified Cam Clay model is employed to simulate elasto-plastic soil behaviour during electro-osmosis consolidation. It employs an associated flow rule, and the yield (f) and plastic potential (g) functions can be expressed by

$$f = g = q^2 - M^2 p'(p_c - p') \quad (4.21)$$

where the stress invariants p' and q represent the mean effective stress and deviatoric stress, respectively, M is the slope of the critical state line (CSL) in the p' - q plane and p_c is the pre-consolidation pressure, which is the hardening parameter of the model that can be expressed by

$$p_c = p_{c0} \exp\left(\frac{(1 + e_0)\Delta\varepsilon_v^p}{\lambda - \kappa}\right) \quad (4.22)$$

where λ and κ are the plastic compression index and unloading-reloading index, respectively, e_0 is the initial void ratio, $\Delta\varepsilon_v^p$ is the increment of plastic volumetric strain and p_{c0} is the pre-consolidation pressure at the beginning of plastic loading. According to standard elasto-plastic theory, \mathbf{D}_{ep} is the elasto-plastic stress-strain matrix given by

$$\mathbf{D}_{ep} = \mathbf{D}_e - \frac{\mathbf{D}_e \frac{\partial g}{\partial \sigma'} \frac{\partial f}{\partial \sigma'}^T \mathbf{D}_e}{H + \frac{\partial f}{\partial \sigma'}^T \mathbf{D}_e \frac{\partial g}{\partial \sigma'}} \quad (4.23)$$

where \mathbf{D}_e is the elastic stress-strain matrix and noting that, when the Jaumann stress rate is employed, \mathbf{D}_{ep} has an identical form to that encountered in small strain theory (de Souza Neto et al., 2008). σ' is the effective stress and H is the modulus of plastic hardening/softening.

The coupling between the deformation and flow processes is established using the principle of effective stress. Hence the total stress can be written as

$$\boldsymbol{\sigma} = \boldsymbol{\sigma}' + \mathbf{I}p \quad (4.24)$$

where p is the pore water pressure. When assuming large strain kinematics, involving also large rotations, care must be taken to ensure the material frame invariance of the model. To do that, a frame-independent stress rate such as the Jaumann stress rate needs to be introduced, i.e. (Nazem et al., 2008)

$$d\boldsymbol{\sigma}^J = d\boldsymbol{\sigma}' - d\boldsymbol{\Omega} \cdot \boldsymbol{\sigma}' - \boldsymbol{\sigma}' \cdot d\boldsymbol{\Omega}^T = \mathbf{D}_{ep} \cdot d\boldsymbol{\varepsilon} \quad (4.25)$$

where \mathbf{D}_{ep} is the stress-strain matrix derived from the constitutive relations in terms of the Cauchy stress and linear strain tensor $d\boldsymbol{\varepsilon}$ (Nazem et al., 2006), and the Jaumann stress rate is related to the Cauchy stress rate by the non-objective spin tensor $\boldsymbol{\Omega}$, given by

$$\boldsymbol{\Omega} = \frac{1}{2}[(\nabla \mathbf{u}) - (\nabla \mathbf{u})^T] \quad (4.26)$$

By substituting Eq. (4.25) into the effective stress equation, Eq. (4.24), the stress increment can be written as

$$d\sigma = \mathbf{D}_{ep} \cdot d\varepsilon + d\boldsymbol{\Omega} \cdot \boldsymbol{\sigma}' + \boldsymbol{\sigma}' \cdot d\boldsymbol{\Omega}^T + \mathbf{I} dp \quad (4.27)$$

In the large strain formulation based on the Jaumann stress rate, Eq. (4.25), the effective stress increment can be calculated by

$$\boldsymbol{\sigma}'^{t+\Delta t} = \boldsymbol{\sigma}'^t + \int_0^{\Delta\varepsilon} \mathbf{D}_{ep} \cdot d\varepsilon + \int_0^{\Delta\boldsymbol{\Omega}} (d\boldsymbol{\Omega} \cdot \boldsymbol{\sigma}'^t + \boldsymbol{\sigma}'^t \cdot d\boldsymbol{\Omega}^T) \quad (4.28)$$

Stress integration algorithms for large strain analysis have been discussed many times before. It has been shown that stress transformation due to rigid body rotation can be included in the equations before, after, or during the stress integration in each increment (Nazem et al., 2009). It has also been shown that, with this method, stress integration schemes used for small strain can be easily extended to large strain (Nazem et al., 2006). An explicit stress integration scheme with automatic sub-stepping and error control for large strain is implemented here to solve the elasto-plastic constitutive relationship.

4.3.2. PORE WATER TRANSPORT

The constitutive equation for the pore water flow velocity in electro-osmosis comprises two components. One is the hydraulic flow caused by the gradients of pore water pressure and the other is the electro-osmosis flow caused by electrical potential gradients. From Darcy's law, the hydraulic flow can be expressed as

$$\mathbf{v}_w = -\frac{k_w}{\gamma_w} \nabla(p + \gamma_w z) \quad (4.29)$$

where k_w , γ_w and z are the coefficient of hydraulic conductivity, unit weight of water and elevation, respectively. The fluid flux due to electro-osmosis can be expressed as a linear function of the applied electrical potential gradient:

$$\mathbf{v}_{eo} = -k_{eo} \nabla V \quad (4.30)$$

where k_{eo} is the coefficient of electro-osmosis permeability and V is the electrical potential. According to Esrig's (1968) assumption, these two independent flows can be combined to give the total flow:

$$\tilde{\mathbf{v}} = \mathbf{v}_w + \mathbf{v}_{eo} = -\frac{k_w}{\gamma_w} \nabla(p + \gamma_w z) - k_{eo} \nabla V \quad (4.31)$$

The Helmholtz–Smoluchowski model is widely used for explaining the electro-osmosis phenomenon in soil (Mitchell and Soga, 2005). In this model, k_{eo} is derived from the balance between the electrical force causing the water flow and the frictional force between the water and the wall of the capillary. It can be written as

$$k_{eo} = -\frac{\zeta \varepsilon n}{\mu} \quad (4.32)$$

where ζ is the zeta potential, ε is the permittivity of the pore fluid and μ is the viscosity of the pore fluid. In clayey soils, since the permittivity and viscosity of the pore water are approximately constant over a fairly large range of salinity, k_{eo} is controlled primarily by the zeta potential and soil porosity. As reported by [Mohamedelhassan and Shang \(2002\)](#), k_{eo} is mainly controlled by porosity when the pore fluid salinities are smaller than a certain value (8 g/L NaCl in their paper), and increases in magnitude with an increase in the soil porosity. There is a linear relationship between the electro-osmosis permeability and porosity, which can be expressed as

$$k_{eo} = An + B \quad (4.33)$$

where A and B are material constants that can be determined experimentally.

The hydraulic conductivity is one of the crucial parameters in the electro-osmosis process and it greatly influences the rate of consolidation and negative pore water pressure development. Although, in most electro-osmosis theories, the coefficient of hydraulic conductivity is assumed to be constant, in reality it is a function of the porosity or void ratio. A relationship between hydraulic conductivity and void ratio, e , has been reported by many researchers ([Mitchell and Soga, 2005](#); [Mohamedelhassan and Shang, 2002](#)). Such a relationship is typically obtained by curve-fitting experimental data and depends on the type of soil. For clays, a logarithmic equation may be used:

$$\log k_w = Ce + D \quad (4.34)$$

where C and D are material constants.

4.3.3. ELECTRIC CHARGE TRANSPORT

According to Ohm's law, the electrical current flow can be expressed by

$$\mathbf{j} = -k_{\sigma e} \nabla V \quad (4.35)$$

where $k_{\sigma e}$ is the electrical conductivity of the soil. The electrical conductivity is a function of the soil mineralogy and pore fluid composition. However, it is evident from experiments on marine clay that the electrical conductivity of the pore water is greater than that of the bulk soil. The electrical conductivity of a saturated porous medium can be represented by the following model ([Mohamedelhassan and Shang, 2002](#)):

$$k_{\sigma e} = \frac{k_{\sigma s} k_{\sigma w} (1 + e)}{k_{\sigma w} + e k_{\sigma s}} \quad (4.36)$$

where $k_{\sigma s}$ is the surface conductivity of the clay particles and $k_{\sigma w}$ is the conductivity of the pore water. [Mohamedelhassan and Shang \(2002\)](#) reported that the surface conductivity of the soil solid increases with pore water salinity and is independent of the void ratio of the bulk soil. They found that the soil bulk conductivity is proportional to the pore fluid salinity and soil void ratio. However, this soil conduction model is only suitable for describing the conductivity of marine sediments.

4.3.4. VOID RATIO AND CONDUCTIVITY/PERMEABILITY UPDATES

The nonlinear relationship between conductivity or permeability and void ratio has been accounted for in the above formulation. However, the method for updating the void ratio or porosity needs to be introduced here. First, let e^t represent the void ratio at time t . As the volume changes during soil deformation, the relationship for the incremental void ratio at time $t + \Delta t$ may be given by

$$e^{t+\Delta t} = J(1 + e^t) - 1 \quad (4.37)$$

where J is the Jacobian determinant of the deformation gradient tensor. In an updated Lagrangian approach where time step increments Δt are assumed to be small enough to justify neglecting the contribution from the second-order strain components during each step, the volume strain increment may be approximated by the trace of the linear strain tensor, so that $J \approx 1 + \text{tr}\varepsilon$. The void ratio, which is updated and stored at each integration point, can then be expressed as (Lewis and Schrefler, 1998; Meroi et al., 1995)

$$e^{t+\Delta t} = (1 + \text{tr}\varepsilon)(1 + e^t) - 1 = e^t + (1 + e^t)\text{tr}\varepsilon \quad (4.38)$$

Note that, when dealing with large deformation and rotation, some care needs to be taken regarding changes in the conductivity and permeability tensors due to rigid body rotation, if the material is initially anisotropic. This effect is expressed as

$$\mathbf{k}_\pi^{t+\Delta t} = \mathbf{R}^T \cdot \mathbf{k}_\pi^t \cdot \mathbf{R} \quad (4.39)$$

where \mathbf{k}_π represents the conductivity or permeability matrices of the hydraulic, electro-osmosis and electrical components, and \mathbf{R} is the local rotation matrix which corresponds to the appropriate rotations of the coordinate axes (Carter et al., 1977; Lewis and Schrefler, 1998; Nazem et al., 2008).

4.3.5. FINAL GOVERNING EQUATIONS

By taking account of the constitutive equations, Eqs. (4.27), (4.31) and (4.35), the primary variables, namely the displacements, pore pressure and electrical potential, are coupled through the governing equations at large strain. The mechanical equilibrium, mass balance of water and mass balance of electric charge, i.e. Eqs. (4.10), (4.19) and (4.20), can then be recast in weak form as follows:

$$\begin{aligned} & \int_{V^t} \mathbf{D}_{ep} \cdot d\varepsilon \cdot \delta\varepsilon dV^t + \int_{V^t} (d\boldsymbol{\Omega} \cdot \boldsymbol{\sigma}'^t + \boldsymbol{\sigma}'^t \cdot d\boldsymbol{\Omega}^T) \cdot \delta\varepsilon dV^t \\ & + \int_{V^t} \mathbf{I} d p \delta\varepsilon dV^t + \int_{V^t} \boldsymbol{\sigma}^t \cdot \delta\boldsymbol{\eta} dV^t = \int_{V^t} \mathbf{b}^{t+\Delta t} \cdot \delta\mathbf{u} dV^t \\ & + \int_{S^t} \mathbf{t}^{t+\Delta t} \cdot \delta\mathbf{u} dS^t - \int_{V^t} \boldsymbol{\sigma}^t \cdot \delta\varepsilon dV^t \quad (4.40) \\ & \int_{V^t} \nabla \cdot \mathbf{v}^s \delta p dV^t + \int_{V^t} \left(\frac{k_w}{\gamma_w} \nabla(p + \gamma_w z) + k_{eo} \nabla V \right) \cdot \nabla \delta p dV^t = 0 \\ & \int_{V^t} (k_{\sigma e} \nabla V) \cdot (\nabla \delta V) dV^t = 0 \end{aligned}$$

where $\delta \mathbf{u}$, δp and δV are the virtual displacements, virtual pore water pressure and virtual electric potential, respectively. The global governing equations are solved using the classical finite element method (Smith and Griffiths, 2004), and the spatial and time discretization of the governing equations are the same as presented in Section 3.3 of Chapter 3.

4.4. NUMERICAL SIMULATIONS

In this section, the proposed formulation is validated and tested in the analysis of several numerical examples. Firstly, the proposed large strain model is validated against experimental data. As mentioned previously, no suitable numerical solutions exist for the problem of large strain electro-osmosis consolidation, and few analytical solutions and documented experiments have been developed or performed. However, one example is the 1D electro-osmosis consolidation cell test reported by Feldkamp and Belhomme (1990). The experimental cell contained a colloidal silica column that was subjected to large strain electro-osmosis consolidation. The numerical results of an elasto-plastic simulation at large strain, with evolving hydraulic conductivity and electro-osmosis permeability, are here validated through comparison with the experimental results.

In a second numerical test, another large strain 1D model is investigated. This example highlights the difference between small and large strain analyses of elastic electro-osmosis consolidation. Then, in a third numerical test, the elasto-plastic behaviour of a 2D plane strain model employing the Modified Cam Clay constitutive model, as well as void ratio dependent hydraulic conductivity, electro-osmosis permeability and electrical conductivity, is investigated for a large strain electro-osmosis consolidation problem. The results illustrate the importance of the elasto-plastic formulation and void ratio dependent electrical conductivity in the simulation of electro-osmosis consolidation. Finally, a field test of electro-osmosis treatment is simulated for further verification; this example demonstrates that the current intermittence and current reversal which were used during the field test can be simulated by the proposed approach.

In all examples, an eight-node quadrilateral finite element is adopted for displacements, and this is coupled to a four node quadrilateral element for modelling excess pore water pressure and electrical potential. The flow due to gravity is neglected in the first three examples, since the problem size is small in each case.

4.4.1. ELECTRO-OSMOSIS TEST ON A COLLOIDAL SILICA COLUMN

Feldkamp and Belhomme's (1990) experiment comprised a column of Plexiglas, 30.5 cm in length and of 7.5 cm internal diameter, packed with colloidal silica. Figure 3.1 is representation of a cross-section through the silica specimen, as well as the assumed boundary conditions used for the present analysis. The domain is divided into 100 elements with a size of 1.5×1.525 cm. Displacements are prevented at the bottom of the sample, the left and right boundaries are restrained only in the horizontal direction, and the top of the sample is free. The hydraulic boundary conditions are free drainage at the top surface, whereas the remaining boundaries are impermeable. The cathode is the top boundary, the anode is the bottom boundary, and the left and right boundaries are impermeable with respect to electrical potential. As in the experiment, the electric

current is fixed at 0.104 A (corresponding to a current density of 23.5 A/m²), although it was reported that the applied voltage dropped from around 44 V to 39.5 V during the experiment which lasted approximately 50 minutes. From the known current and initial voltage, the initial electrical conductivity is calculated to be 0.163 S/m. Also, as in the experiment, a back pressure of 179 kPa is applied throughout the test to avoid possible cavitation issues during negative pore pressure development.

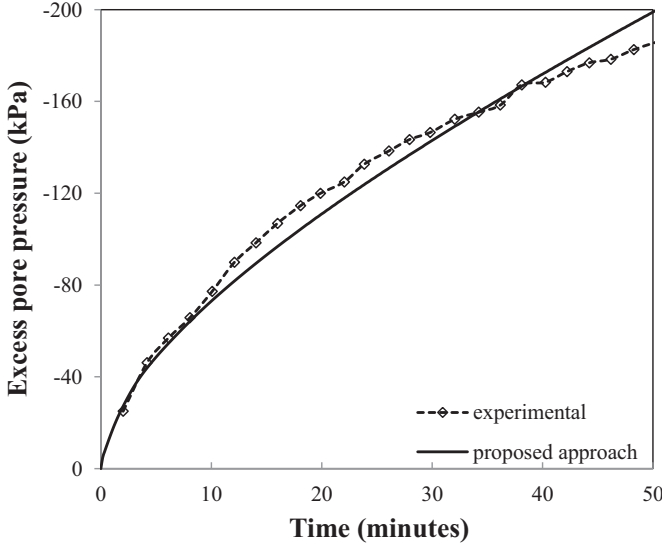


Figure 4.1: Numerical results and experimental measurements of excess pore pressure at the anode versus time.

With regard to the material properties, the hydraulic conductivity and electro-osmosis permeability of the colloidal silica were reported to be (Feldkamp and Belhomme, 1990):

$$\begin{aligned} k_w &= 1.4 \times 10^{-11} \frac{e^{2.54}}{1+e} \\ k_{eo} &= 3.0 \times 10^{-8} \left(\frac{1+e}{15.89} \right)^{1.36} \end{aligned} \quad (4.41)$$

in which $e = 15.0$ at the start of the test. Feldkamp and Belhomme (1990) obtained the relationship for k_w through direct experimentation, whereas the relationship for k_{eo} was derived by curve fitting against the experimental results. The Modified Cam Clay model is used here to describe the constitutive relationship and the following parameters are used: plastic compression index, $\lambda = 3.87$, which has been back-calculated from the test results; unloading–reloading index, $\kappa = \lambda/5 = 0.774$; friction constant, $M = 0.772$, which corresponds to an assumed friction angle of 20°; and Poisson's ratio, $\nu = 0.3$.

The computed development of negative excess pore pressure at the anode, during electro-osmosis consolidation, is compared with the experimental results of Feldkamp

and Belhomme (1990) in Figure 4.1. There is excellent agreement, indicating that the proposed numerical model is correctly modelling the coupled problem.

4.4.2. 1D ELECTRO-OSMOSIS CONSOLIDATION

The second example involves the 1D elastic consolidation of a vertical soil column due to an applied electrical potential at the bottom boundary. This is presented to further verify the proposed numerical model, by comparing the simulation results with small strain results. The soil column is 1 m high and is subjected to an electrical potential of 10 V at the anode. The boundary conditions are the same as for the first example (Figure 3.1). The material parameters used for the large strain and small strain models are listed in Table 4.1, and are based on the initial conditions for Mohamedelhassan and Shang's (2002) tests.

Table 4.1: Material parameters used in second example (after Mohamedelhassan and Shang (2002))

Initial void ratio	e	3.95
Young's modulus	E	2.0×10^5 Pa
Poisson's ratio	ν	0.3
Hydraulic conductivity	k_w	1.72×10^{-8} m/s
Electro-osmosis permeability	k_{eo}	1.47×10^{-8} m ² /(V·s)
Electric conductivity	$k_{\sigma e}$	0.802 S/m

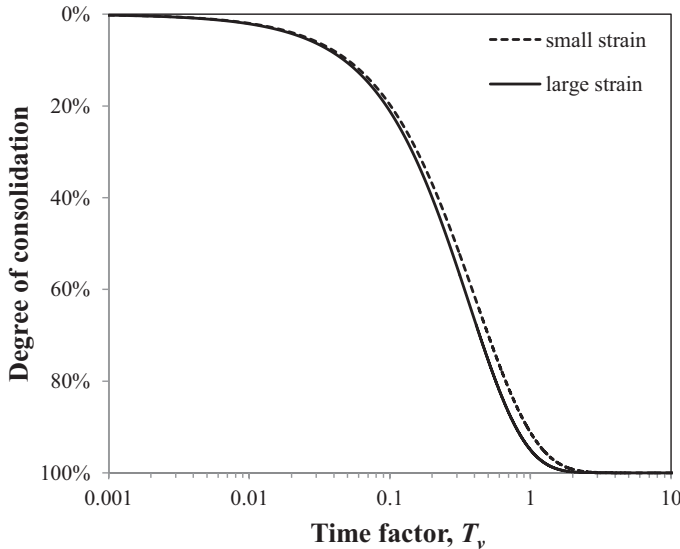


Figure 4.2: Average degree of consolidation versus time factor for 1D consolidation by electro-osmosis.

Figure 4.2 shows the average degree of consolidation versus the time factor, defined by $T_v = k_w \cdot t / (\gamma_w \cdot m_v \cdot L^2)$, in which m_v is the coefficient of compressibility and L is the

drainage path length. The large strain model predicts a faster rate of consolidation than the small strain model, partly due to it considering the geometric stiffness matrix which makes the stiffness strain dependent, but mainly because geometry changes are taken into account so that the drainage path length reduces with time (i.e. in contrast to the small strain model in which it remains constant).

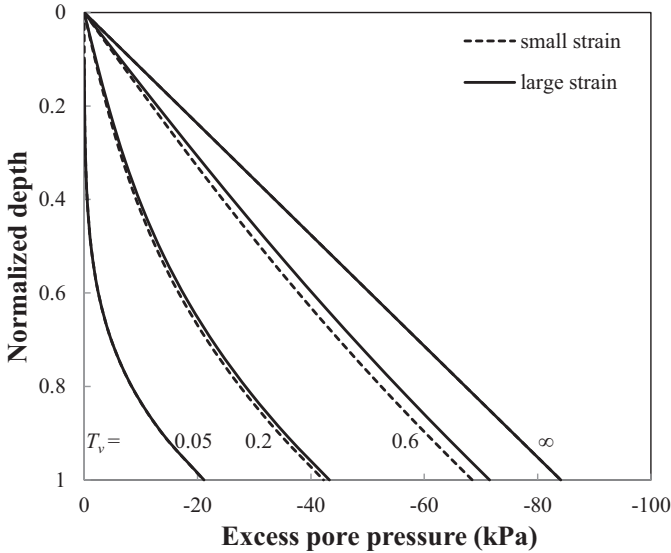


Figure 4.3: Excess pore pressure versus normalized depth for various time factors.

The excess pore pressure distributions with depth (where the deformed mesh has been normalized against the current column height), for various time factors, are presented in Figure 4.3. The large strain model predicts a faster development of the excess pore water pressure than the small strain model. This is due to both the strain dependent stiffness of the large strain model and the geometry change accounted for in the large strain model that makes the electrical gradient greater than in the small strain model (in which the geometry is constant). As can be seen in Figure 4.3, although the pore pressure distributions for both models are similar near the start of the consolidation (i.e. $T_v = 0.05$), as the consolidation progresses the large strain results deviate from the small strain model (i.e. $T_v = 0.2, 0.6$). However, both models predict the same excess pore pressure profile at the steady state, since, as explained by [Yuan and Hicks \(2013\)](#), the final excess pore pressure is controlled only by the voltage applied if the hydraulic conductivity and electro-osmosis permeability remain constant. Moreover, because of this both models predict a linear final pore pressure distribution between the electrodes.

The settlements show similar changes with time factor to the excess pore pressure, due to the coupling of the pore water and soil skeleton; that is, the decrease in pore pressure coincides with an increase in effective stress and so to an increase in soil deformation. As shown in Figure 4.4, the large strain model gives smaller final settlements than the small strain model, because the large strain model takes account of the geometry

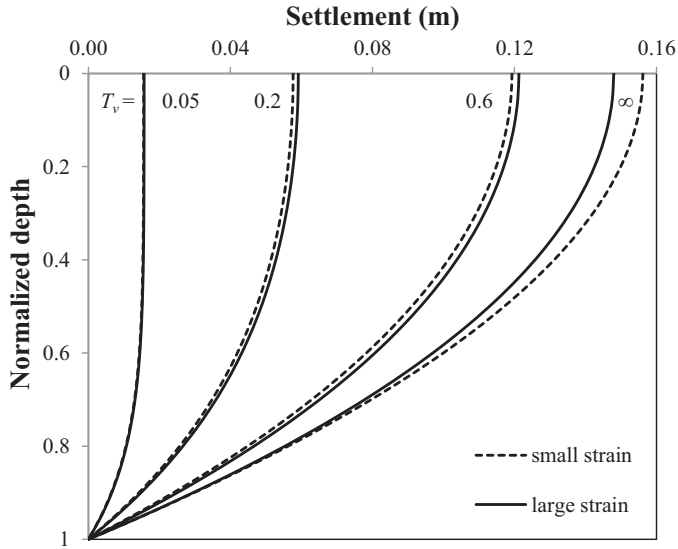


Figure 4.4: Settlement versus normalized depth for various time factors.

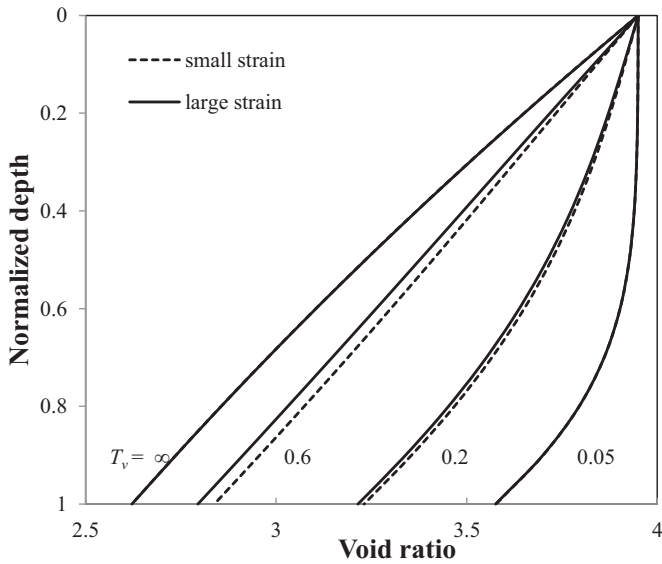


Figure 4.5: Void ratio versus normalized depth for various time factors.

dependent nonlinear stiffness as reported by [Yuan and Hicks \(2013\)](#).

The changes in void ratio result from the increase in effective stress in the soil sample. Figure 4.5 shows that the void ratio decrease occurs mainly near the anode, as this is

where the largest negative pore pressures develop. Notice that the final void ratios are the same in both models, due to the final pore pressure profiles being the same for the two models.

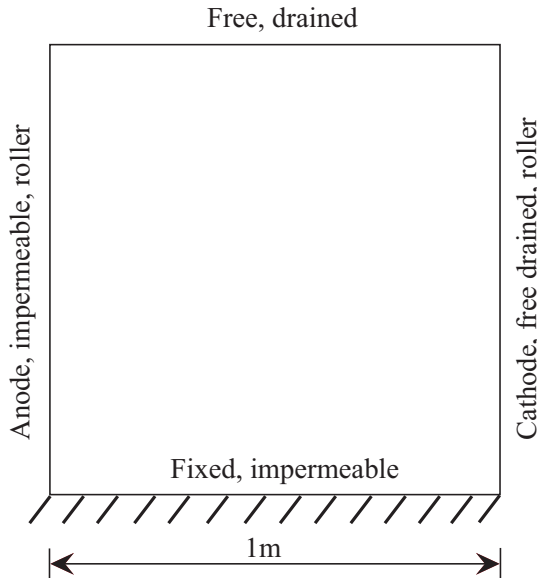


Figure 4.6: 2D electro-osmosis consolidation model.

4.4.3. 2D ELASTO-PLASTIC ELECTRO-OSMOSIS CONSOLIDATION

A square domain of side length 1 m is presented in Figure 4.6 and is used here to investigate elasto-plastic clay behaviour during electro-osmosis consolidation. The domain is discretized into 100 elements with a uniform size of 0.1×0.1 m. The boundary conditions are as follows: the left edge is impermeable and on rollers allowing only vertical movement; the right edge is free draining and on rollers allowing only vertical movement; the bottom boundary is impermeable and fixed; and the top surface is free draining. In terms of electric boundary conditions: the anode is along the left edge, the right edge is the cathode, and the horizontal boundaries are impermeable to electric current. An electric potential of 5 V is applied at the anode. The material parameters are selected from laboratory tests on the electro-osmosis of a marine sediment, carried out by [Mohamedelhassan and Shang \(2002\)](#), including the following empirical expressions:

$$\begin{aligned}
 \log k_w &= 1.1075e - 11.297 \\
 k_{eo} &= 3.27 \times 10^{-8}n - 1.14 \times 10^{-8} \\
 k_{\sigma e} &= \frac{0.42(1+e)}{1.29 + 0.33e}
 \end{aligned}
 \tag{4.42}$$

The material parameters for the Modified Cam Clay model are listed in Table 4.2, and are also derived from Mohamedelhassan and Shang's (2002) laboratory tests. The initial

effective stresses have been assigned using the effective unit weight of the soil and the coefficient of earth pressure at rest. However, to avoid potential numerical problems at very low stresses, a minimum effective stress of 1 kPa is assumed. The initial yield surface location is then determined according to the effective pressure and assumed over-consolidation ratio (OCR). Finally, the electric potential is applied at the anode and the displacements and pore water pressure changes due to the consolidation processes are computed.

Table 4.2: Material parameters for the Modified Cam Clay model (after [Mohamedelhassan and Shang \(2002\)](#))

void ratio at $p' = 1$ kPa	e	3.95
Poisson's ratio	ν	0.3
Plastic compression index	λ	0.547
Unloading-reloading index	κ	0.064
Critical stress ratio	M	1.172
Over-consolidation ratio	OCR	1.0
Coefficient of earth pressure at rest	K_0	1.0
Total unit weight of soil	γ	14 kN/m ³

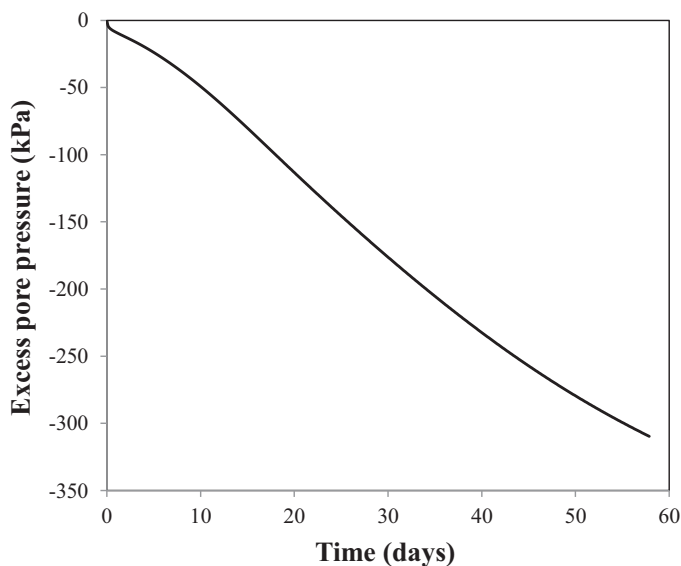


Figure 4.7: Excess pore pressure versus time at the base of the anode.

The excess pore pressure versus time relationship at the base of the anode is shown in Figure 4.7. (Note that the current model formulation does not set a limit on the tensile pore pressures generated; for example, to account for the effects of cavitation.) The development of negative pore pressure changes results in an increase in the effective stress, which causes a decrease in the void ratio. Theoretically, the magnitude of the

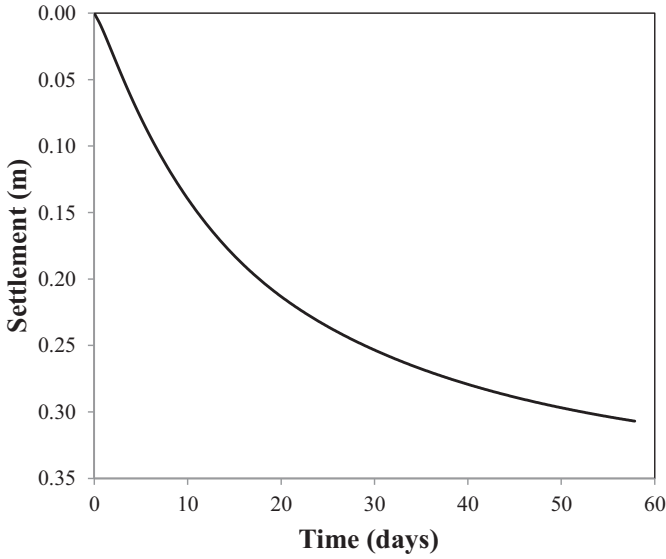


Figure 4.8: Settlement versus time at the top of the anode.

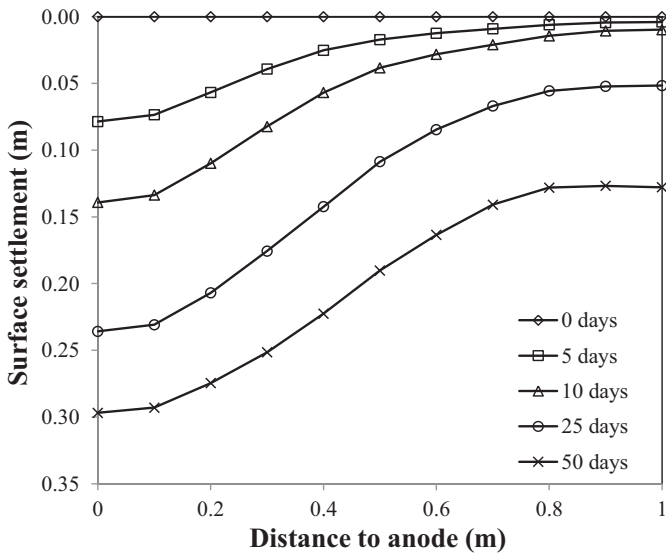


Figure 4.9: Surface settlement relative to the anode at different times.

electro-osmosis consolidation is governed by the ratio of the electro-osmosis permeability and hydraulic conductivity (k_{eo}/k_w) of the soil, it being greater for larger values of k_{eo}/k_w . Normally, the decrease of hydraulic conductivity is much faster than the de-

crease of electro-osmosis permeability with void ratio. Therefore, the ratio k_{eo}/k_w increases with the decrease in void ratio, so that larger excess pore pressures develop (albeit more slowly) than for a constant k_{eo}/k_w .

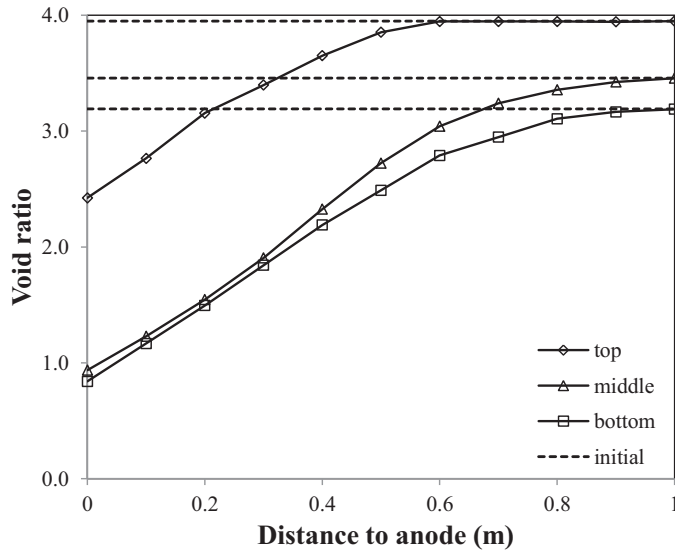


Figure 4.10: Final void ratio profile relative to the anode at different depths.

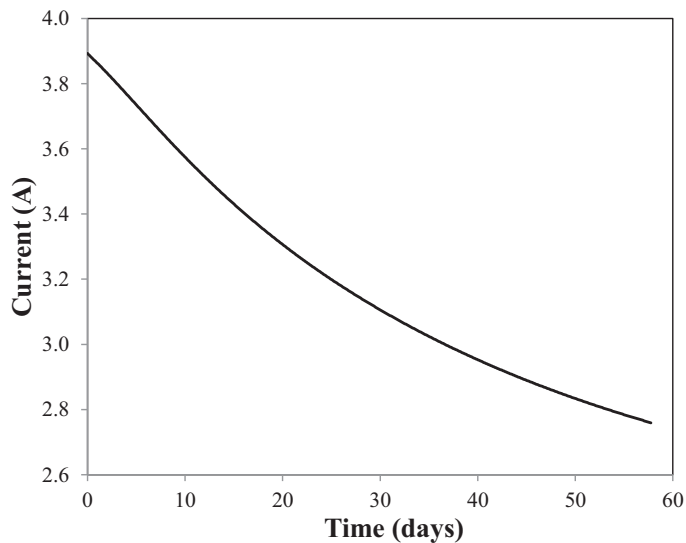


Figure 4.11: Electric current versus time relationship.

Figure 4.8 illustrates the evolution of settlement at the top of the anode. It shows that large settlements are observed, even though the equilibrium state has not been reached after 60 days, demonstrating that large strain theory is necessary for electro-osmosis consolidation. Figure 4.9 shows the settlement profiles of the top surface for different times. The settlements are mainly developed near the anode and, as the time increases, the difference in settlement between the locations of the two electrodes becomes larger. As already mentioned, the deformation is controlled by the excess pore pressure due to the coupling behaviour between the pore water and soil skeleton, and the largest negative excess pore pressures are developed near the anode. Similarly, Figure 4.10 shows that the void ratio decrease mainly occurs near the anode. In contrast, the void ratio decrease near the cathode is negligible. Note that the initial void ratio is larger at the top of the domain than at the middle and bottom, and that the final void ratios at the middle and bottom of the layer near the anode are almost the same. This is because the region with the maximum negative excess pore pressure extends from the bottom to the middle of the soil domain, in the region near the anode, which means that the effective stresses are almost the same in that region.

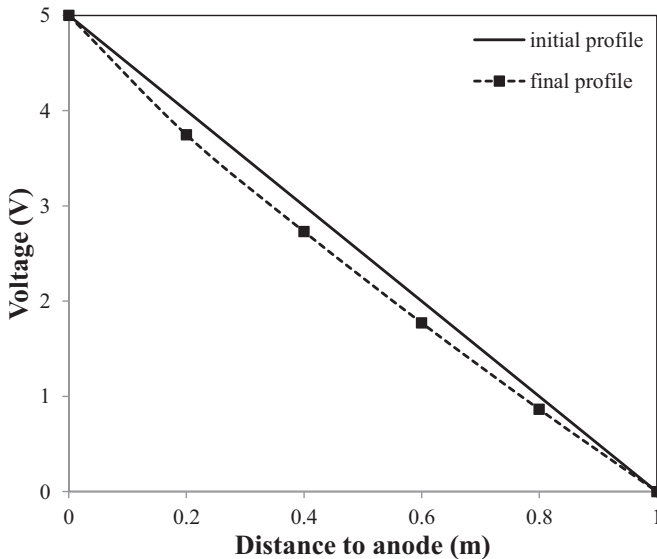


Figure 4.12: Voltage profile along the bottom boundary relative to the anode.

The electric current through the sample is plotted as a function of time in Figure 4.11, revealing that the current reduces from around 3.9 A to less than 2.8 A during the simulation period. This is due to the void ratio decrease, during consolidation, causing an increase in the sample's resistance to the flow of electrical current. Figure 4.12 shows the initial and final voltage distributions along the bottom boundary between the two electrodes. The voltage drop near the anode is due to the electrical conductivity decreasing with the increase of effective stress and is consistent with the findings of laboratory investigations (Mohamedelhassan and Shang, 2001; Lefebvre and Burnotte, 2002). How-

ever, the voltage loss is not that significant, because, according to Eq. (4.42), the electric conductivity does not decrease rapidly with decreasing void ratio.

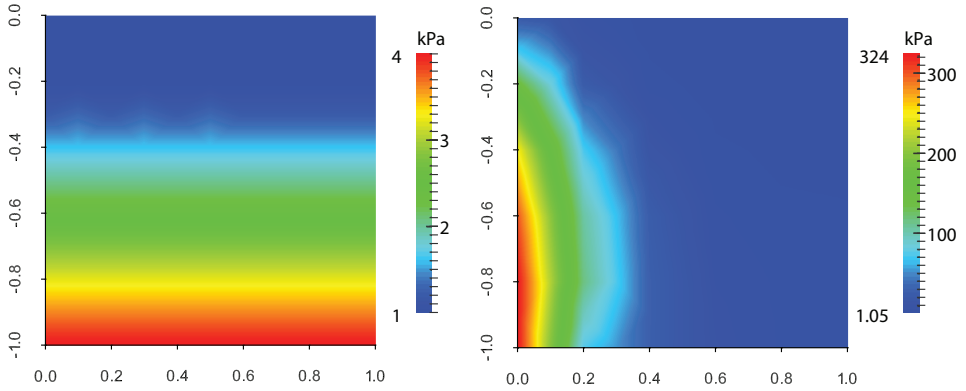


Figure 4.13: Pre-consolidation pressure distributions: initial (left) and final (right).

Figure 4.13 presents the initial and final pre-consolidation pressure distributions, in which the pre-consolidation pressure is defined by p_c in Eq. (4.22). It is seen that the gain in pre-consolidation pressure is much higher near the bottom of the anode than elsewhere. As the total vertical stress was kept constant during the electro-osmosis consolidation, the increase in pre-consolidation pressure is approximately equal to the negative excess pore pressure developed. It is also noted that the increase in pre-consolidation pressure near the top of the anode is much bigger than near the cathode, where only a slight increase is observed. It is found that, by applying electro-osmosis consolidation, the strength improvement is not uniform; in this illustration, it is very efficient near the anode, but has almost no effect near the cathode.

4.4.4. NUMERICAL STUDY OF A FIELD TEST

A field test involving the electro-osmosis treatment of a Norwegian quick clay, reported by Bjerrum et al. (1967), is simulated using finite element analysis to further verify the proposed numerical model. The test site was located in As, 30 km south of Oslo, Oslofjord, Norway. The test involved the installation of electrodes, of 10 m length and 19 mm diameter, arranged in 10 rows spaced 2 m apart. In each row, the electrodes (anodes or cathodes) were positioned at a spacing of 0.6-0.65 m. They were pushed into the ground to a depth of about 9.6 m, leaving 0.4 m above the ground, and three displacement gauges (S1, S2 and S3) were installed between the 4th and 5th electrode rows at depths of 1, 4 and 8 m, respectively. The DC voltage was applied for 120 days, but with current intermittence and polarity reversal.

The entire treatment area was subdivided into isolated repetitive areas, and so a 2D plane strain model is here adopted to simulate one repetitive area, as shown in Figure 4.14. Note that the consolidation in the weathered crust making up the top 2 m is neglected, since it is a fairly stiff layer due to drying and weathering effects. Therefore, a rectangular domain of 2 m width and 7.6 m depth is simulated, with one impermeable anode and one drained cathode, as seen in the figure. The geotechnical properties of

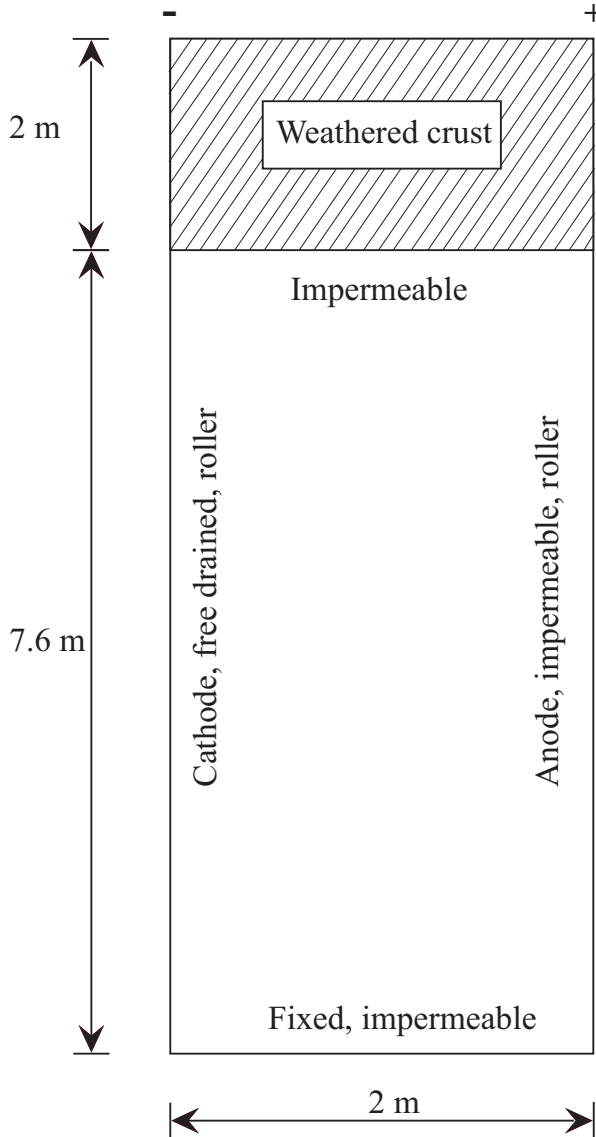


Figure 4.14: Geometry and boundary conditions of the 2D model.

the soft clay, given in Table 4.3, are obtained directly from Bjerrum et al. (1967), as are the electro-osmosis and hydraulic properties. Although Modified Cam Clay parameters were not stated in the paper, the plastic compression index λ has been back-calculated from the given compression index, $C_c = 0.4$, using the relationship $\lambda = C_c/2.3 = 0.174$. Moreover, the ratio λ/κ generally varies in the range 5 to 10; in this analysis 6 is chosen, so that $\kappa = 0.029$. For triaxial compression, the friction constant M is calculated from

the relationship $M = 6\sin\phi/(3-\sin\phi)$; by assuming a friction angle of 15° , $M = 0.567$. The Poisson's ratio is assumed be 0.3, whereas the initial effective stress and approximated preconsolidation pressure were given by Bjerrum et al. (1967), and are shown in Figure 4.15.

Table 4.3: Properties of soft clay (after Bjerrum et al. (1967))

Natural water content	w	31%
Plastic limit	w_p	14%
Liquid limit	w_L	19%
Plastic index	I_p	5%
Clay content $< 2 \mu m$		37%
Content of organic matter		0.9%
Specific gravity	G_s	2.75
Compression index	C_c	0.4
Hydraulic conductivity	k_w	2×10^{-10} m/s
Electro-osmosis permeability	k_{eo}	2×10^{-9} m ² /(V·s)
Electric conductivity	$k_{\sigma e}$	0.0213 S/m

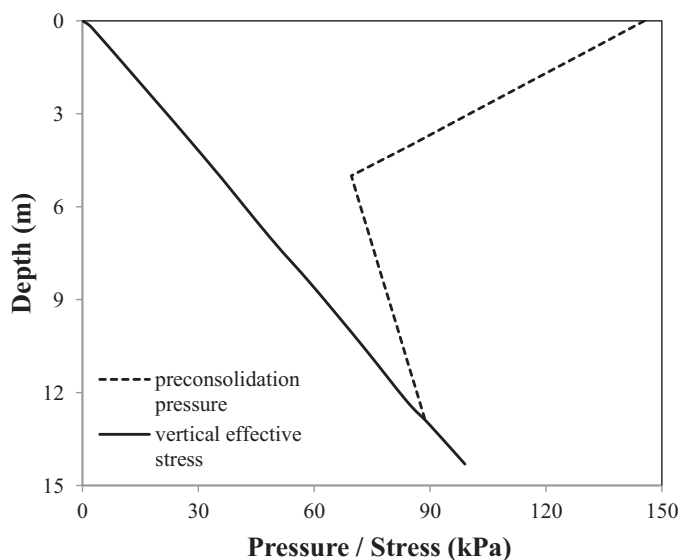


Figure 4.15: Approximated initial effective stress and preconsolidation pressure profiles (after Bjerrum et al. (1967)).

The applied voltage was not constant during the field test, since current intermittence and polarity reversal were considered. The applied voltage in the field test and the approximated input voltage are shown in Figure 4.16. The voltage between the electrodes was measured on days 8, 52 and 80, and revealed a considerable potential drop

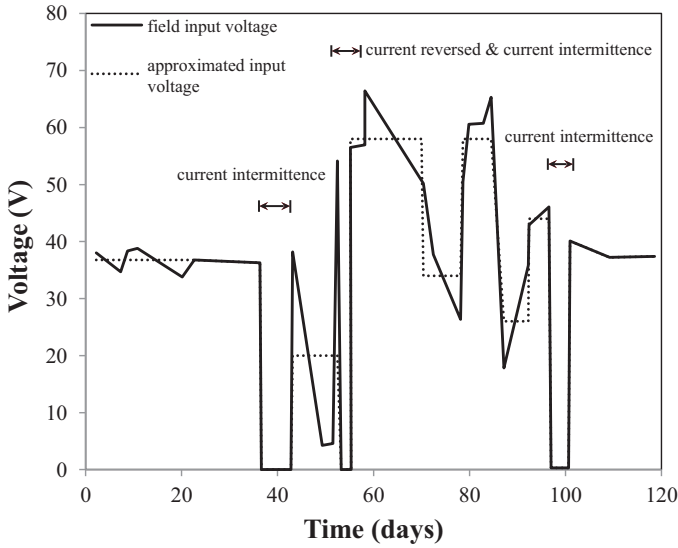


Figure 4.16: Applied field and approximated input voltages versus time (after Bjerrum et al. (1967)).

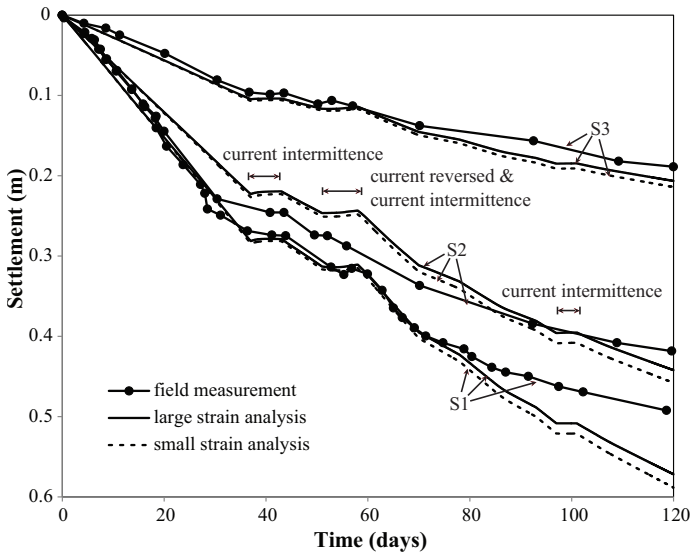


Figure 4.17: Computed and measured settlement versus time at different depths.

within 10 cm of the electrodes. During the numerical simulation, the efficiency of the input voltage is considered to be approximately 75 % before day 52, and 50 % during days 52 to 120, based on the field measurements. This has been implemented by reducing the

input voltage to the relevant value during these periods.

The settlements at depths of 1, 4 and 8 m, computed in the large strain and small strain numerical analyses, as well as the field data from settlement gauges S1, S2 and S3 installed half way between the anode and cathode, are shown in Figure 4.17. The results show that consideration of geometrical nonlinearity causes a reduction in the settlements relative to the small strain simulation, and that this effect increases with time as the consolidation progresses. However, the differences between the two solutions is relatively small in this example. This is because, although the settlements are as high as 0.6 m, the strains are only moderate ($\approx 8\%$) due to the overall thickness of the layer.

Figure 4.17 shows excellent agreement between the computed and measured settlements, especially for the first 70 days of the treatment period, at depths of 1 m and 8 m. However, the computed settlement at 4 m depth is smaller than the measured settlement. The computed settlements are larger than the measured values between days 70 and 120, at both 1m and 8 m depth. Finally, current intermittence and current reversal are considered in the analysis. As can be seen in Figure 4.17, the impact of the current intermittence between days 37 and 43, and the current intermittence and reversal between days 51 and 58, have been well reproduced by the numerical simulation.

4.5. CONCLUSIONS

A formulation for the consideration of large strain elasto-plastic electro-osmosis consolidation has been presented. Three coupled governing equations for force equilibrium, pore water transport and electrical transport are derived and solved using finite elements. The elasto-plastic behaviour of clay is considered by employing the Modified Cam Clay constitutive model and nonlinear variations in soil transport parameters are incorporated by introducing a dependence of the absolute soil conductivity or permeability (with respect to hydraulic, electro-osmosis and electrical model components) on void ratio.

The proposed approach has been verified against a 1D large strain electro-osmosis consolidation test and the numerical results show good agreement with the experimental data. Following the verification, the performance and applicability of the approach has been demonstrated via three further numerical examples. A simple 1D numerical simulation was conducted and evaluated, to highlight the influence of considering large strain during electro-osmosis consolidation. An idealized 2D electro-osmosis consolidation problem, using the Modified Cam Clay constitutive relationship, was then investigated. Changes in void ratio, and consequent changes in the coefficients of hydraulic conductivity and electro-osmosis permeability during the electro-osmosis consolidation, could not be neglected, because the coefficients of hydraulic conductivity and electro-osmosis permeability are two of the dominating factors in the consolidation process. Furthermore, the voltage and current distributions were investigated, by considering the change in the electrical conductivity. It was demonstrated that the voltage drop near the anode, and the current decrease during electro-osmosis which has been found in many laboratory tests, can be simulated by the proposed model. Moreover, the strength improvement in the clay during the electro-osmosis was quantified. A significant improvement in the pre-consolidation pressure was found in the vicinity of the anode. Finally, a field test of electro-osmosis treatment was analyzed, to further

demonstrate the capability of the proposed numerical model. The computed settlement at different depths showed good agreement with the measured data.

The presented numerical examples have demonstrated that the modelling of electro-osmosis consolidation has to be performed carefully, according to realistic conditions. Hence the consideration of large strain elasto-plastic mechanical behaviour and nonlinear soil transport properties is often necessary.

5

LARGE STRAIN ELASTO-PLASTIC ELECTRO-OSMOSIS CONSOLIDATION OF UNSATURATED CLAYS

This chapter presents a numerical model for the elasto-plastic electro-osmosis consolidation of unsaturated clays experiencing large strains, by considering electro-osmosis and hydro-mechanical flows in a deformable multiphase porous medium. The coupled governing equations involving the pore water flow, pore gas flow, electric flow and mechanical deformation in unsaturated clays, are derived within the framework of averaging theory and solved numerically using finite elements. The displacements of the solid phase, the pressure of the water phase, the pressure of the gas phase and the electric potential are taken as the primary unknowns in the proposed model. The nonlinear variation of transport parameters during electro-osmosis consolidation are incorporated into the model using empirical expressions that strongly depend on the degree of water saturation, whereas the Barcelona Basic Model is employed to simulate the elasto-plastic mechanical behaviour of unsaturated clays. The accuracy of the proposed model is evaluated by validating it against two well-known numerical examples, involving electro-osmosis and unsaturated soil behaviour, respectively. Two further examples are then investigated to study the capability of the computational algorithm in modelling multiphase flow in electro-osmosis consolidation. Finally, the effects of gas generation at the anode, the deformation characteristics, the degree of saturation and the time dependent evolution of the excess pore pressure are discussed.

5.1. INTRODUCTION

For the approximation of large strain geotechnical consolidation, Biot first developed the classical theory of large strains in an elastic porous medium (Biot, 1941). There then followed a number of large strain models in the literature (Carter et al., 1977, 1979; Borja and Alarcón, 1995; Borja et al., 1998; Li et al., 2004; Nazem et al., 2008), in which the majority of papers focused on fully saturated conditions. Fewer numerical solutions exist for unsaturated soils, although coupled analyses for unsaturated soil under dynamic loading were presented by Meroi et al. (1995) and Sanavia et al. (2002) formulated an unsaturated model for a porous medium undergoing large inelastic strains. These unsaturated models were based on the common assumption that the gas pressure is uniform and at atmospheric pressure in the unsaturated zone. Recently, Uzuoka and Borja (2012) went one step further in incorporating unsaturation into their formulation, by treating pore gas pressure as a primary variable at large strain.

The analytical and numerical models for electro-osmosis consolidation usually assumed that the soil is saturated during the consolidation process. However, Tamagnini et al. (2010) recently presented a numerical model for electro-osmosis consolidation, accounting for gas generation and transport under unsaturated conditions. Laboratory tests and field applications are usually performed on saturated soil, to study the transport parameters as well as the mechanical properties of electro-osmosis consolidation. In contrast, unsaturated soil conditions have seldom been investigated, although desaturation is often found near the anode, caused by, for example, negative pore water pressure development and gas generation and transport. Under unsaturated conditions, soil transport parameters involving electro-osmosis changes are strongly dependent on the degree of water saturation, as has been reported in some pilot electro-osmosis experiments under unsaturated conditions (Mattson et al., 2002a,b; Wieczorek et al., 2005; Chang et al., 2006). This influence may be significant and should not be ignored.

This chapter develops a numerical model for the finite element solution of the coupled multiphase system in unsaturated porous media at large strain. The novel feature of the proposed approach is the consideration of unsaturated elasto-plastic mechanical behaviour. The fully coupled governing field equations considering force equilibrium, pore water transport, pore gas transport and electrical current flow are derived based on averaging theory and solved, via the finite element method in the space domain and an implicit integration scheme in the time domain. Moreover, for the fluids, various relationships between the transport parameters, degree of water saturation and selected experimentally determined suction function are incorporated into the proposed model. A Bishop type effective stress is used to establish the coupling between the deformation and flow processes in unsaturated conditions. The Barcelona Basic Model (BBM) (Alonso et al., 1990) is introduced into the proposed formulation to simulate the mechanical behaviour of unsaturated clays.

The chapter is organized as follows. Section 5.2 gives a brief description of the governing equations for the constitutive relationships of the different phases, as well as the background to large strain theory. Then, a detailed discretization procedure, including the governing equations in matrix form and their time integration, is introduced in Section 5.3. Finally, in Section 5.4, the proposed computational algorithm is first validated by solving two idealized examples and comparing the numerical results with analytical

solutions. These are followed by further numerical examples to investigate and demonstrate the performance of the proposed model.

5.2. GOVERNING EQUATIONS AT LARGE STRAIN

5.2.1. BASIC ASSUMPTIONS

The governing equations for the equilibrium of force, hydraulic head, pore gas pressure and electric potential are derived based on the following assumptions: (1) the governing balance equations for multiphase flow are based on averaging theories; (2) an isotropic unsaturated soil with incompressible soil particles; (3) the coupled conduction processes occur under isothermal conditions; (4) the effect of electrical–chemical reactions is negligible except for electrolysis at the electrodes; (5) electrophoresis and streaming currents are negligible; (6) the flow of fluid due to the electrical and hydraulic gradients may be superimposed to obtain the total flow; (7) Darcy’s law is valid; (8) Ohm’s law is valid.

5.2.2. KINEMATIC AND DEFORMATION EQUATIONS

In a multiphase porous medium, consider an arbitrary reference configuration for the π phase with coordinates \mathbf{X}^π , which has position \mathbf{x}^π at time t . The mapping function φ^π relates the initial and current position vectors. Hence, for a typical time step, the updated configuration of the body may be written as

$$\mathbf{x}^\pi = \varphi^\pi(\mathbf{X}^\pi, t) \quad (5.1)$$

The current and fixed reference configurations are related to each other by the displacement \mathbf{u}^π , via the equation

$$\mathbf{x}^\pi = \mathbf{X}^\pi + \mathbf{u}^\pi \quad (5.2)$$

A fundamental measure of the deformation is given by the deformation gradient, defined as

$$\mathbf{F}^\pi = \frac{\partial \varphi^\pi}{\partial \mathbf{X}^\pi} = \frac{\partial \mathbf{x}^\pi}{\partial \mathbf{X}^\pi} \quad (5.3)$$

The change in volume between the reference and current configurations can be established as

$$dV^\pi = J^\pi dV_0^\pi \quad (5.4)$$

where V_0^π and V^π are the reference and current volumes respectively, and J^π is the Jacobian determinant which is the determinant of the deformation gradient \mathbf{F}^π . The Green strain tensor is given as

$$\mathbf{E} = \frac{1}{2}(\mathbf{F}^T \mathbf{F} - \mathbf{I}) \quad (5.5)$$

where \mathbf{I} is a unit tensor. In order to compute the Cauchy stress $\boldsymbol{\sigma}$, the second Piola–Kirchhoff stress \mathbf{S} measured at the reference configuration has to be computed first. The Cauchy stress is related to the second Piola–Kirchhoff (PK2) stress by the deformation gradient as follows:

$$\boldsymbol{\sigma} = \frac{1}{J} \mathbf{F}^T \mathbf{S} \mathbf{F} \quad (5.6)$$

The spatial velocity \mathbf{v}^π of the material point \mathbf{x}^π is given by

$$\mathbf{v}^\pi = \mathbf{v}^\pi(\mathbf{x}^\pi, t) = \frac{\partial \mathbf{x}^\pi}{\partial t} \quad (5.7)$$

For an arbitrary scalar valued function $f^\pi(\mathbf{x}^\pi, t)$, its material time derivative, given in its spatial description and referring to a moving particle of the π phase, is defined by

$$\frac{D^\pi f^\pi}{Dt} = \frac{\partial f^\pi}{\partial t} + \nabla f^\pi \cdot \mathbf{v}^\pi \quad (5.8)$$

In a multiphase porous medium, it is common to assume the motion of the solid configuration as a reference and to describe the motion of the π phase particles relative to the solid. So, the water relative velocity can be written as

$$\mathbf{v}^{ws} = \mathbf{v}^w - \mathbf{v}^s \quad (5.9)$$

where superscripts w and s refer to the water and solid phases, respectively. Similarly, the relative velocity of the pore gas can be expressed as

$$\mathbf{v}^{gs} = \mathbf{v}^g - \mathbf{v}^s \quad (5.10)$$

where superscript g refers to the gas phase. By considering the above relative velocities, the material time derivative of f^π with respect to the moving solid phase is written as

$$\frac{D^s f^\pi}{Dt} = \frac{D^\pi f^\pi}{Dt} + \nabla f^\pi \cdot \mathbf{v}^{s\pi} \quad (5.11)$$

5.2.3. BALANCE LAWS

The mass balance law for the solid phase in the current configuration may be written as

$$\frac{D^s \rho_s}{Dt} + \rho_s \nabla \cdot \mathbf{v}^s = 0 \quad (5.12)$$

For the π phase material, the partial density of that phase is defined as the averaged density for the volume fraction η^π , i.e.

$$\rho_\pi = \eta^\pi \rho^\pi \quad (5.13)$$

where ρ_π is the average density and ρ^π is the intrinsic density in the current configuration. The volume fraction is related to porosity n , degree of water saturation S_w and degree of gas saturation S_g as follows:

$$\begin{aligned} \eta^s &= 1 - n \\ \eta^w &= n S_w \\ \eta^g &= n S_g \end{aligned} \quad (5.14)$$

with the saturation constraint, $S_w + S_g = 1$. Substituting Eqs. (5.13) and (5.14) into the mass balance equation of the solid skeleton (5.12) gives,

$$\frac{D^s(1-n)\rho^s}{Dt} + (1-n)\rho^s \nabla \cdot \mathbf{v}^s = 0 \quad (5.15)$$

Taking account of the incompressibility of the solid particles, partial differentiation of the mass balance equation leads to

$$-\frac{D^s n}{Dt} + (1-n)\nabla \cdot \mathbf{v}^s = 0 \quad (5.16)$$

The mass balance laws for the fluid and gas phases ($\pi = w, g$) can be expressed as follows:

$$\frac{D^\pi \rho_\pi}{Dt} + \rho_\pi \nabla \cdot \mathbf{v}^\pi = 0 \quad (5.17)$$

5.2.4. EQUILIBRIUM EQUATIONS

The equilibrium equation for the multiphase porous medium can be written as

$$\nabla \cdot \boldsymbol{\sigma} + \rho \mathbf{b} = \mathbf{0} \quad (5.18)$$

where $\boldsymbol{\sigma}$ is the total Cauchy stress vector, \mathbf{b} is the body force vector and ρ is the average density of the multiphase medium defined as $\rho = (1-n)\rho^s + n(S_w\rho^w + S_g\rho^g)$.

The stress relationship in the mechanics of unsaturated porous media is expressed through the concept of the modified effective stress, to take account of the coupling between the deformations of the soil skeleton and the pore pressures. Some review articles are available on this topic (Jommi, 2000; Gens et al., 2006; Sheng et al., 2008; Nuth and Laloui, 2008; Gens, 2010). One of the best known and commonly used definitions is Bishop's stress, which is expressed as

$$\boldsymbol{\sigma} = \boldsymbol{\sigma}' + \mathbf{I}\bar{p} \quad (5.19)$$

where $\boldsymbol{\sigma}'$ is the effective stress, \mathbf{I} is the identity vector and \bar{p} is the mean or averaging pore pressure, given by

$$\bar{p} = S_w p_w + S_g p_g \quad (5.20)$$

where p_w and p_g are the pore water pressure and pore gas pressure, respectively. Furthermore, the suction or capillary pressure, $s = p_g - p_w$, is introduced as the second constitutive variable for describing unsaturated soil behaviour in the Barcelona Basic Model (BBM). Bishop's expression was originally thought to serve as a single stress parameter concept, although, in unsaturated conditions, it fails when describing certain wetting and drying phenomena, e.g. the collapse of the soil upon wetting under constant effective stress. However, it does not require additional assumptions to take account of the shear strength increase with suction and the elastic volumetric strain due to change in suction. Moreover, the major advantage is that Bishop's stress provides a straightforward description of the transition between unsaturated and fully saturated conditions, without the need to change the global numerical formulation.

When assuming large strain kinematics, involving also large rotations, care must be taken to ensure the material frame invariance of the model. Based on the hypoelasticity framework, a frame-independent stress such as the Jaumann stress rate needs to be introduced, i.e (Nazem et al., 2008)

$$d\boldsymbol{\sigma}^J = d\boldsymbol{\sigma}' - d\boldsymbol{\Omega} \cdot \boldsymbol{\sigma}' - \boldsymbol{\sigma}' \cdot d\boldsymbol{\Omega}^T = \mathbf{D}_{ep} \cdot d\boldsymbol{\varepsilon} + \mathbf{W}_{ep} ds \quad (5.21)$$

where \mathbf{D}_{ep} is the elasto-plastic stress–strain matrix, \mathbf{W}_{ep} is the elasto-plastic suction–strain vector and $\boldsymbol{\varepsilon}$ is the strain vector. The Jaumann stress rate is related to the Cauchy stress rate by the non-objective spin tensor $\boldsymbol{\Omega}$, which may be given by

$$\boldsymbol{\Omega} = \frac{1}{2} [(\Delta \mathbf{u}) - (\Delta \mathbf{u})^T] \quad (5.22)$$

By substituting Eq. (5.21) into the effective stress equation, Eq. (5.19), the stress rate can be written as

$$d\boldsymbol{\sigma} = \mathbf{D}_{ep} \cdot d\boldsymbol{\varepsilon} + \mathbf{W}_{ep} dS + d\boldsymbol{\Omega} \cdot \boldsymbol{\sigma}' + \boldsymbol{\sigma}' \cdot d\boldsymbol{\Omega}^T + \mathbf{I} d\bar{p} \quad (5.23)$$

In the large strain formulation based on objective stress rates (i.e. Jaumann stress rates), the basic rate evolution law for the stress increment is (Nazem et al., 2006, 2009)

$$\boldsymbol{\sigma}'^{t+\Delta t} = \boldsymbol{\sigma}'^t + \int_0^{\Delta \boldsymbol{\varepsilon}} \mathbf{D}_{ep} \cdot d\boldsymbol{\varepsilon} + \int_0^{\Delta S} \mathbf{W}_{ep} dS + \int_0^{\Delta \boldsymbol{\Omega}} (d\boldsymbol{\Omega} \cdot \boldsymbol{\sigma}'^t + \boldsymbol{\sigma}'^t \cdot d\boldsymbol{\Omega}^T) \quad (5.24)$$

The hypoelasticity framework is adopted in this paper, as it has been proven that a Jaumann rate formulation is effectively equivalent to a multiplicative decomposition approach based on a hyperelasticity framework (de Souza Neto et al., 2008; De Borst et al., 2012), when the elastic strains remain small. If the increments are very small, the integration of the resulting rate equations should be close to the results of formulations that are based on multiplicative decomposition. This is exactly the case for the explicit stress integration scheme, where small increments are maintained by imposing a strict error control. An explicit stress integration scheme with automatic sub-stepping and error control for large strain is implemented here to solve the BBM unsaturated elasto-plastic constitutive model (Sheng et al., 2003a; Nazem et al., 2009; Solowski and Gallipoli, 2010).

5

5.2.5. MASS BALANCE EQUATIONS

The mass balance equations for the water and gas phases, based on the assumptions presented in Section 5.2.1, are derived in this section. They are augmented by the constitutive relationships that relate degree of water saturation to suction via a functional expression and relative velocities to pressure gradients via the generalized Darcy law.

By introducing the material time derivative with respect to the solid phase, the mass balance equation, Eq.(5.17), becomes

$$\frac{D^s \rho_\pi}{Dt} + \mathbf{v}^{\pi s} \cdot \nabla \rho_\pi + \rho_\pi \nabla \cdot \mathbf{v}^{\pi s} + \rho_\pi \nabla \cdot \mathbf{v}^s = 0 \quad (5.25)$$

Using the vector identity $\nabla \cdot (\rho_\pi \mathbf{v}^{\pi s}) = \mathbf{v}^{\pi s} \cdot \nabla \rho_\pi + \rho_\pi \nabla \cdot \mathbf{v}^{\pi s}$, and by introducing the intrinsic density with volume fraction via Eqs. (5.13) and (5.14), Eq. (5.25) may be transformed into

$$\frac{D^s (n S_\pi \rho^\pi)}{Dt} + \nabla \cdot (n S_\pi \rho^\pi \mathbf{v}^{\pi s}) + n S_\pi \rho^\pi \nabla \cdot \mathbf{v}^s = 0 \quad (5.26)$$

The mass balance of the pore water can be derived from Eq. (5.26) as follows:

$$S_w \rho^w \frac{D^s n}{Dt} + n \rho^w \frac{D^s S_w}{Dt} + n S_w \frac{D^s \rho^w}{Dt} + \nabla \cdot (n S_w \rho^w \mathbf{v}^{ws}) + n S_w \rho^w \nabla \cdot \mathbf{v}^s = 0 \quad (5.27)$$

Substituting Eq. (5.16) into Eq. (5.27) gives

$$n\rho^w \frac{D^s S_w}{Dt} + nS_w \frac{D^s \rho^w}{Dt} + \nabla \cdot (nS_w \rho^w \mathbf{v}^{ws}) + S_w \rho^w \nabla \cdot \mathbf{v}^s = 0 \quad (5.28)$$

Similarly, the mass balance equation for the gas phase can be written as

$$n\rho^g \frac{D^s S_g}{Dt} + nS_g \frac{D^s \rho^g}{Dt} + \nabla \cdot (nS_g \rho^g \mathbf{v}^{gs}) + S_g \rho^g \nabla \cdot \mathbf{v}^s = 0 \quad (5.29)$$

The constitutive equation for the pore water flow velocity in electro-osmosis comprises two components. One is the hydraulic flow caused by the gradients of pore water pressure and the other is the electro-osmosis flow caused by electrical potential gradients. The generalized Darcy's law gives

$$nS_w \mathbf{v}^{ws} = -\frac{\mathbf{k}_w k_{rw}}{\gamma_w} (\nabla p_w - \rho^w \mathbf{g}) - \mathbf{k}_{eo} k_{reo} \nabla V \quad (5.30)$$

where γ_w is the unit weight of the pore water, \mathbf{k}_w is the intrinsic hydraulic conductivity matrix, k_{rw} is the relative hydraulic conductivity coefficient, \mathbf{k}_{eo} and k_{reo} are the absolute and relative electro-osmosis permeability, respectively, and V is the electric potential. Similarly, the constitutive equation for the relative gas flow velocity results in the generalized Darcy's law,

$$nS_g \mathbf{v}^{gs} = -\frac{\mathbf{k}_g k_{rg}}{\gamma_g} (\nabla p_g - \rho^g \mathbf{g}) \quad (5.31)$$

where γ_g is the unit weight of the pore gas, \mathbf{k}_g is the intrinsic gas conductivity matrix, and k_{rg} is the relative gas conductivity coefficient.

The state equation for the compressible phases ($\pi = w, g$), under isothermal conditions, leads to the constitutive law for compressibility based on the material time derivative with respect to the solid skeleton as

$$\frac{D^s \rho^\pi}{Dt} = \frac{\rho^\pi}{K_\pi} \frac{D^s p_\pi}{Dt} \quad (5.32)$$

where K_w and K_g are the bulk modulus of the water and gas, respectively. The material time derivative of the water saturation with respect to the solid skeleton can be expressed as

$$\frac{D^s S_w}{Dt} = \frac{\partial S_w}{\partial s} \frac{D^s s}{Dt} = \frac{\partial S_w}{\partial s} \left(\frac{D^s p_g}{Dt} - \frac{D^s p_w}{Dt} \right) \quad (5.33)$$

where $\partial S_w / \partial s$ is the specific moisture capacity defined by the soil–water characteristic curve (SWCC), which represents the relationship between suction and relative permeability as a function of the degree of water saturation. In literature, there are various empirical formulations for the SWCC. One popular model proposed by [Van Genuchten \(1980\)](#) is used here, which is given as

$$S_e = \left(1 + \left(\frac{s}{p_0} \right)^n \right)^{-m} \quad (5.34)$$

where S_e denotes the effective or normalized water saturation, p_0 is the air entry pressure defining the suction or capillary pressure at which air starts to flow into the pore

volume, and n and m are material parameters which are determined by curve fitting against experimental data. The effective degree of water saturation S_e is defined as

$$S_e = \frac{S_w - S_{min}}{S_{max} - S_{min}} \quad (5.35)$$

where S_{min} is the minimum or residual degree of water saturation and S_{max} is the maximum degree of water saturation. In the van Genuchten model, the relative permeability coefficients of water and air are expressed as

$$\begin{aligned} k_{rw} &= \sqrt{S_e} \left[1 - (1 - S_e^{1/m})^m \right]^2 \\ k_{rg} &= \sqrt{S_e} \left[1 - S_e^{1/m} \right]^{2m} \end{aligned} \quad (5.36)$$

In order to avoid numerical instability when the model switches from the fully saturated to the partially saturated condition, or from the partially saturated to the dry condition, a lower limit for the relative permeability coefficients of the fluids equal to 0.0001 is assumed. However, for the relative permeability coefficient of electro-osmosis in unsaturated conditions, only a few tests have been reported. Based on the laboratory data in literature, [Tamagnini et al. \(2010\)](#) suggest that the relative permeability coefficient of electro-osmosis can be given as a function of the degree of saturation as

$$k_{reo} = aS_w^b \quad (5.37)$$

where a and b are material parameters.

Finally, by introducing suitable constitutive equations Eqs. (5.30), (5.32) and (5.33), and neglecting the gradients of the water and gas densities, the continuity equation for pore water, Eq. (5.28), with respect to the current configuration of the solid skeleton, can be obtained as

$$\left(\frac{nS_w}{K_w} - n \frac{\partial S_w}{\partial s} \right) \frac{\partial p_w}{\partial t} + n \frac{\partial S_w}{\partial s} \frac{\partial p_g}{\partial t} + S_w \nabla \cdot \mathbf{v}^s + \nabla \cdot \left(\frac{\mathbf{k}_w k_{rw}}{\gamma_w} (-\nabla p_w + \rho^w \mathbf{g}) - \mathbf{k}_{eo} k_{reo} \nabla V \right) = 0 \quad (5.38)$$

Similarly, by considering $D^s S_g / Dt = -D^s S_w / Dt$ and substituting Eqs. (5.31), (5.32) and (5.33) into the mass balance equation of the pore gas, Eq. (5.29), and by neglecting the gradients of the water and gas densities, the continuity equation for the pore air with respect to the current configuration of the solid skeleton can be written as

$$\left(\frac{n(1-S_w)}{K_g} - n \frac{\partial S_w}{\partial s} \right) \frac{\partial p_g}{\partial t} + n \frac{\partial S_w}{\partial s} \frac{\partial p_w}{\partial t} + (1-S_w) \nabla \cdot \mathbf{v}^s + \nabla \cdot \left(\frac{\mathbf{k}_g k_{rg}}{\gamma_g} (-\nabla p_g + \rho^g \mathbf{g}) \right) = 0 \quad (5.39)$$

5.2.6. ELECTRIC CURRENT DENSITY BALANCE EQUATION

According to Ohm's law, the electrical current flow can be expressed by

$$\mathbf{j} = -k_{\sigma e} \nabla V \quad (5.40)$$

where $k_{\sigma e}$ is the electrical conductivity of the soil. The electrical conductivity is a function of the soil mineralogy and pore fluid composition. However, it is evident from experiments that the electrical conductivity of the pore water is greater than that of the

bulk soil. The effective electrical conductivity of an unsaturated porous medium can be represented by

$$k_{\sigma e} = k_{r\sigma e} k_{\sigma w} + k_{\sigma s} \quad (5.41)$$

where $k_{\sigma s}$ is the electric conductivity of the solid skeleton, $k_{\sigma w}$ is the electric conductivity of the pore water under saturated conditions, and $k_{r\sigma e}$ is the relative electric conductivity. It is related to the degree of water saturation and can be described by the power law

$$k_{r\sigma e} = c S_w^d \quad (5.42)$$

where c and d are material parameters.

By applying the conservation of charge and assuming the current is steady state, the governing equation for the electric field can be represented as

$$-\nabla \cdot \mathbf{j} = C_p \frac{\partial V}{\partial t} \quad (5.43)$$

where C_p is the the capacitance per unit volume, and $C_p = 0$ is assumed. Substituting Eq. (5.40) into Eq. (5.43) gives the electric current density balance equation,

$$\nabla \cdot (\mathbf{k}_{\sigma e} \nabla V) = 0 \quad (5.44)$$

5.2.7. FINAL GOVERNING EQUATIONS

The primary variables, namely the displacements, pore water pressure, pore gas pressure and electrical potential, are coupled through the governing equations at large strain for mechanical equilibrium, mass balance of the pore fluids (water and gas) and electric current density, i.e. Eqs. (5.18), (5.38), (5.39) and (5.44), respectively. The governing equations may be solved by the finite element method, and the discretizations in space and time are presented in the following section.

5.3. FINITE ELEMENT FORMULATION

5.3.1. WEAK FORMS

The discretization process for the coupled multiphase flow problem starts by applying the Galerkin weighted residual method to the governing equations. The governing equations are thereby weighted over the domain by the test functions $\delta \mathbf{u}$, δp_w , δp_g and δV , corresponding to the virtual displacements, virtual water pressure, virtual gas pressure and virtual electric potential, respectively.

In an updated Lagrangian (UL) formulation, the virtual work equation for a deformable body of volume V^t at the current configuration, bounded by surface S^t , is written as (Bathe, 1996):

$$\int_{V^t} \mathbf{S}^{t+\Delta t} \cdot \delta \mathbf{E}^{t+\Delta t} dV^t = \int_{V^t} \mathbf{b}^{t+\Delta t} \cdot \delta \mathbf{u}^{t+\Delta t} dV^t + \int_{S^t} \mathbf{t}^{t+\Delta t} \cdot \delta \mathbf{u}^{t+\Delta t} dS^t \quad (5.45)$$

where \mathbf{S} is the PK2 stress tensor, \mathbf{b} is the body force and \mathbf{t} are the boundary traction components. Moreover, the incremental decomposition of the PK2 stress tensor can be expressed as

$$\mathbf{S}^{t+\Delta t} = \mathbf{S}^t + \Delta \mathbf{S} \quad (5.46)$$

when referenced to the current configuration at time t , and assuming $\mathbf{S}_t = \boldsymbol{\sigma}_t$ in the UL formulation. By substituting Eqs. (5.46) into Eq. (5.45), and ignoring the high order terms, the linearized governing equation for equilibrium is obtained as

$$\begin{aligned} \int_{V^t} \bar{\mathbf{D}} \cdot d\boldsymbol{\varepsilon} \cdot \delta\boldsymbol{\varepsilon} dV^t + \int_{V^t} \boldsymbol{\sigma}^t \cdot \delta\boldsymbol{\eta} dV^t &= \int_{V^t} \mathbf{b}^{t+\Delta t} \cdot \delta\mathbf{u} dV^t \\ + \int_{S^t} \mathbf{t}^{t+\Delta t} \cdot \delta\mathbf{u} dS^t - \int_{V^t} \boldsymbol{\sigma}^t \cdot \delta\boldsymbol{\varepsilon} dV^t \end{aligned} \quad (5.47)$$

where $\bar{\mathbf{D}}$ is the stress–strain matrix derived from the constitutive relationship $d\mathbf{S} = \bar{\mathbf{D}} \cdot d\mathbf{E}$ (Nazem et al., 2006). $\boldsymbol{\varepsilon} = -\frac{1}{2}(\nabla\mathbf{u} + (\nabla\mathbf{u})^T)$ and $\boldsymbol{\eta} = -\frac{1}{2}((\nabla\mathbf{u})^T \cdot \nabla\mathbf{u})$ are the linear and nonlinear parts of the Green strain tensor, respectively. Introducing the Jaumann stress rate (Eq. (5.23)) into the virtual work equation, the following equilibrium equation at the current configuration can be obtained:

$$\begin{aligned} \int_{V^t} \mathbf{D}_{ep} \cdot d\boldsymbol{\varepsilon} \cdot \delta\boldsymbol{\varepsilon} dV^t + \int_{V^t} \mathbf{W}_{ep} ds \cdot \delta\boldsymbol{\varepsilon} dV^t + \int_{V^t} (d\boldsymbol{\Omega} \cdot \boldsymbol{\sigma}^{t'} + \boldsymbol{\sigma}^{t'} \cdot d\boldsymbol{\Omega}^T) \cdot \delta\boldsymbol{\varepsilon} dV^t \\ + \int_{V^t} \mathbf{I} d\bar{p} \delta\boldsymbol{\varepsilon} dV^t + \int_{V^t} \boldsymbol{\sigma}^t \cdot \delta\boldsymbol{\eta} dV^t &= \int_{V^t} \mathbf{b}^{t+\Delta t} \cdot \delta\mathbf{u} dV^t \\ + \int_{S^t} \mathbf{t}^{t+\Delta t} \cdot \delta\mathbf{u} dS^t - \int_{V^t} \boldsymbol{\sigma}^t \cdot \delta\boldsymbol{\varepsilon} dV^t \end{aligned} \quad (5.48)$$

The method of weighted residuals provides the weak form of the continuity equation for water flow, Eq. (5.38), as

$$\begin{aligned} \int_V \left(\frac{nS_w}{K_w} - n \frac{\partial S_w}{\partial s} \right) \frac{\partial p_w}{\partial t} \delta p_w dV + \int_V n \frac{\partial S_w}{\partial s} \frac{\partial p_g}{\partial t} \delta p_w dV + \int_V S_w \nabla \cdot \mathbf{v}^s \delta p_w dV \\ + \int_V \nabla \cdot \left(\frac{\mathbf{k}_w k_{rw}}{\gamma_w} (-\nabla p_w + \rho^w \mathbf{g}) - \mathbf{k}_{eo} k_{reo} \nabla V \right) \delta p_w dV = 0 \end{aligned} \quad (5.49)$$

In order to eliminate second order derivatives, partial differentiation and Green's theorem are used here, so that, with suitable boundary conditions, Eq. (5.49) can be rewritten as

$$\begin{aligned} \int_V \left(\frac{nS_w}{K_w} - n \frac{\partial S_w}{\partial s} \right) \frac{\partial p_w}{\partial t} \delta p_w dV + \int_V n \frac{\partial S_w}{\partial s} \frac{\partial p_g}{\partial t} \delta p_w dV + \int_V S_w \nabla \cdot \mathbf{v}^s \delta p_w dV \\ + \int_V \left(\frac{\mathbf{k}_w k_{rw}}{\gamma_w} (\nabla p_w - \rho^w \mathbf{g}) + \mathbf{k}_{eo} k_{reo} \nabla V \right) \cdot \nabla (\delta p_w) dV = 0 \end{aligned} \quad (5.50)$$

Similarly, the weak form of the continuity equation for gas flow (Eq. (5.39)) is obtained

as

$$\begin{aligned} & \int_V \left(\frac{n(1-S_w)}{K_g} - n \frac{\partial S_w}{\partial s} \right) \frac{\partial p_g}{\partial t} \delta p_g dV + \int_V n \frac{\partial S_w}{\partial s} \frac{\partial p_w}{\partial t} \delta p_g dV + \int_V (1-S_w) \nabla \cdot \mathbf{v}^s \delta p_g dV \\ & + \int_V \nabla \cdot \left(\frac{\mathbf{k}_g k_{rg}}{\gamma_g} (-\nabla p_g + \rho^g \mathbf{g}) \right) \delta p_g dV = 0 \end{aligned} \quad (5.51)$$

The weak form of the mass balance equation for pore gas flow is obtained in the current configuration as

$$\begin{aligned} & \int_V \left(\frac{n(1-S_w)}{K_g} - n \frac{\partial S_w}{\partial s} \right) \frac{\partial p_g}{\partial t} \delta p_g dV + \int_V n \frac{\partial S_w}{\partial s} \frac{\partial p_w}{\partial t} \delta p_g dV + \int_V (1-S_w) \nabla \cdot \mathbf{v}^s \delta p_g dV \\ & + \int_V \left(\frac{\mathbf{k}_g k_{rg}}{\gamma_w} (\nabla p_g - \rho^g \mathbf{g}) \right) \cdot \nabla (\delta p_g) dV = 0 \end{aligned} \quad (5.52)$$

Finally, the weak form of the continuity equation for electric current density, Eq. (5.44), is obtained as

$$\int_V (\nabla \cdot (\mathbf{k}_{\sigma e} \nabla V)) \delta V dV = 0 \quad (5.53)$$

The weak form of the electric current density balance is obtained in the current configuration as

$$\int_V (\mathbf{k}_{\sigma e} \nabla V) \cdot \nabla (\delta V) dV = 0 \quad (5.54)$$

5.3.2. SPATIAL AND TIME DISCRETIZATION

The finite element method (Lewis and Schrefler, 1998; Smith and Griffiths, 2004) has been used to solve the coupled system of weak form equations, Eqs. (5.48), (5.50), (5.52) and (5.54). The following system matrix equations can be derived:

$$\mathbf{C}\dot{\mathbf{X}} + \mathbf{K}\mathbf{X} = \dot{\mathbf{W}}^{ext} \quad (5.55)$$

where

$$\mathbf{C} = \begin{bmatrix} \mathbf{K}_{nl} & \mathbf{C}_{sw} & \mathbf{C}_{sg} & \mathbf{0} \\ \mathbf{C}_{ws} & \mathbf{C}_{ww} & \mathbf{C}_{wg} & \mathbf{0} \\ \mathbf{C}_{gs} & \mathbf{C}_{wg}^T & \mathbf{C}_{gg} & \mathbf{0} \\ \mathbf{0} & \mathbf{0} & \mathbf{0} & \mathbf{K}_{\sigma e} \end{bmatrix}, \quad \mathbf{K} = \begin{bmatrix} \mathbf{0} & \mathbf{0} & \mathbf{0} & \mathbf{0} \\ \mathbf{0} & \mathbf{K}_{ww} & \mathbf{0} & \mathbf{K}_{eo} \\ \mathbf{0} & \mathbf{0} & \mathbf{K}_{gg} & \mathbf{0} \\ \mathbf{0} & \mathbf{0} & \mathbf{0} & \mathbf{0} \end{bmatrix}, \quad \mathbf{X} = \begin{Bmatrix} \mathbf{u} \\ \mathbf{p}_w \\ \mathbf{p}_g \\ \mathbf{V} \end{Bmatrix}$$

$$\dot{\mathbf{X}} = \begin{Bmatrix} \dot{\mathbf{u}} \\ \dot{\mathbf{p}}_w \\ \dot{\mathbf{p}}_g \\ \dot{\mathbf{V}} \end{Bmatrix}, \quad \dot{\mathbf{W}}^{ext} = \begin{Bmatrix} \dot{\mathbf{F}}^{ext} \\ \mathbf{Q}_w^{ext} \\ \mathbf{Q}_g^{ext} \\ \mathbf{Q}_V^{ext} \end{Bmatrix}$$

and where the definitions of the coefficient matrices and the load and flow vectors are given in Appendix B. The time integration and Newton–Raphson method, presented in Section 3.3 of Chapter 3, is used here to solve the coupled governing equation system.

5.4. VALIDATION AND NUMERICAL SIMULATIONS

In this section, numerical examples are presented to demonstrate the capability of the proposed large strain model to accurately simulate a coupled multiphase, electro-osmosis problem. The model was first validated with respect to a 1D analytical solution for the electro-osmosis consolidation of a saturated soil under small strain conditions, which has already been presented in Chapter 3. Currently, there are no analytical solutions for solving the unsaturated flow problem. Thus, the model is then verified by comparing computational results with experimental data from a sand column desaturation test conducted by Liakopoulos (1964). This is followed by 1D and 2D examples that highlight the importance of considering the elasto-plastic mechanical behaviour of unsaturated clays in electro-osmosis consolidation. Furthermore, these examples also emphasize the significance of the multiphase formulation in simulating the electro-osmosis consolidation of unsaturated clays.

In all examples, an eight-node quadratic finite element is adopted for displacements, and this is coupled to a four node quadrilateral element for modelling pore water pressure, pore air pressure and electrical potential.

5

5.4.1. VALIDATION OF THE NUMERICAL MODEL

Two 1D numerical examples have been used in the validation. The first considers electro-osmosis consolidation for electro-osmosis and hydraulic coupling under saturated conditions (Esrig's (1968) problem), to illustrate the accuracy of the proposed model in modelling electro-osmosis, as seen in Figure 3.1. This is the same example as discussed in Section 3.4.1 of Chapter 3, so it is not repeated here. The second example describes the desaturation of a sand column under the effect of gravity. The simulation results are compared with those presented in literature, to demonstrate the accuracy of the proposed model in simulating three phase flow during unsaturated consolidations.

No analytical solution exists for the problem of multiphase flow in a partially saturated soil. Therefore, the three phase flow model has been validated by re-analysing a laboratory test (Liakopoulos, 1964) that has been used as a benchmark for partially saturated soil models by previous researchers (Lewis and Schrefler, 1998; Schrefler and Zhan, 1993; Schrefler and Scotta, 2001; Laloui et al., 2003). A sand column, of 1 m height, is considered to be initially fully saturated, but is left to slowly dewater from its base due to gravity. The column is divided into 20 elements with a size of 0.1×0.05 m. The boundary conditions are as follows: the air pressure at the top and base of the column, and the water pressure at the base are equal to zero (atmospheric pressure); the side walls are impermeable to water and gas; the bottom boundary is fixed with respect to displacement, whereas the lateral boundaries are restrained only in the horizontal direction. The material properties of the sand used in the test are summarized in Table 5.1. In order to describe unsaturated flow, the following saturation–capillary pressure and relative permeability–saturation relationships are adopted (Lewis and Schrefler, 1998):

$$\begin{aligned} S_w &= 1.0 - 1.9722 \times 10^{-11} s^{2.4279} \\ k_{rw} &= 1.0 - 2.207(1.0 - S_w)^{1.0121} \end{aligned} \quad (5.56)$$

In addition, the relative permeability of the pore gas saturation relationship is assumed

to be

$$k_{rg} = (1.0 - S_e)^2 (1.0 - S_e^{5/3})$$

$$S_e = \frac{S_w - S_{rw}}{1.0 - S_{rw}} \quad (5.57)$$

where the residual water saturation is $S_{rw} = 0.2$ and S_e is the effective water saturation.

Table 5.1: Material properties for the analysis of Liakopoulous's (1964) test

Young's Modulus	E	1.3 MPa
Poisson's ratio	ν	0.4
Porosity	n	0.2975
Solid grain density	ρ_s	2000 kg/m ³
Water density	ρ_w	1000 kg/m ³
Air density	ρ_g	1.2 kg/m ³
Bulk modulus of water	K_w	2×10^9 Pa
Bulk modulus of air	K_g	0.1×10^6 Pa
Intrinsic permeability	k	4.5×10^{-12} m/s
Dynamic viscosity of water	μ_w	1×10^{-3} Pa·s
Dynamic viscosity of air	μ_g	1.8×10^{-5} Pa·s
Gravitational acceleration	g	9.806 m/s ²
Atmosphere pressure	p_{atm}	0 Pa

Figure 5.1 ((a)-(e)) shows the numerical results of the three phase model for the water pressure, gas pressure, capillary pressure and water saturation, as a function of height and time. The curves are plotted at 10, 30, 60 and 120 minutes. The water flows out of the column through the bottom boundary due to gravity; when a negative pore water pressure equal to the original weight of the water has been established at the top of the column, the water flow stops as indicated in Figure 5.1(a). Figure 5.1(b) shows that gas is sucked into the column due to the water outflow, resulting in a negative pore gas pressure which reaches a maximum at around 30 minutes, after which it starts to decrease. The development of capillary pressures (i.e. suction) spreads from the top to the bottom of the column, as shown in Figure 5.1(c), and, after 120 minutes, the water saturation has reduced to 0.91 at the top of the column (Figure 5.1(d)). The surface settlement after 120 minutes is approximately 0.0016 m, as shown in Figure 5.1 (e). Figure 5.1(f) shows the water outflow rate as a function of time. There is excellent agreement between the numerical results of the proposed approach and those from previous numerical research (Lewis and Schrefler, 1998). The numerical results predict a much lower water flow rate than the measurements, due to the impermeable gas boundary condition being applied on the lateral surface; however, they can be improved by considering a permeable gas boundary condition (Hu et al., 2011). Overall, the presented computational results agree with the literature (Lewis and Schrefler, 1998; Schrefler and Zhan, 1993; Schrefler and Scotta, 2001; Laloui et al., 2003).

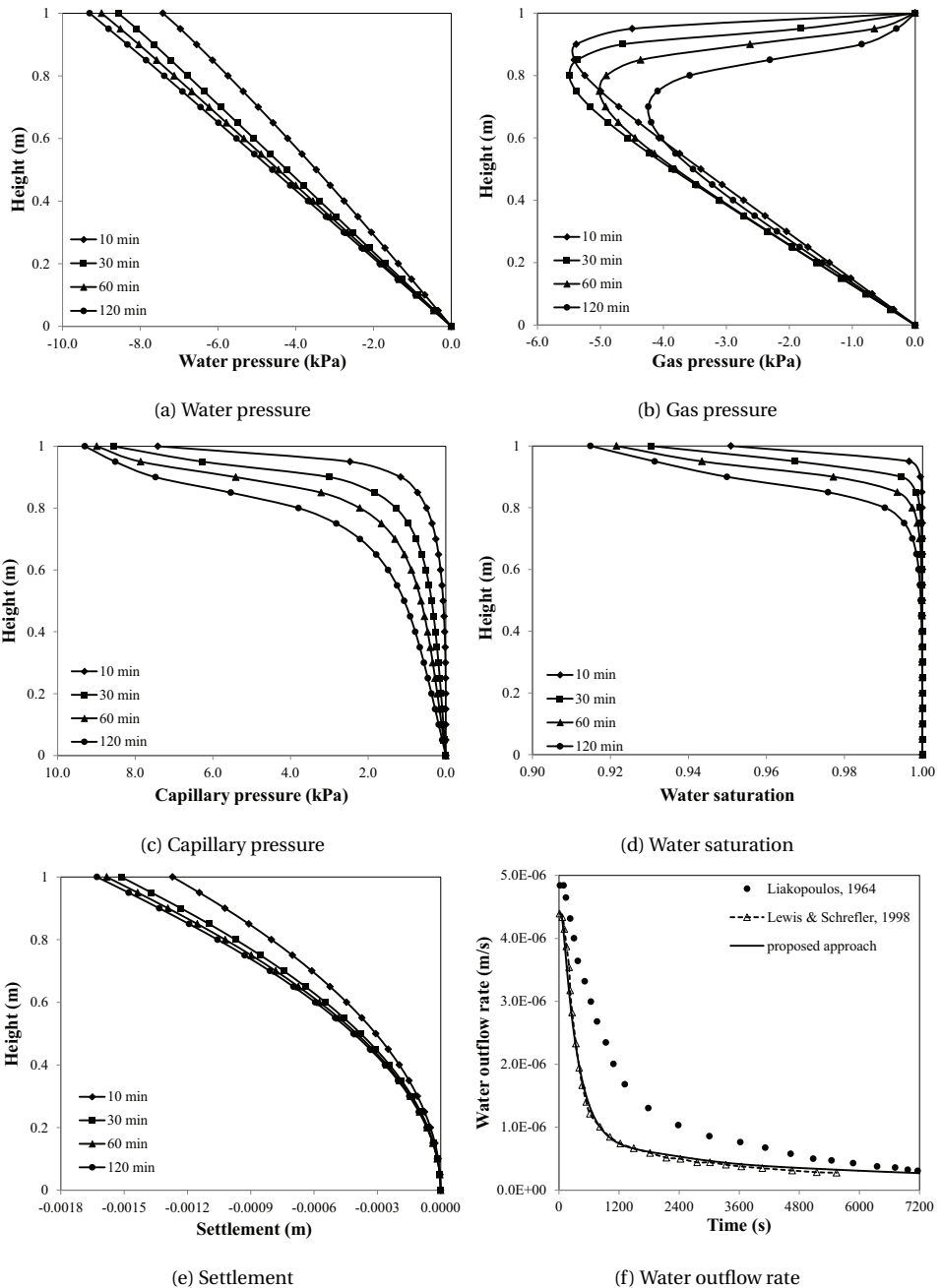


Figure 5.1: Numerical results of Liakopoulos's sand column test

5.4.2. NUMERICAL EXAMPLES AND PARAMETRIC STUDY

Two further examples are discussed. The first studies the 1D elastic consolidation of a partially saturated clay due to an electrical potential applied at the top boundary. The differences between two-phase and three-phase analyses of coupled electro-osmosis consolidation are highlighted, and the effect of different parameters on the electro-osmosis response are also investigated. The second example studies the elasto-plastic behaviour of a 2D plane strain model. In this example, the behaviour of clay during electro-osmosis consolidation is examined, using the fully coupled multiphase approach with the unsaturated elasto-plastic BBM constitutive relationship to capture the nonlinear stress-strain behaviour of the clay. Note that the flow due to gravity is neglected in the following two examples, since the problem size is small in each case.

1D ELASTIC UNSATURATED ELECTRO-OSMOSIS CONSOLIDATION

In order to study the time dependent behaviour of unsaturated soft clay during electro-osmosis consolidation, as well as to consider the difference between small and large strain models, and the effect of including gas generation and gas transport, the 1D FE model from Section 3.4 is subjected to an electrical potential of 10 V at the bottom boundary. The domain is divided into 20 elements with a size of 0.1×0.05 m. The displacement and other boundary conditions are the same as for the problem illustrated in Figure 3.1, and an initial state of mechanical equilibrium is assumed for the initial displacement. An initial back pressure of 400 kPa is assumed in the entire sample, to avoid cavitation when the pore water pressures become negative due to electro-osmosis. The pore gas pressure is also assumed to be initially 400 kPa and the pore gas boundary conditions are as follows: the cathode is open for gas flow; at the anode, the production of gas arising from the electrolysis of water is simulated by relating the inward gas flow to the instantaneous electric current density (Tamagnini et al., 2010), i.e.

$$q_g = J \frac{RT}{4Fp_g} \eta \quad (5.58)$$

where q_g is the gas inflow, J is the applied electric density, R is the universal gas constant, T is the absolute temperature, F is Faraday's constant, and η is the efficiency parameter that is introduced to account for possible losses at the electrode due to chemical reactions. In this numerical example, in order to study the effect of gas generation, numerical simulations are performed assuming saturated conditions, or unsaturated conditions induced by gas generation at the anode, assuming an efficiency $\eta = 0.1$. To study the effect of gas generation efficiency, different values of $\eta = 0.0, 0.1, 0.2$ and 0.4 are also considered and discussed in the second part of the numerical example. The following material parameters are assumed: Young's modulus $E = 7.4 \times 10^5$ Pa, Poisson's ratio $\nu = 0.3$, electro-osmosis permeability $k_{eo} = 5.0 \times 10^{-9}$ m²/V·s, electric conductivity $k_{\sigma e} = 0.1$ S/m, hydraulic conductivity $k_w = 2.0 \times 10^{-9}$ m/s and pore gas permeability $k_g = 1.33 \times 10^{-10}$ m/s. Moreover, for the dependence of the relevant parameters on the degree

of saturation, the suggestions given by Tamagnini et al. (2010) have been followed, i.e.

$$\begin{aligned}
 S_w &= (1 + (\alpha s)^n)^{-m} \\
 k_{rw} &= a_w (S_w)^{b_w} \\
 k_{rg} &= a_g (S_g)^{b_g} \\
 k_{reo} &= a_{eo} (S_w)^{b_{eo}} \\
 k_{\sigma e} &= a_e (S_w)^{b_e}
 \end{aligned} \tag{5.59}$$

in which $n = 1.31$, $m = 11/n$, $\alpha = 0.00851 \text{ kPa}^{-1}$, $a_w = 1$, $b_w = 5$, $a_g = 1$, $b_g = 5$, $a_{eo} = 1$, $b_{eo} = 3.2$, $a_e = 1$ and $b_e = 2$, are material constants.

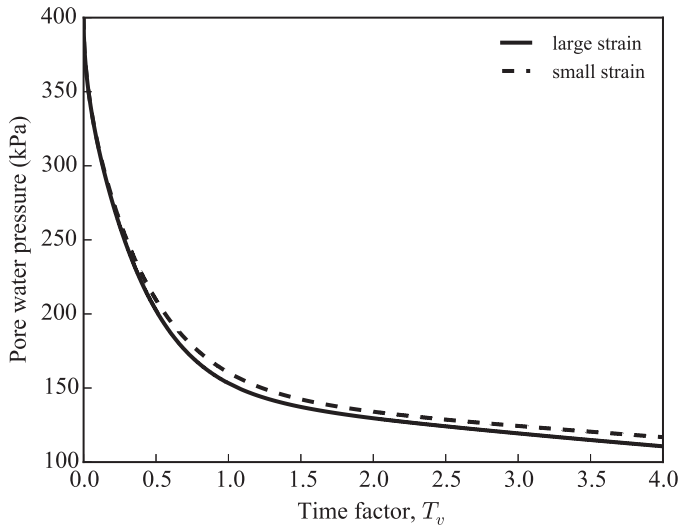


Figure 5.2: Pore water pressure at anode versus time factor for 1D electro-osmosis.

By considering the gas generation efficiency parameter to be $\eta = 0.1$, the evolution of the pore water pressure and the settlements for large and small strain models are presented. Figure 5.2 shows the pore water pressure at the anode versus time factor, defined by $T_v = k_w \cdot t / (\gamma_w \cdot m_v \cdot L^2)$, in which m_v is the coefficient of compressibility and L is the drainage path length. It is seen that the pore water pressure drop develops faster at the anode for the large strain analysis than for the small strain analysis, because of the strain dependent stiffness and the geometry change accounted for in the large strain analysis that makes the electrical gradient greater and the drainage path length shorter than in the small strain analysis (in which the geometry is constant). Figure 5.3 shows the time dependent behaviour of the surface settlement for the small and large strain models. As expected, the small strain model predicts a larger final absolute settlement than the large strain model, due to the consideration of geometrical changes in the latter.

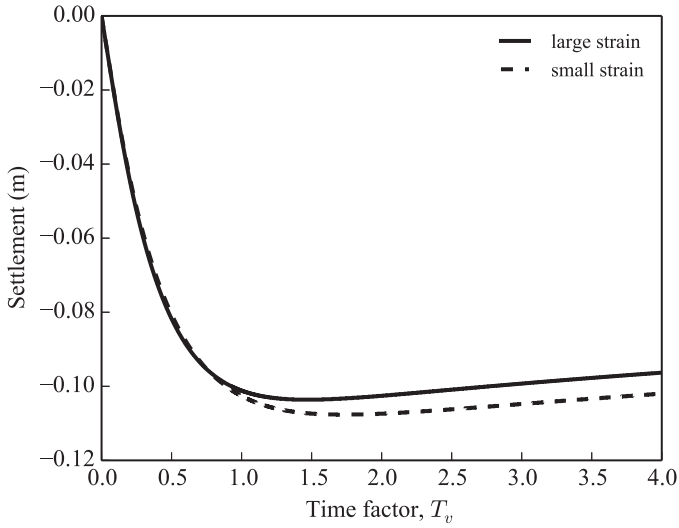


Figure 5.3: Surface settlement versus time factor for 1D electro-osmosis.

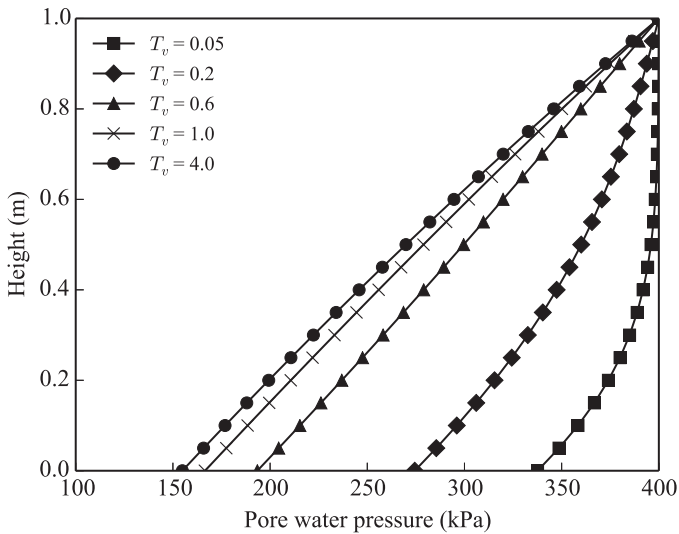


Figure 5.4: Pore water pressure versus depth for various time factors under saturated conditions (no gas generation).

The pore water pressure distributions with depth for saturated and unsaturated conditions ($\eta=0.1$), at various times, are presented in Figures 5.4 and 5.5, respectively. It

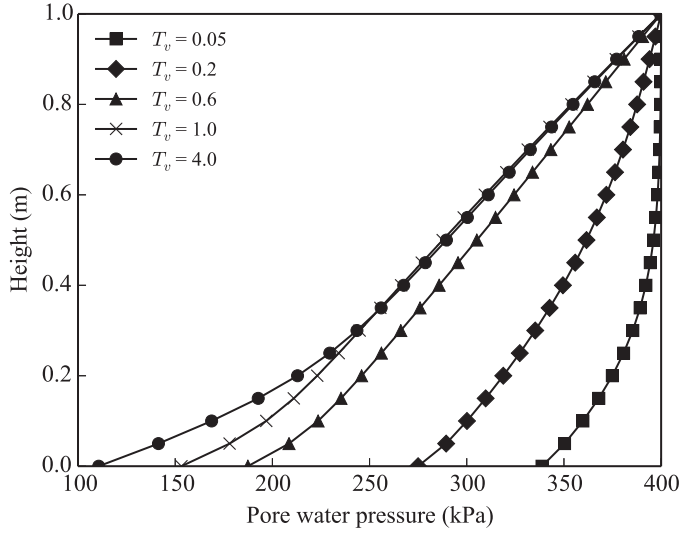


Figure 5.5: Pore water pressure versus depth for various time factors in unsaturated conditions.

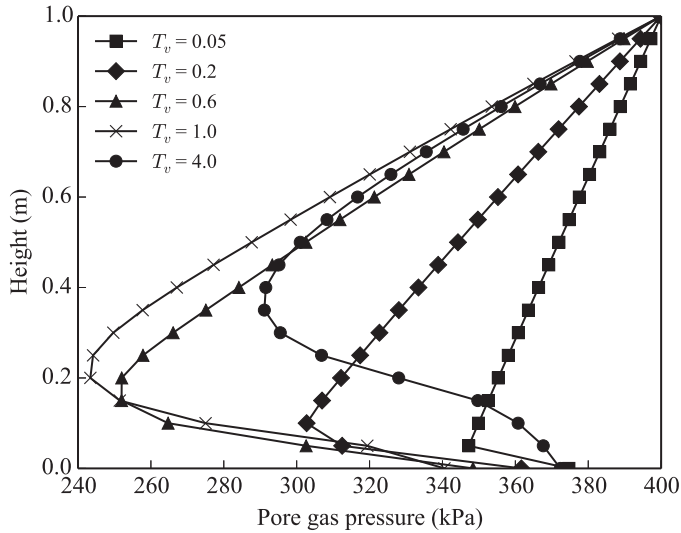


Figure 5.6: Pore gas pressure versus depth for various time factors in unsaturated conditions.

can be seen that, near the start of the analysis ($T_v = 0.05$ and $T_v = 0.2$), both saturated and unsaturated analyses predict almost the same pore water pressure profiles, but, as the gas produced by hydrolysis accumulates and the pore water pressure decreases near

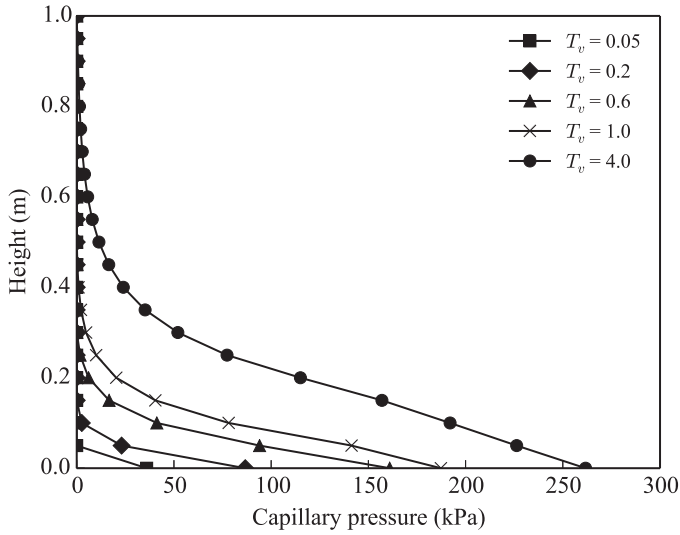


Figure 5.7: Capillary pressure versus depth for various time factors.

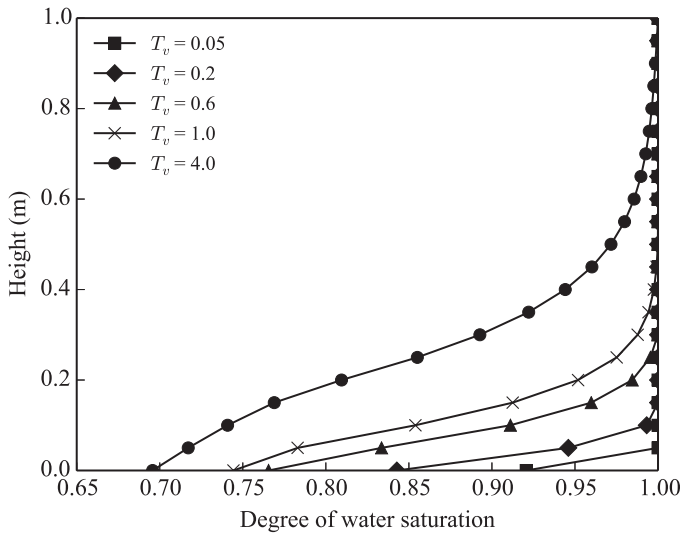


Figure 5.8: Degree of water saturation versus depth for various time factors.

the anode, the region around the anode becomes increasingly unsaturated, and significant additional pore water pressure decreases near the anode are predicted compared to the saturated case ($T_v = 0.6$, $T_v = 1.0$ and $T_v = 4.0$). Theoretically, the magnitude

of the pore water pressure developed by electro-osmosis is governed by the ratio of the electro-osmosis permeability and hydraulic conductivity of the soil (k_{eo}/k_w), it being greater for larger values of k_{eo}/k_w . Under unsaturated conditions, the transport coefficients involved in electro-osmosis consolidation are strongly influenced by the degree of water saturation. As can be seen in Eq. (5.59), the decrease of hydraulic conductivity is much faster than the decrease of electro-osmosis permeability, so that the ratio k_{eo}/k_w increases with a decrease in the degree of water saturation. Hence, a larger decrease in pore water pressure is predicted when there is sample desaturation near the anode. Beyond the anode region, in Figure 5.5, a smaller decrease in pore water pressure is found ($T_v = 0.6$, $T_v = 1.0$ and $T_v = 4.0$) compared to the saturated case (Figure 5.4), due to the pore water pressure decrease being hindered by the pore gas pressure in this area.

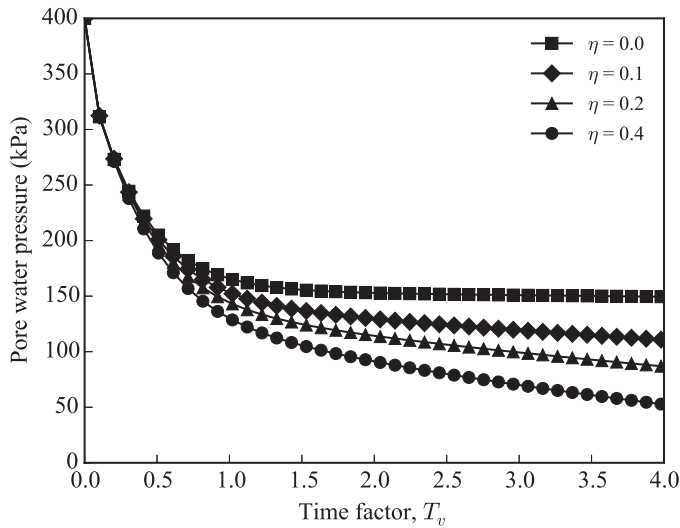


Figure 5.9: Pore water pressure at anode versus time factor for different gas generation efficiency parameters.

The distributions of the pore gas pressure versus depth for various times are shown in Figure 5.6. It is shown that the pore gas pressure in the sample initially decreases with time. The gas produced at the anode flows towards the cathode. However, it cannot escape easily from the sample and accumulates near the anode, making the sample more unsaturated. Figures 5.7 and 5.8 show the numerical results for the capillary pressure and degree of water saturation, respectively, with depth, for various time factors. As seen in the figures, the desaturation process starts at the anode where the gas is generated and spreads to the cathode.

To study the effect of the gas generation efficiency parameter η , a sensitivity analysis has been performed to illustrate the evolution of pore water pressure and pore gas pressure at the anode and surface settlement at the cathode, as shown in Figures 5.9-5.11. It is shown that the pore water pressure drop at the anode becomes greater with the increase of η , as explained previously, since gas generated by the electrolysis of water

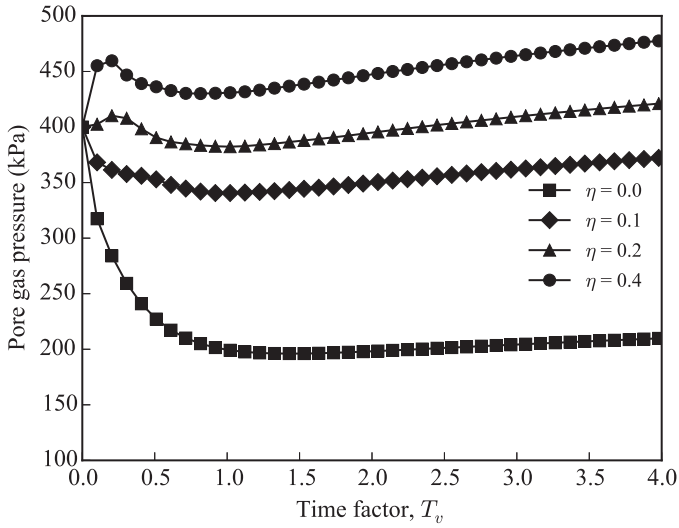


Figure 5.10: Pore gas pressure at anode versus time factor for different gas generation efficiency parameters.

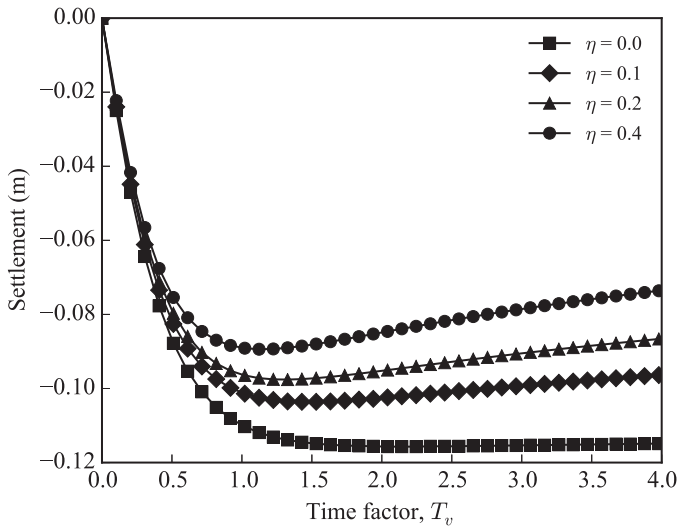


Figure 5.11: Surface settlement versus time factor for different gas generation efficiency parameters.

accumulates in the anode region and makes the sample partially desaturate. The water pressure drop tends to increase as the degree of water saturation decreases. Figure 5.10 shows the pore gas pressure evolution at the anode for different η , demonstrating that

overall the pore gas pressure in the anode region increases significantly as gas production increases. It can be seen that, when the gas production is zero or small ($\eta=0.0, 0.1$) the pore gas pressures at the anode tend to decrease and are lower than the initial back pressure. By increasing the gas production ratio ($\eta=0.2, 0.4$) at the anode, a peak in the pore gas pressure can be observed at the beginning of the simulation, and the final pore gas pressures are higher than the initial back pressure. Figure 5.11 shows that, the higher the amount of gas generated at the anode, the smaller the final surface settlement. This is because partial saturation due to gas generation could make the sample "stiffer" according to the Bishop effective stress. Note that the surface of the soil tends to swell due to the increase of pore gas pressure in the last stage of the simulation.

2D UNSATURATED ELASTO-PLASTIC ELECTRO-OSMOSIS CONSOLIDATION

The square domain previously shown in Figure 4.6, of side length 1 m, is now used to investigate unsaturated elasto-plastic clay behaviour during electro-osmosis consolidation. The domain is divided into 100 square elements of size 0.1×0.1 m. The boundary conditions are as follows: the left edge is impermeable to both water and gas, and is on rollers allowing only vertical movement; the right edge is free for both water and gas and it is also on rollers allowing only vertical movement; the bottom boundary is impermeable to both water and gas, and is fixed with respect to displacements; the top surface is free for both water and gas. In terms of electric boundary conditions: the anode is along the left edge, the right edge is the cathode, and the horizontal boundaries are impermeable to electric current. An electric potential of 20 V is applied at the anode, and the efficiency parameter is assumed to be $\eta = 0.1$. An initial back pressure of 600 kPa is assumed for both water and gas, in order to avoid cavitation issues.

Table 5.2: Material properties used for 2D analysis (after Sheng et al. (2003b))

MCC parameters		BBM parameters	
Plastic compression index	$\lambda = 0.25$	Reference stress	$p_r = 1.0 \text{ kPa}$
Elastic compression index	$\kappa = 0.05$	Rate of increase of soil stiffness with suction	$\beta = 0.012 \text{ kPa}^{-1}$
Poisson's ratio	$\nu = 0.3$	Parameter defining maximum soil stiffness	$r = 0.75$
Friction constant	$M = 0.772$	Rate of cohesion increase with suction	$k_s = 0$
Initial void ratio	$e_0 = 3.0$	Elastic compression index of suction	$\kappa = 0$
Over consolidation ratio	$OCR = 1.0$	Degree of non-associativity of the flow rule	$\alpha = 0.376$

The transport parameters are the same as for the previous 1D electro-osmosis example. The Barcelona Basic Model proposed by Alonso et al. (1990), based on the Modified Cam Clay (MCC) model, is employed, although the BBM version considered in this paper neglects the possibility of yielding on the suction increase line. This simplifies treatment with little loss of generality, as, for most applications of the BBM, soil paths never in-

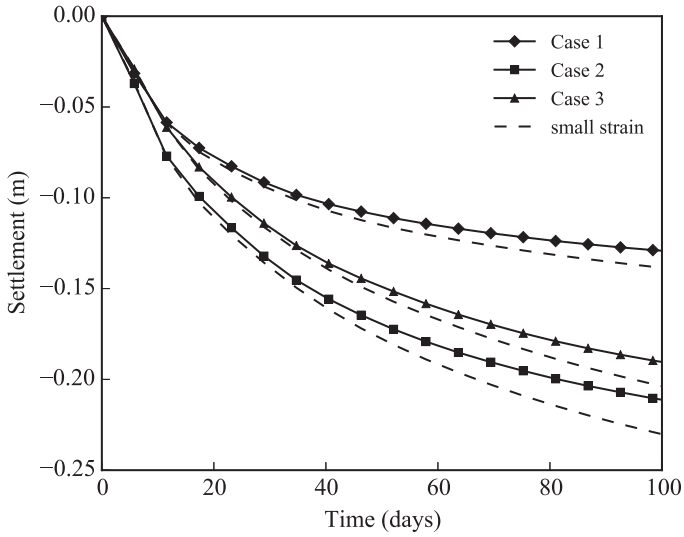


Figure 5.12: Evolution of surface settlement at the anode with time, for large and small strain analyses.

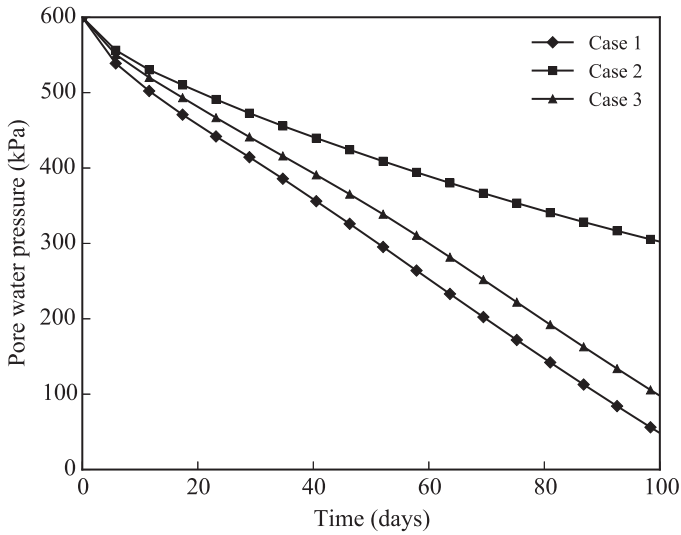


Figure 5.13: Pore water pressure at the base of the anode versus time relationship for different analyses.

tersect the SI locus (Solowski and Gallipoli, 2010). Typical material parameters for the BBM with Bishop's effective stress have been adopted, based on Sheng et al. (2003b), and are listed in Table 5.2. The initial effective stresses have been assigned by using the

Table 5.3: Details of 3 types of analyses used in 2D example

Analysis type	Constitutive model	Gas generation
Case 1	BBM	Yes
Case 2	MCC	No
Case 3	MCC	Yes

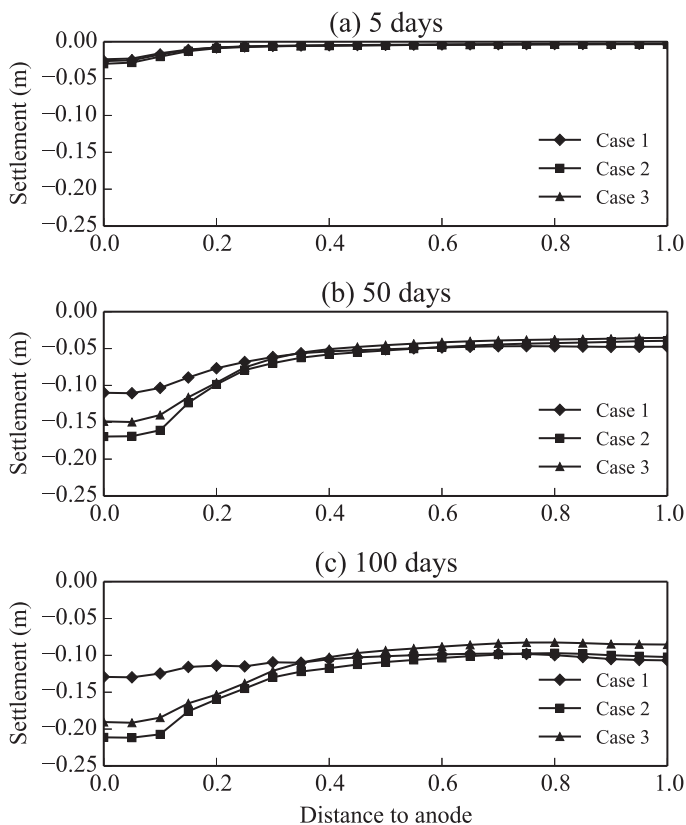


Figure 5.14: Surface settlement relative to the anode at various times for different analyses.

effective unit weight of the soil ($\gamma' = 900 \text{ kN/m}^3$) and the coefficient of earth pressure at rest ($K_0 = 1.0$). However, to avoid potential numerical problems at very low stresses, a minimum vertical effective stress of 1 kPa is assumed. The initial yield surface location is then determined according to the initial effective pressure distribution and assumed over-consolidation ratio (OCR). Finally, the electric potential is applied at the anode, and the displacements and pore water pressure changes due to the consolidation processes

are computed.

In order to study the elasto-plastic mechanical behaviour of the clay and the effect of gas generation at the anode, three groups of analyses are carried out, as indicated in Table 5.3. Case 1 uses the BBM constitutive relationship with gas generation. Case 2 uses the MCC constitutive relationship without gas generation. Case 3 uses the MCC constitutive relationship with gas generation.

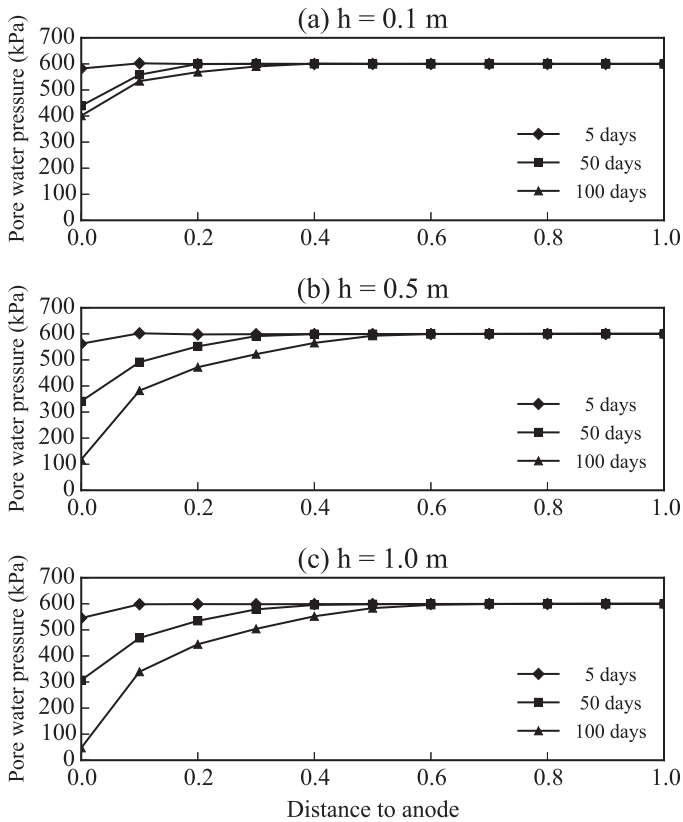


Figure 5.15: Pore water pressure (Case 1) relative to the anode for various times at different depths.

Figure 5.12 illustrates the evolution of settlement at the top of the anode for the different analyses, considering both large and small strain. As expected, the large strain model predicts smaller final settlements for all three Cases, due to the strain dependent geometric stiffness. The difference between large and small strain results is approximately 10%, demonstrating that large strain may often be necessary in the modelling of electro-osmosis consolidation.

Focusing only on the large strain analyses in Figure 5.12, Case 1, which uses the BBM, predicts lower absolute final settlements compared to Case 3, which uses MCC, even though gas generation at the anode is considered in both analyses. This is because the

generated gas at the anode is trapped in the soil mass, making it unsaturated. When the BBM is employed, the suction is considered to be a state variable and the clay becomes stiffer as the suction increases. However, in the MCC analysis the suction is neglected. Although MCC is employed for Cases 2 and 3, gas generation is only considered in Case 3. It is shown that Case 2 predicts larger absolute final settlements compared to Case 3, indicating that the gas generated at the anode hinders the development of surface settlement.

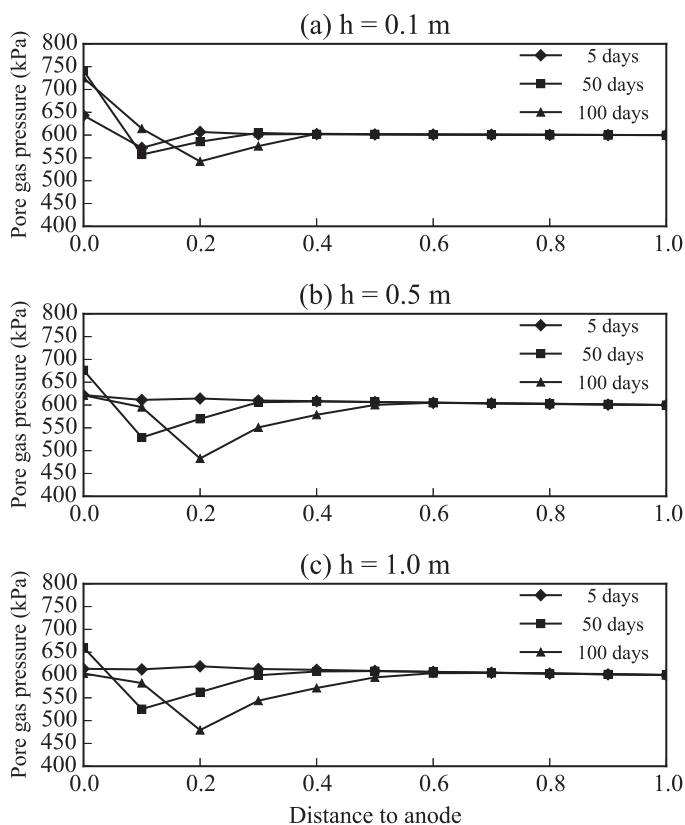


Figure 5.16: Pore gas pressure (Case 1) relative to the anode for various times at different depths.

The pore water pressure versus time relationship at the base of the anode for the three analyses is shown in Figure 5.13. The development of pore water pressure in Case 2 is much smaller than in Cases 1 and 3, due to partial saturation being considered in Cases 1 and 3 (caused by gas developed at the anode). As mentioned in the previous section, the ratio k_{e0}/k_w increases with a decrease in the degree of water saturation. Therefore, as the magnitude of the developed pore water pressure is governed by k_{e0}/k_w , as the clay desaturates, the excess pore water pressure drop at the anode increases.

Figure 5.14 shows the surface settlement as a function of the distance to the anode at

various times for the different analyses. At day 5, the difference between the analyses is small and the vertical settlement is mainly developed near the anode. As time increases, the difference between Case 1 and Cases 2 and 3 becomes larger. Since the BBM is employed in Case 1, when the clay desaturates the soil becomes much stiffer, so that the soil settles less near the anode than in Cases 2 and 3 in which the MCC model is used.

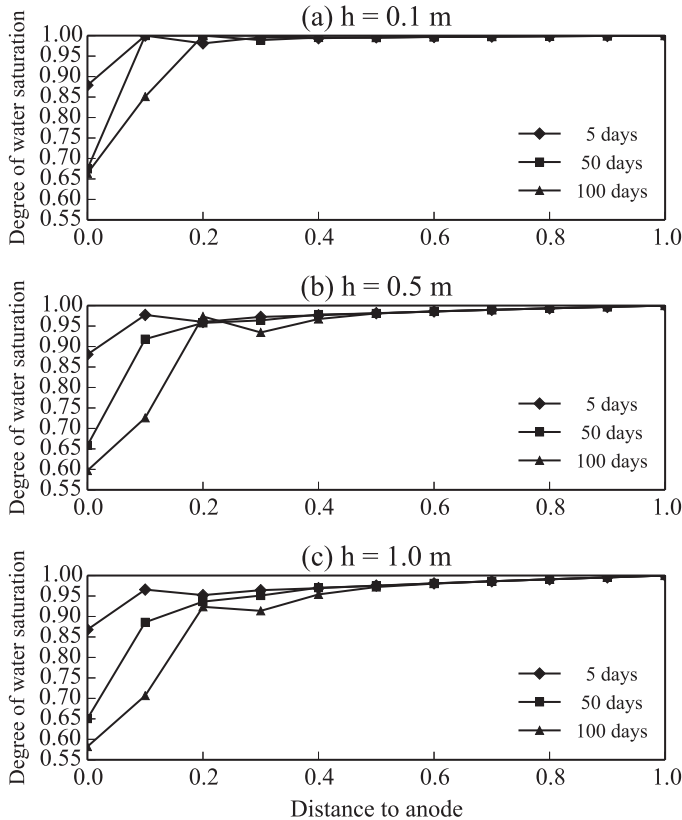


Figure 5.17: Degree of water saturation (Case 1) relative to the anode for various times at different depths.

Special attention is paid to the numerical results of Case 1, in which the BBM constitutive model and gas generation are considered. Figure 5.15 shows the pore water pressure profiles between the electrodes for various times and different depths. As expected, the pore water pressure changes mainly develop near the anode, although the extent of the pore water pressure decrease is increasing with time. Moreover, the middle ($h = 0.5$ m) and bottom ($h = 1.0$ m) of the layer have almost the same pore water pressure profile, and both show larger decreases than the top of the layer ($h = 0.1$ m) due to the drainage condition imposed at the surface. The pore gas pressure profiles between the electrodes for various times and different depths are shown in Figure 5.16. The pore gas pressure should have a similar profile to the pore water pressure if there is no gas generation at

the anode. The pore gas pressure near the anode increases for all three depths, because of the gas production at the anode. There is a drop of pore gas pressure a bit further from the anode region, and this drop of pore gas pressure moves towards cathode with time, due to the gas migrating to the cathode. The degree of water saturation shows similar trends to the pore water pressure. Figure 5.17 shows that the desaturation process starts at the anode and spreads to the cathode. The final degree of water saturation developed at the base of the anode is around 0.6, which indicates that the desaturation near the anode can be significant. The final unsaturated zone has spread 0.8 m from the anode.

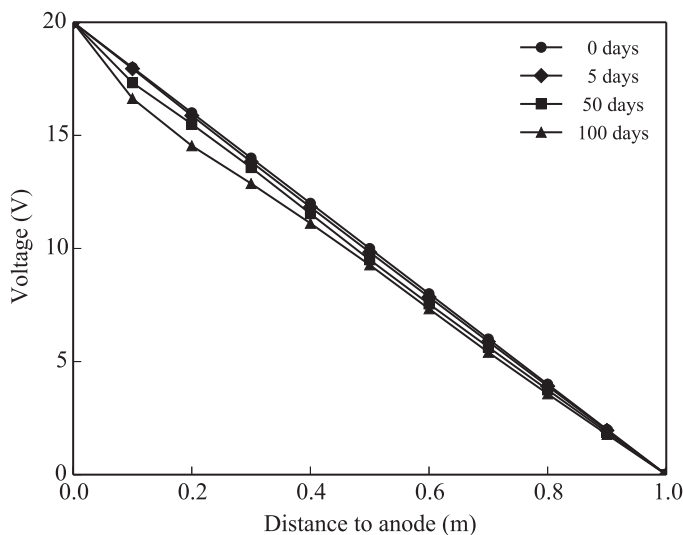


Figure 5.18: Voltage (Case 1) profile along the bottom boundary relative to the anode for various times.

Finally, the voltage profiles along the bottom boundary between the electrodes, for different times, are presented in Figure 5.18. There is an electrical potential drop near the anode with increasing time, which is consistent with the findings of laboratory observations (Mohamedelhassan and Shang, 2001). Due to the flow of water toward the cathode and the gas developed near the anode, the soil mass becomes unsaturated near the anode and remains fully saturated near the cathode. Consequently, the electrical conductivity of the soil is not uniform, but decreases near the anode, resulting in a non-linear electrical potential distribution. The voltage drop at the soil-electrode interface may be more significant, although this is not considered in the model.

5.5. CONCLUSIONS

In this chapter, a formulation for considering large strain elasto-plastic electro-osmosis consolidation under unsaturated conditions has been presented, which simulates the coupling of the water flow, gas flow and electrical transport in the deformable porous medium. Four coupled governing equations are derived and solved using finite ele-

ments. The elasto-plastic behaviour of clay under unsaturated conditions is considered by employing the Barcelona Basic Model (BBM), and degree of water saturation dependent constitutive relationships are employed to describe the nonlinearity of the transport parameters. The novel feature of the proposed numerical model is the possibility to account for, within a single framework, the effects of gas generation, the unsaturated elasto-plastic constitutive relationship and large strain.

In order to demonstrate that the proposed model is effective in modelling partially saturated electro-osmosis consolidation, the fully coupled governing equations have been successfully applied to a series of numerical examples. Two numerical examples have been chosen to illustrate the accuracy of the proposed approach. A 1D example of electro-osmosis consolidation showed good agreement with an analytical solution. In the second example, the experiment conducted by Liakopoulos (1964) has been used as a benchmark problem to further verify the proposed approach in modelling unsaturated flow. Following the verification, a simple elastic 1D numerical simulation has been conducted and evaluated, to highlight the influence of considering large strain and gas generation during elastic electro-osmosis consolidation. A sensitivity analysis has been conducted, to evaluate the influence of the gas generation efficiency. An idealized elasto-plastic 2D electro-osmosis consolidation problem, using the BBM constitutive relationship, has then been investigated.

Under unsaturated conditions, the transport coefficients involved in electro-osmosis consolidation are strongly dependent on the degree of water saturation. Changes in the degree of water saturation result in changes in the coefficients of electro-osmosis permeability and hydraulic conductivity. These should not be neglected, because electro-osmosis consolidation is governed by the ratio of the electro-osmosis permeability to the hydraulic conductivity of the soil. Moreover, the generated gas at the anode could hinder the soil deformation. By considering suction as a state variable in the BBM, it has been shown that the soil becomes significantly stiffer due to desaturation at the anode, resulting in much less settlement in this region, for example, compared to results obtained using the MCC model. The electrical potential distribution between the electrodes has also been investigated, by considering the change in the electrical conductivity with degree of water saturation. It was demonstrated that the electrical potential drop near the anode, which has been observed in many laboratory tests, can be simulated by the proposed model.

6

NUMERICAL EVALUATION OF OPTIMAL APPROACHES FOR ELECTRO-OSMOSIS CONSOLIDATION

Numerical simulations are used to identify and evaluate optimum electrode configurations, as well as approaches such as current intermittence and current reversal, which have been proven, experimentally, to be helpful in improving the efficiency of electro-osmosis consolidation of soft clays. A newly developed numerical model that considers coupled electro-osmosis flow, hydraulic flow, and electric density flow, in a deformable porous medium at large strain, is used to simulate the electro-osmosis consolidation. The governing equations of the model are summarized first. Then, various electrode configurations are studied numerically. The results indicate that, with more anodes installed, one can expect more water to drain out and more uniform surface settlement; but, on the other hand, more energy consumption is required. Current intermittence allows more water to be drained out and has a lower energy index compared to a continuous current, although it consumes more energy than the latter. Polarity reversal is also shown to be more efficient than a continuous current supply; moreover, it results in more settlement at the original cathode.

6.1. INTRODUCTION

The consolidation of soft clay creates a lot of problems in foundation engineering. In particular, because of the very low permeability of clay, primary consolidation takes a long time to complete. To shorten this consolidation time, traditional dewatering techniques such as surcharge or preloading, a combination of preloading with prefabricated vertical drains (PVD), and vacuum preloading have been used for many decades (Hansbo et al., 1981; Bergado et al., 2002; Shang et al., 1998; Chu et al., 2000; Indraratna et al., 2011). However, when dealing with materials with low rates of consolidation, low bearing capacity or shear strength, or high compressibility, such as with mine tailings, dredged costal sediments and municipal sludge, new technologies such as electro-osmosis consolidation are often needed. Electro-osmosis is a process that induces the flow of pore fluid in a soil mass from the anode to the cathode, in response to the application of a direct current electric field. The electrodes are generally installed in pairs in the soil mass, between which the direct current forces ions in the mobile part of the electric double layer (EDL) to move to the cathode, dragging water flow with them. Because of this, electro-osmosis permeability is independent of grain size, in contrast to hydraulic permeability which is dependent on grain size. As the flow caused by an electric field is often much greater than that caused by a hydraulic gradient, this means that electro-osmosis has an advantage over conventional treatment, because it accelerates the consolidation process.

6

Numerous laboratory studies have been conducted, to gain insight and to improve the performance of electro-osmosis consolidation. In particular, the influence of the electrode materials and the voltage loss at the soil–electrode interfaces has been studied (Mohamedelhassan and Shang, 2001), with results indicating that the voltage drop is less in metallic anodes than in anodes made of other materials. However, metallic electrodes have corrosion problems which reduces their efficiency. Hence many attempts have been made to develop new electrode materials, with newly developed products such as electric-kinetic geosynthetics (EKG) (Fourie et al., 2007; Glendinning et al., 2008; Jones et al., 2011) and polymeric electrical vertical drains (EVD) (Chew et al., 2004; Karunaratne, 2011) having been recently used as electrodes for electro-osmosis consolidation. On the other hand, chemical treatments have been introduced to improve soil-electrode contacts, as chemical injection at the electrodes has been demonstrated to enhance the transfer of electric potential to the soil (Burnotte et al., 2004; Lefebvre and Burnotte, 2002; Asavadorndeja and Glawe, 2005; Ou et al., 2009).

The area of influence of an electric field for electro-osmosis remediation, for different electrode configurations, was studied numerically by Alshawabkeh and Sheahan (2003), with the analysis identifying the relationship between the minimum cost and electrode spacing. A field trial on sludge using electro-osmosis was reported by Glendinning et al. (2008), in which the treatment time and power consumption of two electrode configurations were studied. Recently, Hu and Wu (2014) studied the settlement of three electrode configurations using a finite element model.

The continuous application of electric current can induce excessive electrode corrosion and high heat generation, which results in an ineffective use of electro-osmosis consolidation. Lockhart and Hart (1988) found that the use of current intermittence in laboratory tests improved the efficiency of electro-osmosis consolidation with respect

to continuous current application. [Micic et al. \(2001\)](#) conducted an experimental investigation into the electro-osmosis strengthening of a marine sediment, with the results demonstrating that the power consumption and electrode corrosion were reduced by using current intermittence. [Mohamedelhassan and Shang \(2001\)](#) reported that, in their experimental research, higher electro-osmosis flow was generated with current intermittence than with a continuous current. [Bjerrum et al. \(1967\)](#) reported the application of current reversal (also known as polarity reversal) in a field test. [Wan and Mitchell \(1976\)](#) found that current reversal can produce a more uniform water content decrease, and thereby strength increase, between electrodes. [Shang \(1997a\)](#) found that current reversal can balance the pH of water at the electrodes, thereby reducing the electrode corrosion.

The aim of this chapter is to numerically investigate various factors for achieving an optimal dewatering effect during electro-osmosis. The first objective is to determine the best electrode configuration for effective dewatering. Further objectives are to demonstrate the efficiency of current intermittence and current reversal, compared to continuous current, during electro-osmosis consolidation. The paper starts by summarizing the numerical model used in the simulations, and then the details of the numerical analyses are presented. The settlement, pore water pressure, outflow rate of water, accumulated volume of water, and electric current, as well as the power consumption of different setups, are illustrated through these numerical examples. The criterion of energy consumption per unit volume of water discharged is employed to evaluate the efficiency of the electro-osmosis consolidation. Moreover, the coefficient of variation of surface settlement is introduced, to evaluate the uniformity of consolidation between the electrodes after electro-osmosis treatment. Hence the numerical simulations provide a strategy for assessing future field applications.

6.2. METHODOLOGY

6.2.1. MODELLING FRAMEWORK

A finite strain numerical model ([Yuan and Hicks, 2013](#); [Yuan et al., 2013](#); [Yuan and Hicks, 2014](#)), which considers coupled electro-osmosis flow under hydraulic and electric potential gradients in a deformable porous medium, is used to conduct the numerical experiments in this chapter. The model incorporates elasto-plasticity to describe soil mechanical behaviour under both saturated and unsaturated conditions, using the Modified Cam Clay (MCC) model ([Roscoe and Burland, 1968](#)) and the Barcelona Basic Model (BBM) ([Alonso et al., 1990](#)), respectively. Void ratio dependent transport and degree of saturation dependent empirical expressions are employed to consider the nonlinear variation of the transport parameters. The governing equations of the finite strain numerical model were provided in Chapter 4 and [Yuan and Hicks \(2014\)](#), and are therefore not reintroduced here.

6.2.2. POWER CONSUMPTION AND ENERGY INDEX

The efficiency of electro-osmosis consolidation can be evaluated by several performance metrics, such as the power consumption, the settlement achieved or volume of water drained out, or the time elapsed to achieve a certain settlement. The two key outputs of the consolidation process are the power consumption and water drained out, as they

determine the feasibility of the application. The optimal application is to discharge a sufficiently high volume of water out of the soil, given a relatively small energy consumption and short elapsed time. A more meaningful criterion, the energy index (kWh/m^3) is introduced here to evaluate the economic efficiency of electro-osmosis consolidation. This is the power consumption to drain one cubic meter of water out of the soil mass, and is a function of the voltage applied and current, i.e.

$$E = \frac{W}{vol} = \frac{1}{vol} \int V I dt \quad (6.1)$$

where W is the power, in kWh, vol is the volume of water discharged from the soil, in m^3 and I is the current, in A.

6.3. NUMERICAL EXAMPLES

This section comprises three numerical simulations: an assessment of the optimization of the electrode configuration; a comparison between intermittent current and continuous current approaches; and a comparison between current reversal and continuous current. Each simulation is based on different material properties and model domains (either 2D or 3D), and is conducted under large strain conditions. The simulations consider both saturated soil and unsaturated soil, by employing the MCC or BBM constitutive models, respectively. In all examples, the initial effective stresses have been assigned by using the effective unit weight of the soil and the coefficient of earth pressure at rest. The initial yield surface location is determined according to the effective pressure and assumed over-consolidation ratio. The model domains, adopted material properties and other details are described as follows.

6.3.1. EXAMPLE 1: ELECTRODE CONFIGURATIONS

3D models are used to investigate the efficiency of various electrode configurations. The main focus is to find the optimized anode configuration; that is, the one with the lowest energy index. The domain is a 1 m cube and the electrodes are assumed to be 0.02 m in diameter and 0.75 m long. Figure 6.1 shows a plan view of the four electrode configurations considered. In configuration A, one pair of electrodes is installed in the middle of the domain, with a spacing of 0.3 m between the anode and cathode. In configuration B, one cathode with two anodes are installed at 0.3 m spacing, in a single row located in the middle of the domain. In configuration C, one central cathode is surrounded by four anodes, with a spacing of 0.3 m between the cathode and each anode. In configuration D, a central cathode is surrounded by eight anodes, to form a regular grid of 0.3 m spacing.

The transport parameters are selected from laboratory tests on the electro-osmosis of a marine sediment, carried out by [Mohamedelhassan and Shang \(2002\)](#), including the following empirical expressions:

$$\begin{aligned} \log k_w &= 1.1075e - 11.297 \\ k_{eo} &= 3.27 \times 10^{-8} n - 1.14 \times 10^{-8} \\ k_{\sigma e} &= \frac{0.42(1 + e)}{1.29 + 0.33e} \end{aligned} \quad (6.2)$$

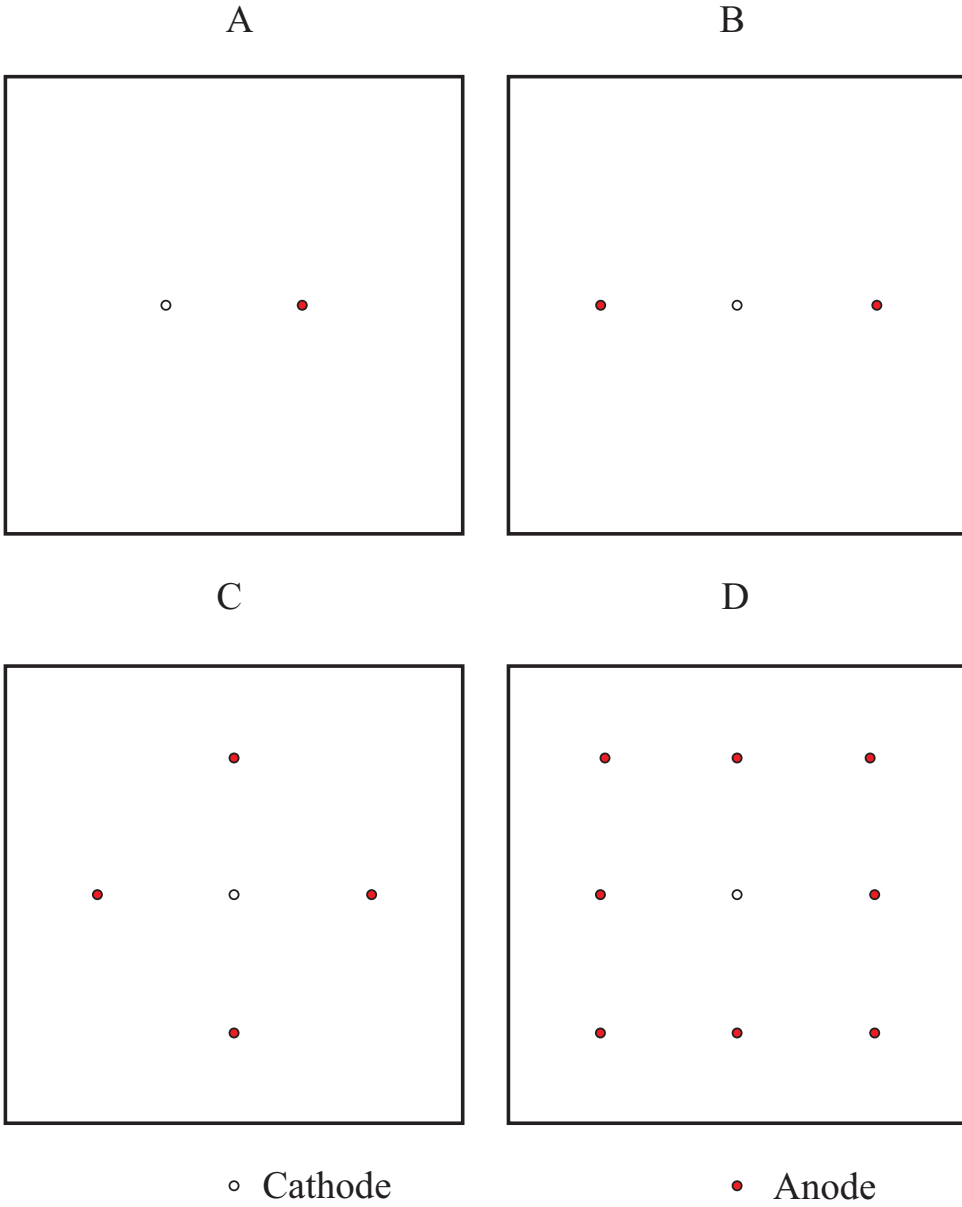
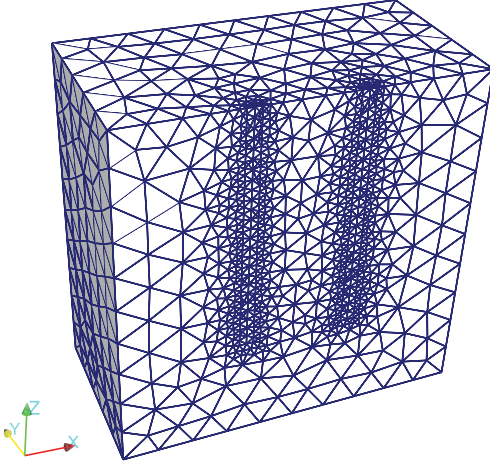


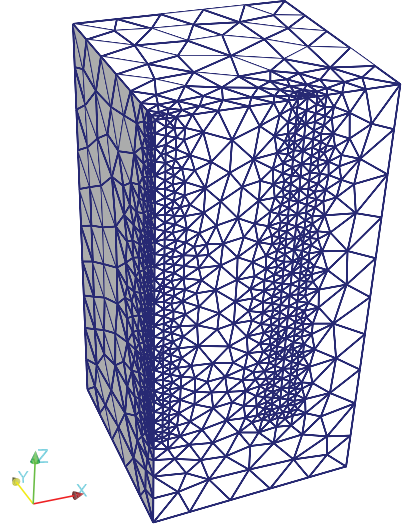
Figure 6.1: Plan view of analysed electrode configurations.

Saturated conditions are considered in this example. The material parameters for the MCC model are listed in Table 6.1, and are also derived from Mohamedelhassan and Shang's (2002) tests.

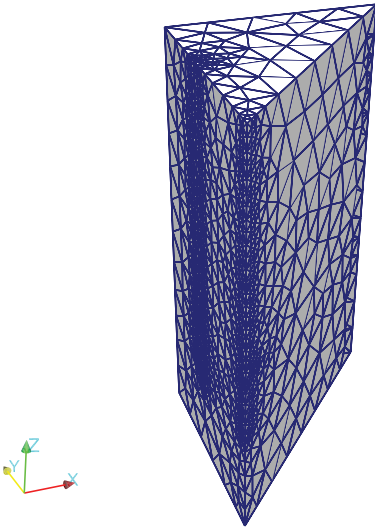
A



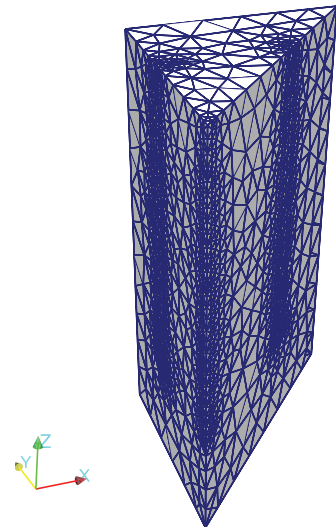
B



C



D



6

Figure 6.2: 3D finite element meshes for analysed electrode configurations.

Table 6.1: Material parameters for the MCC model (based on [Mohamedelhassan and Shang \(2002\)](#))

Void ratio at $p' = 1$ kPa	e	3.95
Poisson's ratio	ν	0.3
Plastic compression index	λ	0.547
Unloading–reloading index	κ	0.064
Critical stress ratio	M	1.172
Over-consolidation ratio	OCR	1.0
Coefficient of earth pressure at rest	K_0	1.0
Total unit weight of soil	γ	19 kN/m ³

3D analyses are carried out to simulate the conditions imposed on the cubic domain, although only 1/2, 1/4, 1/8 and 1/8 of the problem are considered, due to the planes of symmetry for configurations A, B, C and D, respectively. Figure 6.2 shows the geometries of the meshes used in the analyses. The mesh boundary conditions are that the vertical sides are prevented from moving in the horizontal plane, whereas the bottom boundary is fixed. In terms of hydraulic boundary conditions, the top surface is open and free draining, whereas the remaining boundaries are impermeable; in order to maintain a draining condition, a hydraulic conductivity of 1.0×10^{-4} m/s is assumed at the cathode. For the electrical boundary conditions, voltages of 5 V and 0 V are maintained at the anode and cathode, respectively, whereas all other boundaries are assumed to be impermeable to electric current. Note that an electrical conductivity of 1.0×10^6 S/m is assumed for the steel electrodes. A four-node tetrahedron finite element is adopted for displacements, pore water pressure and electrical potential.

6.3.2. EXAMPLE 2: CURRENT INTERMITTENCE

Current intermittence is the application of a pulse voltage at predetermined on/off intervals during the electro-osmosis consolidation. Recent experimental research has indicated that an intermittent current is beneficial to electro-osmosis consolidation compared to a continuous current ([Mohamedelhassan and Shang, 2001](#); [Micic et al., 2001](#)). A 2D square domain of 1 m side length (see Figure 4.6) is used to investigate the use of current intermittence for an unsaturated clay. The boundary conditions are as follows: the left edge is impermeable and on rollers allowing only vertical movement; the right edge is free draining and on rollers allowing only vertical movement; the bottom boundary is impermeable and fixed; and the top boundary is free draining. In terms of electrical boundary conditions: the anode is along the left edge, the right edge is the cathode, and the horizontal boundaries are impermeable to electric current.

For both simulations (continuous and intermittent current), the power-on time is 5×10^6 seconds. For the intermittent current analyses, the total simulation time is 9×10^6 seconds and there are four intermittences in the applied input voltage, each lasting for 1×10^6 seconds, as shown in Figure 6.3. Unsaturated conditions are considered in this example; hence the same material parameters as used in the previous example for saturated conditions are employed here, plus additional material parameters that are needed

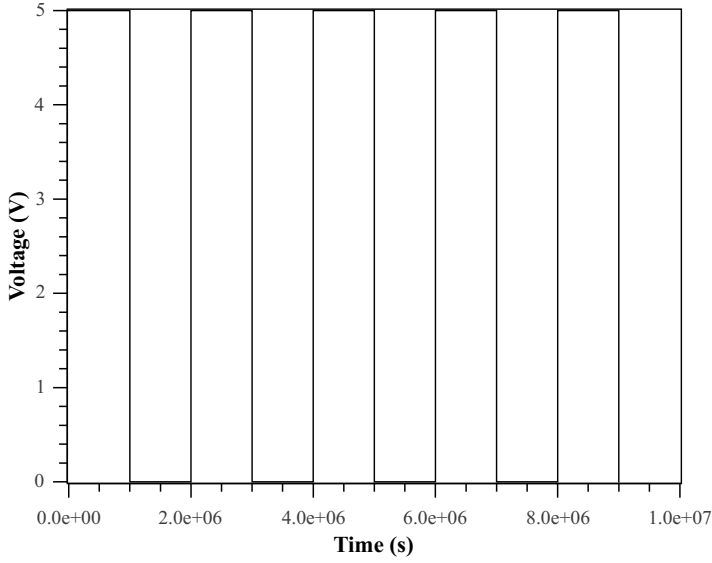


Figure 6.3: Applied input voltage for current intermittence simulation.

6

Table 6.2: Material parameters for the Barcelona Basic Model (after Sheng et al. (2003b))

Reference stress	p_r	1.0 kPa
Rate of increase of soil stiffness with suction	β	0.012 kPa ⁻¹
Parameter define the maximum soil stiffness	r	0.75
The rate of cohesion increase with suction	k_s	0
Elastic compression index with respect to suction	κ_s	0
The degree of non-associativity of the flow rule	α	0.437

for the BBM with Bishop's effective stress. These are adopted from Sheng et al. (2003b) and are listed in Table 6.2. Moreover, to model the dependence of relevant parameters on the degree of saturation, the following empirical expressions have also been adopted (Tamagnini et al., 2010):

$$\begin{aligned}
 S_w &= (1 + (\alpha s)^n)^{-m} \\
 k_{rw} &= a_w (S_w)^{b_w} \\
 k_{rg} &= a_g (S_g)^{b_g} \\
 k_{reo} &= a_{eo} (S_w)^{b_{eo}} \\
 k_{\sigma e} &= a_e (S_w)^{b_e}
 \end{aligned} \tag{6.3}$$

in which $n = 1.31$, $m = 11/n$, $\alpha = 0.00851 \text{ kPa}^{-1}$, $a_w = 1$, $b_w = 5$, $a_g = 1$, $b_g = 5$, $a_{eo} = 1$, $b_{eo} = 3.2$, $a_e = 1$ and $b_e = 2$, are material constants. In this example, an eight-node quadrilateral finite element is adopted for displacements, and this is coupled to a four

node quadrilateral element for modelling pore water pressure and electrical potential.

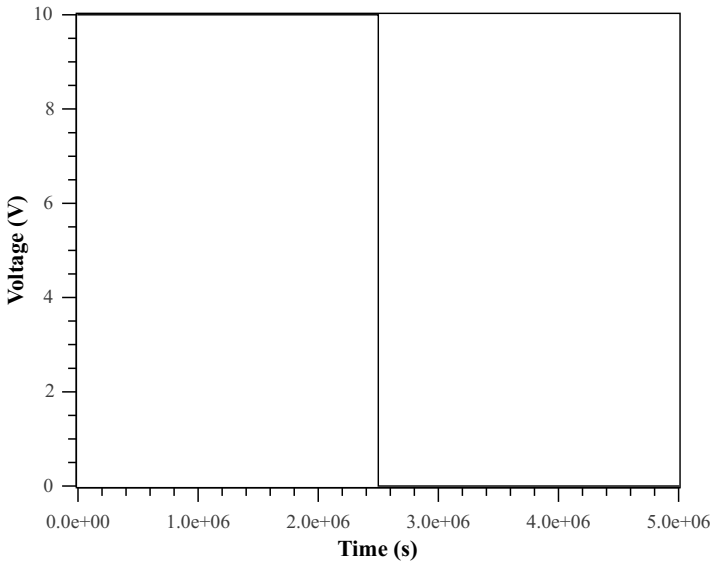


Figure 6.4: Applied input voltage for current reversal simulation.

6.3.3. EXAMPLE 3: CURRENT REVERSAL

In order to study the effects of current reversal during electro-osmosis consolidation, the 2D model is subjected to a voltage of 5 V, with a voltage reversal mid-way through the simulation (Figure 6.4). Once again, unsaturated conditions are considered, and the same material properties as in the previous simulation are used. The boundary conditions are the same as in the previous simulation for the first 2.5×10^6 seconds, before the polarity reversal. The current is reversed at 2.5×10^6 seconds and, at this time, the hydraulic boundary conditions are also reversed: that is, the left edge (former anode) is now free draining and the right edge (former cathode) is now impermeable. The remaining boundary conditions are the same as before the polarity reversal.

6.4. RESULTS AND DISCUSSION

6.4.1. ELECTRODE CONFIGURATIONS

The water outflow rates through the cathode, for the four electrode configurations, are shown in Figure 6.5. The water outflow rates decrease with time, due to the negative pore water pressure developed near the anode causing a hydraulic flow which is opposite to the direction of electro-osmosis flow. Hence, when the hydraulic flow equals the electro-osmosis flow the system reaches the steady state. The figure shows that, with more anodes installed around the cathode, a higher water outflow rate is achieved. However, the nonlinear response between water outflow rate and the number of anodes indicates that there is an optimum anode number. Figure 6.6 shows the accumulated volume of

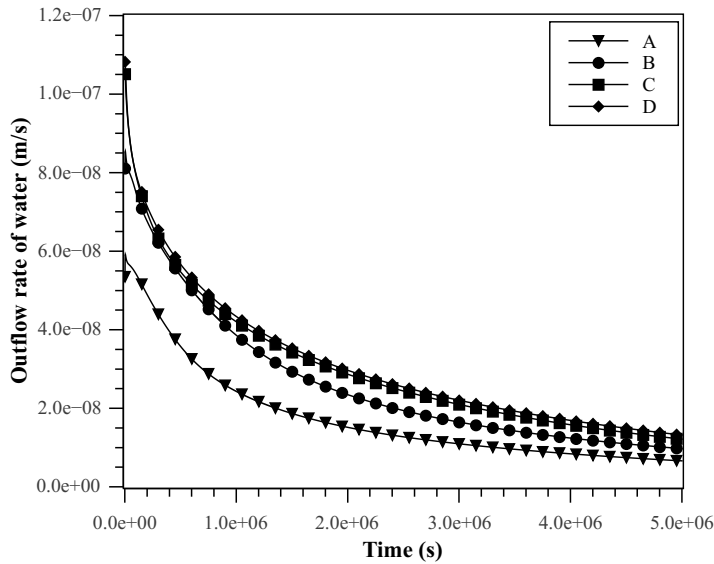


Figure 6.5: Influence of various electrode configurations on evolution of water outflow rate through the cathode.

6

water exiting through the cathode; as expected, with more anodes installed around the cathode, there is a greater outflow of water. Configuration B gives an outflow that is about 50% greater than that of configuration A, whereas configurations C and D indicate a rather modest additional outflow of water.

Figure 6.7 shows the evolution of electric current through the cathode. Note that, since the electrical conductivity is decreasing with void ratio, as described in Eq. (6.2), the electric current is also decreasing with time. The time evolution of the energy consumption, for the various electrode configurations, is shown in Figure 6.8. The investigated electrode configurations show that, with more anodes installed, more water is draining out and the time required to reach a certain accumulated volume of water is less, although the increase in the number of anodes results in a greater energy consumption. So, the energy index introduced in Section 6.2 is used as a criterion to evaluate and compare the consolidation effects of the various configurations. As shown in Figure 6.9, configuration A has the lowest energy index; moreover, the energy indices for one (A) and two (B) anodes around the cathode are significantly less than for four (C) and eight (D) anodes, indicating that they are more energy efficient. The coefficients of variation of surface settlement for the various electrode configurations are shown in Figure 6.10, in which the coefficient of variation is equal to the standard deviation of the surface settlement divided by the mean. It is seen that configurations C and D have much smaller coefficients of variation than configurations A and B, which indicates that, although configurations C and D have the higher energy indices, the obtained surface settlement between the electrodes is more uniform for these cases.

Considering all the results illustrated in this section, configurations A C and D give a

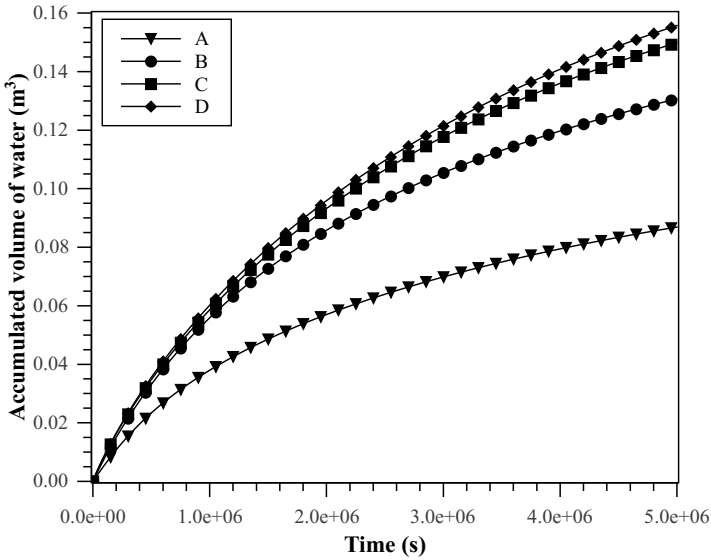


Figure 6.6: Influence of various electrode configurations on evolution of accumulated volume of water exiting through the cathode.

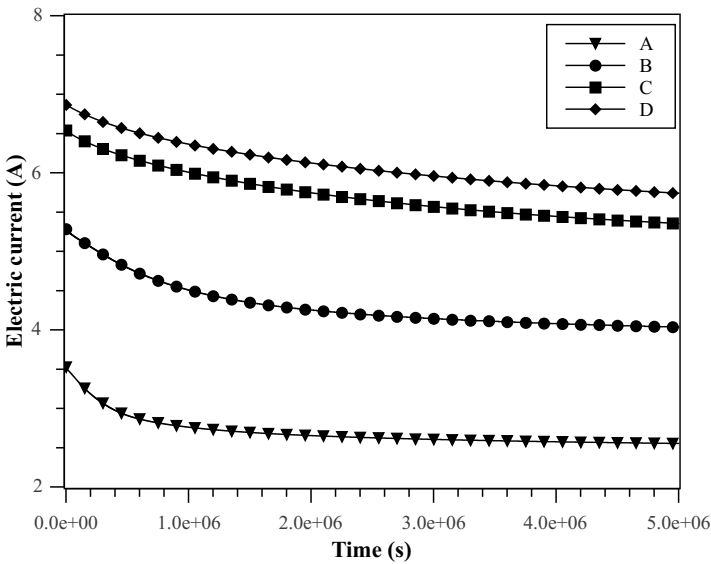


Figure 6.7: Influence of various electrode configurations on evolution of electric current current through the cathode.

larger volume of drained water and a much more uniform surface settlement profile than configurations A and B, but they also have greater energy indices. Configuration

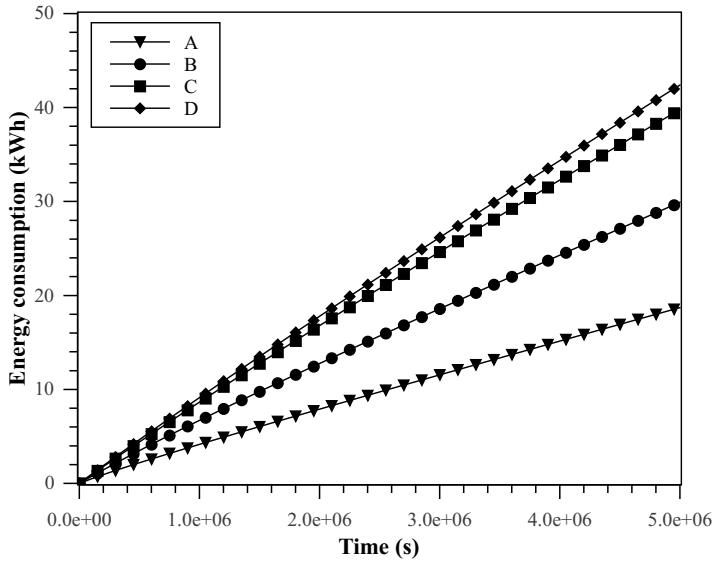


Figure 6.8: Influence of various electrode configurations on evolution of energy consumption.

6

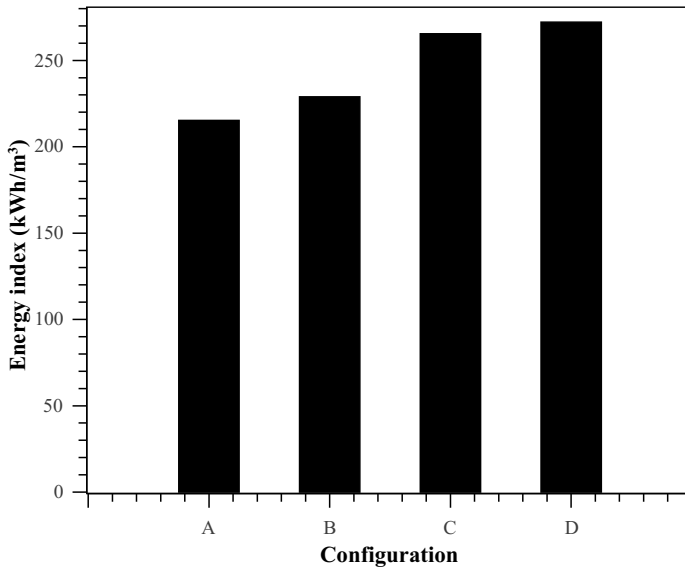


Figure 6.9: Influence of various electrode configurations on energy index.

A is the most efficient electrode installation, from the economic point of view, but results in the largest differential settlement. Configuration C has a slightly smaller energy index than configuration D, but requires only half as many installed anodes to achieve

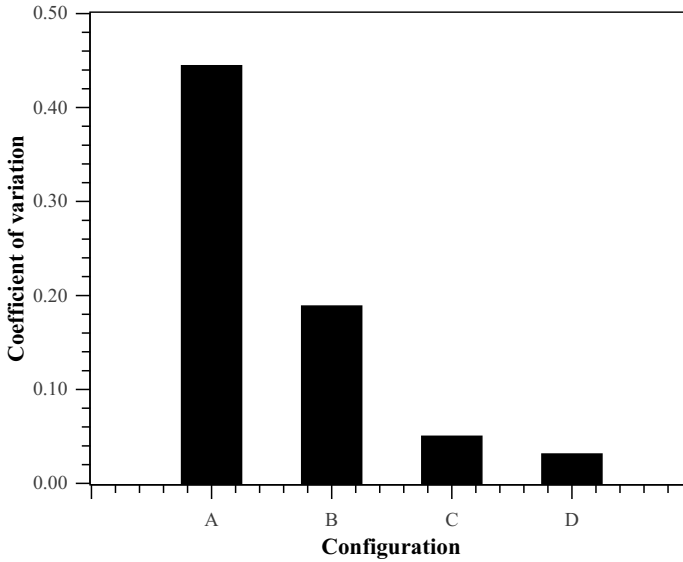


Figure 6.10: Influence of various electrode configurations on coefficient of variation of settlement.

almost the same volume of water drained out and gives a similar (low) coefficient of variation of the surface settlement. This suggests that, if reducing the volume of water in the soil mass and having more uniform consolidation between the electrodes are the primary objectives of the electro-osmosis consolidation, then this can best be achieved by an increased number of anodes (configuration C), although it will come at the cost of increased energy consumption. If a low cost of consolidation is the objective, but with a reasonably uniform consolidation between the electrodes, then electrode configuration B is recommended.

6.4.2. CURRENT INTERMITTENCE

Figure 6.11 shows the water outflow rate through the cathode for continuous and intermittent applied currents. (In order to better compare the results, the current-off times are not included in the following figures; therefore, both simulations have the same x axis length.) There is a gradual reduction in the overall flow rate as the consolidation progresses, with a peak in the flow rate observed when the current is reapplied after each period of zero current (i.e. in the intermittent case). This is because, during the no current period, the negative pore water pressure will partially dissipate due to the pore water redistributing in the domain, so that after the current is reapplied the outflow rate is much bigger than in the continuous current approach. Note that the small drop in outflow rate at the beginning of the simulation is due to the hydraulic conductivity being very small. Hence, the bulk of the water cannot flow out immediately, but remains in the middle of the domain causing a positive pore water pressure; this makes the water outflow rate drop temporarily, but, as the positive pore water pressures dissipate, the water outflow rate recovers. The evolution of accumulated volume of water exiting through

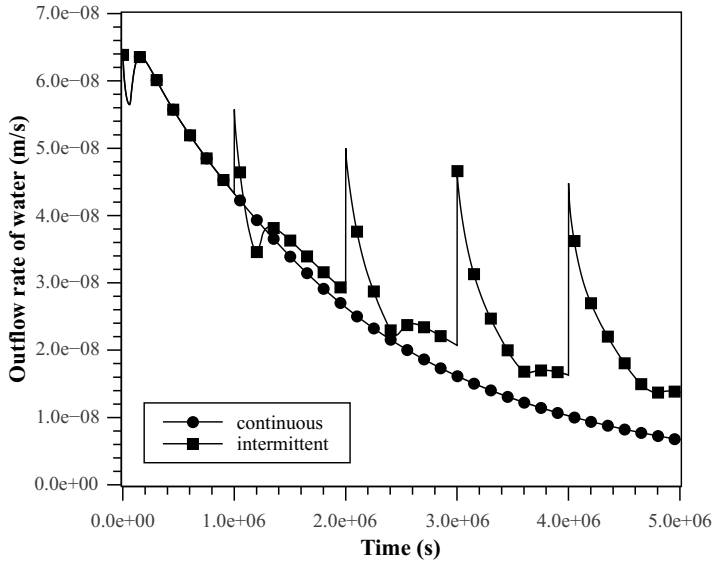


Figure 6.11: Influence of current intermittence on evolution of water outflow rate through the cathode.

6

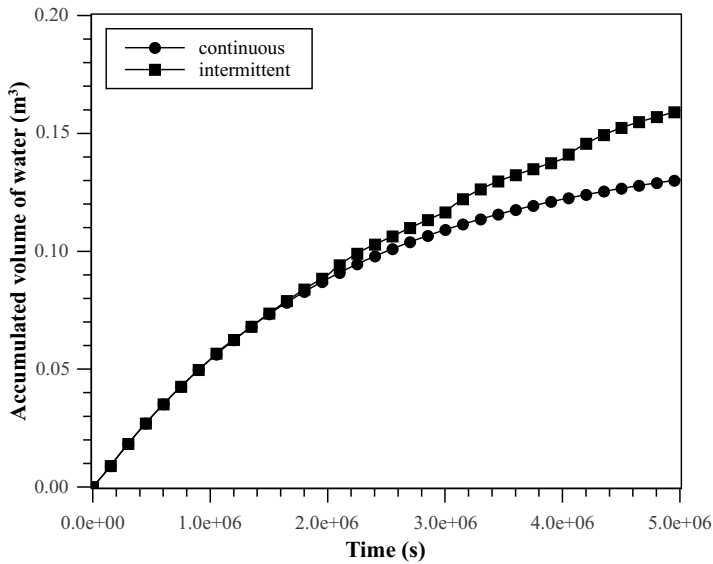


Figure 6.12: Influence of current intermittence on evolution of accumulated volume of water existing through the cathode.

the cathode, for intermittent and continuous currents, is shown in Figure 6.12. It is seen that, before 2×10^6 seconds, the accumulated volume of water for both simulations is

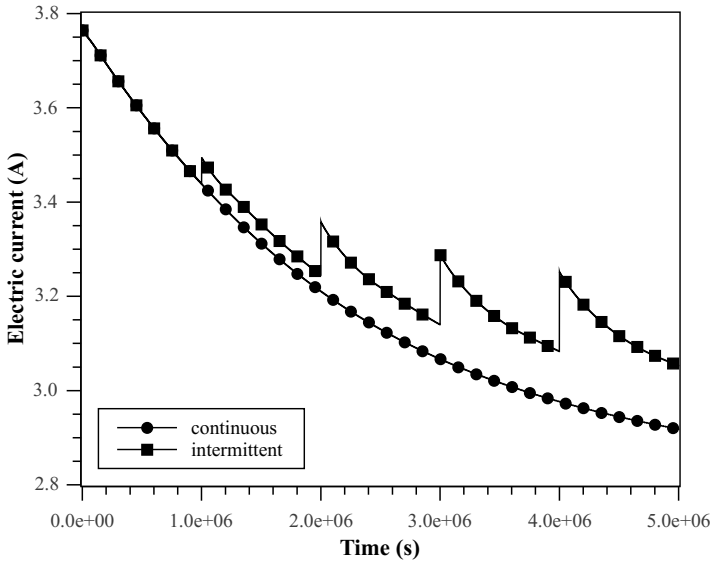


Figure 6.13: Influence of current intermittence on evolution of electric current through the cathode.

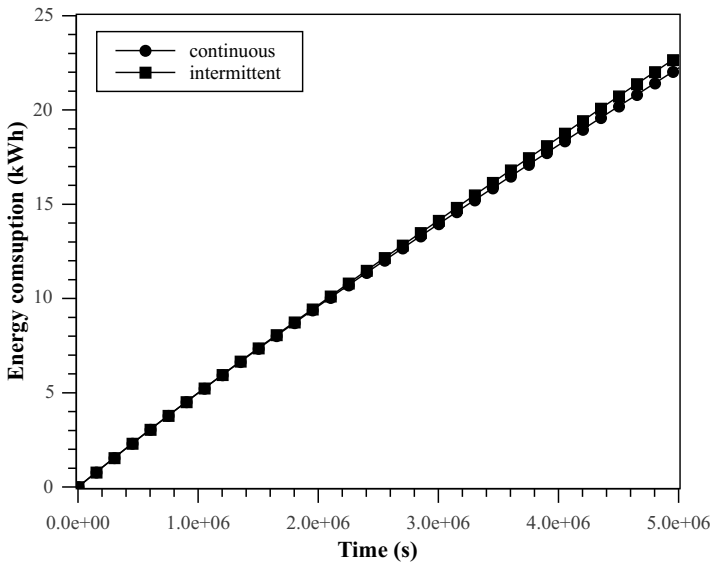


Figure 6.14: Influence of current intermittence on evolution of energy consumption.

almost the same. However, as the consolidation progresses, the volume of water accumulated from the intermittent current is greater than that from the continuous current, due to the increase in the outflow rate each time the current is reapplied.

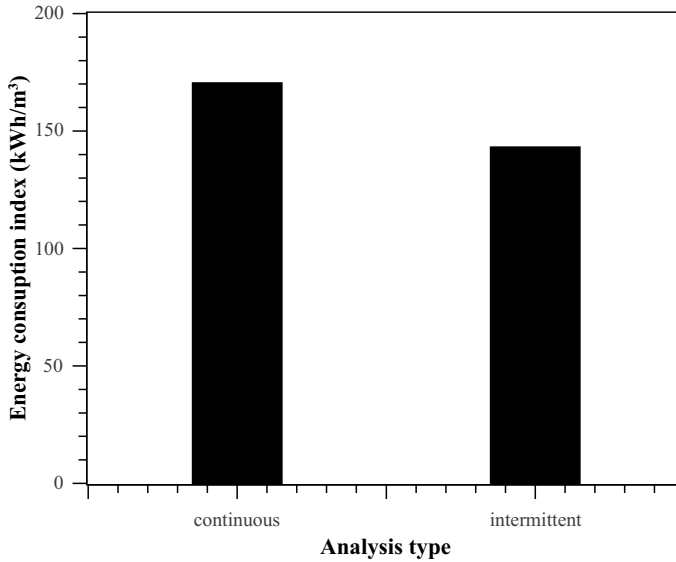


Figure 6.15: Comparison of energy index for continuous and intermittent currents.

The evolution of electric current through the cathode has a similar trend to the water outflow rate. As shown in Figure 6.13, a brief peak in the current is found when the voltage is reapplied; indeed, this is a common observation during laboratory tests of electro-osmosis (Glendinning et al., 2008). As explained before, the negative pore water pressures developed near the anode will dissipate as the water redistributes within the domain, and the soil deformation will rebound slightly, when the current is off. Due to the degree of water saturation and soil void ratio both increasing, according to Eqs. (6.2) and (6.3), the electric conductivity will therefore increase when the current is off. Hence when the voltage is reapplied after a period of zero voltage, the electric current will peak. As a higher current is obtained after the current is intermitted, a slightly higher energy consumption compared to a continuous current is apparent, as seen in Figure 6.14. However, the volume of water drained out of the soil is also greater compared to the continuous current. Hence in order to evaluate the efficiency of both methods, the energy index is plotted in Figure 6.15. It is seen that the energy index for the intermittent current is around 16% smaller than that for the continuous current, which indicates that current intermittence can reduce the power consumption required to drain a certain volume of water, thereby enhancing the effectiveness of electro-osmosis treatment.

6.4.3. CURRENT REVERSAL

The impact of reversing the electric current (at 2.5×10^6 s) is compared to the case of no current reversal in Figures 6.16-6.21. The simulation results suggest that soil samples tested using current reversal have a higher cathode surface settlement than those conducted using a continuous current. With current reversal, there is only a slight settlement rebound found at the top of the original anode, but a much higher surface settlement is

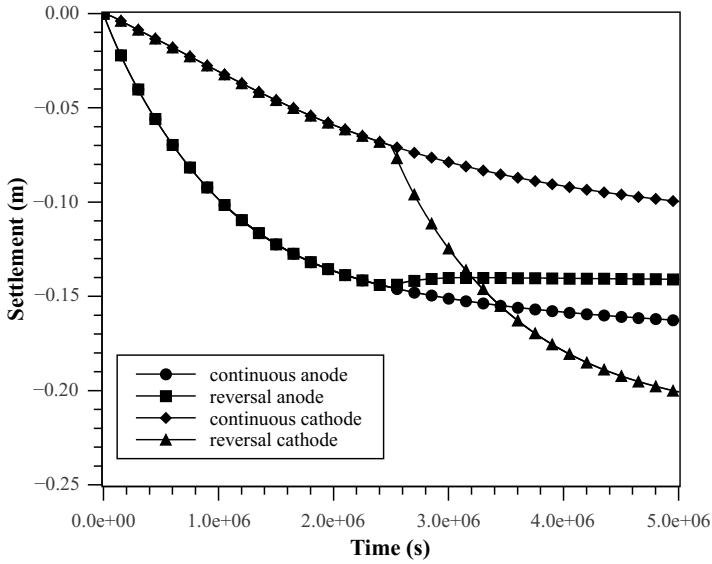


Figure 6.16: Influence of current reversal on evolution of surface settlements at original anode and cathode.

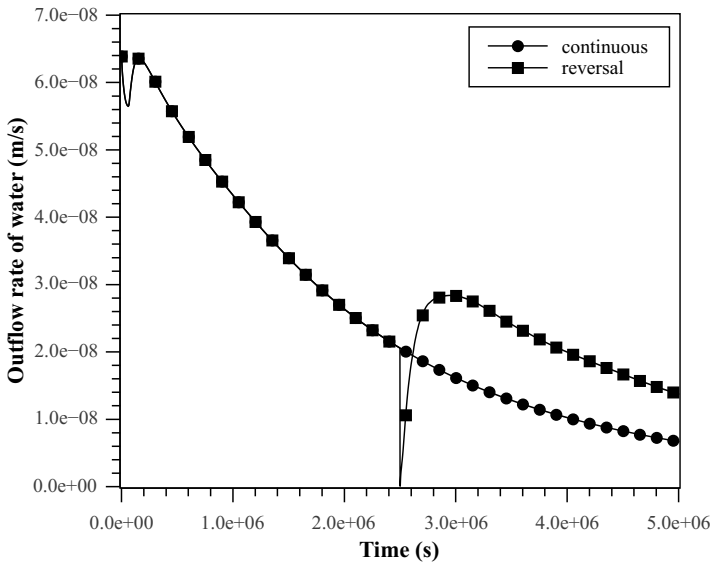


Figure 6.17: Influence of current reversal on evolution of water outflow rate through the cathode.

obtained at the top of the original cathode (even higher than the settlement at the anode without current reversal), as shown in Figure 6.16.

The effect of current reversal is that the water outflow rate is decreased to almost zero

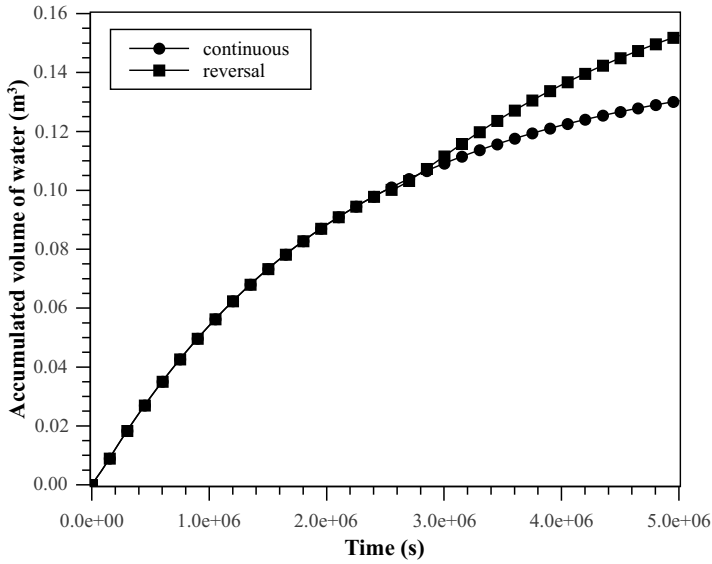


Figure 6.18: Influence of current reversal on evolution of accumulated volume of water existing through the cathode.

6

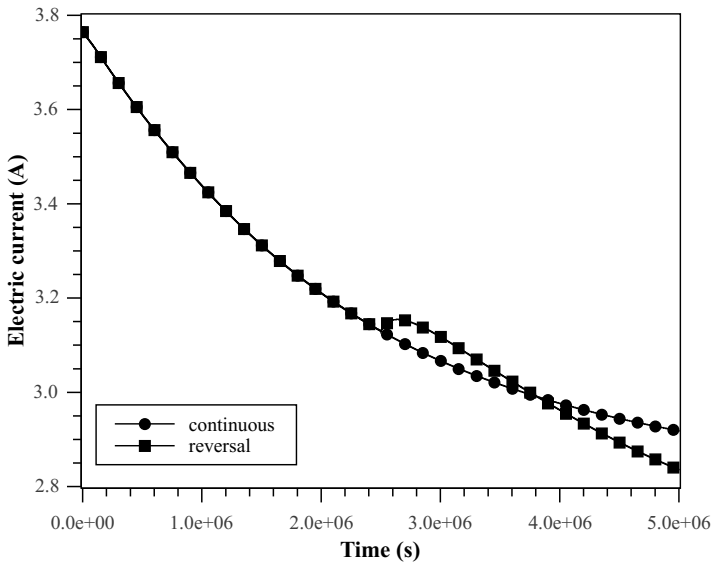


Figure 6.19: Influence of current reversal on evolution of electric current through the cathode.

immediately after the reversal and then it increases rapidly to a value which is greater than that for the continuous current (Figure 6.17), resulting in a greater volume of water

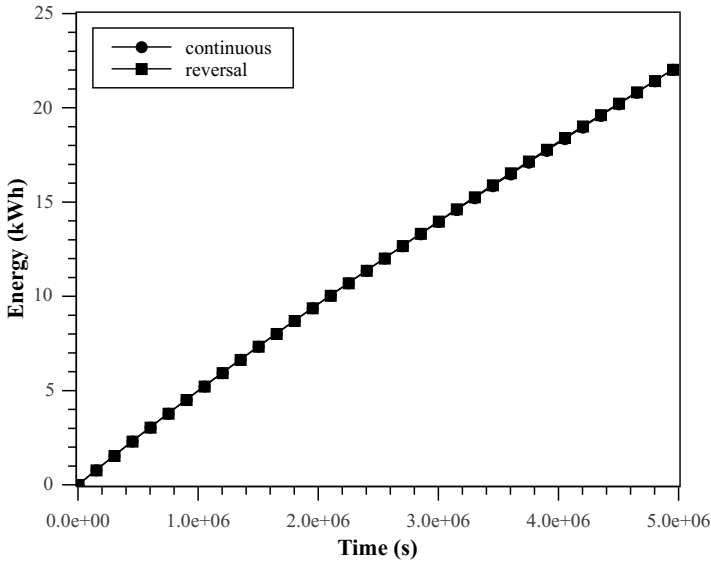


Figure 6.20: Influence of current reversal on evolution of energy consumption.

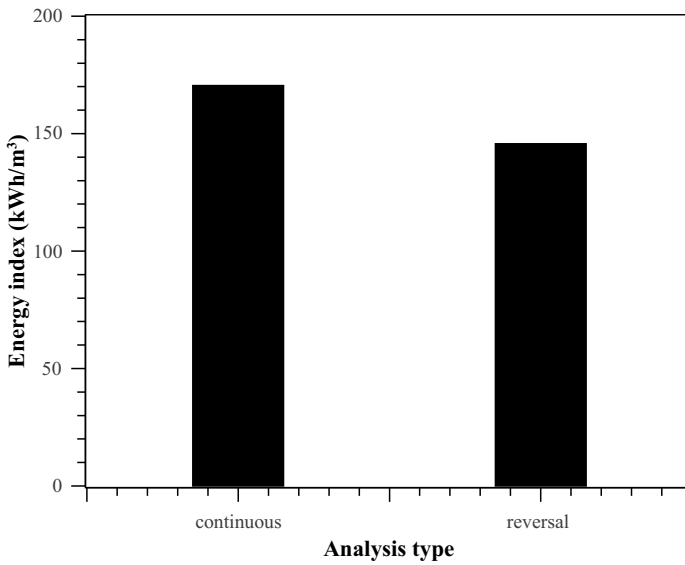


Figure 6.21: Comparison of energy index for continuous and reversal currents.

accumulated through the cathode after 3×10^6 seconds compared to when a continuous current is applied (Figure 6.18). This is because, after current reversal, the negative pore water pressures near the former anode are not dissipated immediately, which causes a

local hydraulic flow that is in the opposite direction to the electro-osmosis flow; hence the water outflow rate decreases to zero at the new cathode. However, when the current is reversed the hydraulic boundary conditions are also reversed and so the left edge becomes open for free drainage; hence the negative pore water pressure can dissipate rapidly, while, at the same time, the outflow rate increases rapidly. Because of the water redistribution within the domain after the current is reversed, the soil becomes more saturated, resulting in an enhanced water outflow rate compared to the case with no current reversal, as seen in Figure 6.17.

Figure 6.19 shows the electric current through the cathode versus time, for both the continuous and current reversal cases, showing that the current decreases gradually as the consolidation progresses. However, there is a slight increase in the current to a peak value immediately after the current is reversed, followed by a reduction of the current at a rate that is greater than that for a continuous current. The evolution of energy consumption is shown in Figure 6.20. It is seen that current reversal results in no noticeable increase in energy consumption, due to the current decreasing more rapidly after the initial peak current, as seen in Figure 6.19. However, the simulation with electric current reversal requires less energy consumption per volume of water drained out of the soil, as seen in Figure 6.21, despite the energy consumption being almost the same, due to the greater volume of water being drained compared to the continuous current case. Hence the energy index is around 15% smaller for the case of current reversal.

6.5. CONCLUSIONS

Various electrode configurations, as well as current intermittence and current reversal approaches for electro-osmosis consolidation have been investigated using numerical simulation. 3D and 2D domains have been analyzed to simulate the time dependent behaviour of the settlement, pore water pressure, outflow rate of water, accumulated volume of water and electric current, as well as the power consumption of different setups. In particular, the combination of a nonlinear elasto-plastic constitutive model and relationships for hydraulic conductivity, electro-osmosis permeability and electrical conductivity as a function of the void ratio and degree of water saturation, have allowed the model to capture the coupled nonlinear response during electro-osmosis consolidation at large strain.

Four electrode configurations have been analyzed using a 3D model domain, with the simulation results indicating that a greater number of anodes installed around the central cathode leads to expedited consolidation and an increased settlement, albeit with greater energy consumption. The often nonlinear response between the energy index and surface settlement indicates the need to optimize each approach for a particular application.

2D simulations comparing the performance of intermittent and continuous currents have shown that, in general, intermittent current leads to a greater volume of water being drained out from the soil than for a continuous current. However, the analyses have also shown that the energy consumption for an intermittent current is greater than that for a continuous current. By computing the energy index of both simulations, it is concluded that the efficiency of electro-osmosis consolidation is greater when using current intermittence than when a continuous current is applied.

The results of a numerical simulation using current reversal have shown that the reversal of the electric field enhances consolidation between the electrodes, as indicated by a higher surface settlement at the original cathode when current reversal was used. Moreover, the numerical results have illustrated that the efficiency of consolidation with current reversal is greater than with a continuous current.

The findings of the numerical simulations for current intermittence and reversal are consistent with those reported in previous laboratory tests. In general, the results of the numerical simulations have shown that the process of electro-osmosis consolidation is enhanced by an increase in the number of anodes, as well as by an intermittent current and current reversal. Due to the considerations of consolidation time, energy consumption and uniformity of consolidation for a particular site, the use of numerical modelling has a potential use in optimizing the design of field applications using electro-osmosis consolidation.

7

CONCLUSION AND RECOMMENDATIONS

7.1. CONCLUSIONS

Electro-osmosis is a novel technique to consolidate soft clays. Electro-osmosis is one of the electro-kinetic phenomena, and is the movement of water under the influence of a direct current electric field. Electro-osmosis flow is a function of voltage gradient and is independent of grain size; this means that electro-osmosis can generate flow rates that are 100 to 1000 times greater than hydraulic flows in fine grained soft clays, because the value of electro-osmosis permeability is greater than that of the hydraulic conductivity. Therefore, electro-osmosis treatment has been applied in the field in numerous applications (Casagrande, 1952; Bjerrum et al., 1967; Lo et al., 1991a; Burnotte et al., 2004). Consolidation theory of electro-osmosis was first conducted by Esrig (1968). Many researchers then developed various analytical and finite element models (Wan and Mitchell, 1976; Lewis and Garner, 1972; Feldkamp and Belhomme, 1990; Shang, 1998a), although such models are limited and cannot fully handle problems with complicated boundary conditions and geometries; or directly consider the force equilibrium; or are incorporated with an elasto-plastic constitutive relationship; or consider large strain.

In this thesis, numerical models for the electro-osmosis consolidation of soft clays in multi-dimensional domains at large strain are presented, which consider the full coupling of the soil mechanical behaviour, pore water transport, pore gas transport and electric flow. In particular, elasto-plastic constitutive models (i.e. the Modified Cam Clay model and Barcelona Basic Model) are employed to describe the mechanical behaviour of the clay. The presented formulations are written in an Updated Lagrangian form based on the current configuration and implemented in a finite element code. The proposed models have been verified against analytical/numerical solutions and also evaluated with results obtained from laboratory and field experiments. Overall, excellent agreement has been found, which demonstrates the accuracy and efficiency of the proposed models. In addition, further numerical examples have been carried out, investigating the time dependent evolution of degree of consolidation, settlement, pore water pressure, and electric current during the electro-osmosis consolidation process, and differences between models based on small and large strain theory are highlighted.

The specific conclusions drawn from this research are summarized as follows:

- (i) The developed numerical models for electro-osmosis consolidation, considering elasto-plastic constitutive models and nonlinear transport parameters at large deformation, can capture the main features of electro-osmosis and well predict the time dependent nature of the problem.
- (ii) Excellent agreement between the results of the proposed model and the analytical solution of Esrig (1968) are found. Moreover, the numerical results of the unsaturated code are in excellent agreement with Lewis and Schrefler (1998) in modelling the draining of a sand column, thereby demonstrating the accuracy of the proposed model in simulating three phase unsaturated consolidation.
- (iii) Large deformation is considered in this research. Updated Lagrangian formulations are employed to account for the geometric nonlinearity, and the differences between large strain and small strain are highlighted, demonstrating that large deformation consolidation theory is often necessary. The numerical results indicate

that the excess pore water pressures develop faster in the large strain model than in the small strain model, finally reaching the same value at the steady state. In terms of deformation, the final settlements predicted by the large strain model are always smaller than those predicted by the small strain model.

- (iv) The deformation is the key concern during consolidation behaviour. However, most previous theories do not directly consider the soil deformation, with the force equilibrium of the soil being included implicitly in the formulation of the pore water transport based on Terzaghi's consolidation theory. Moreover, a linear elastic constitutive relationship is often employed by previous theories. In contrast, in this research the force equilibrium is directly considered in the governing equations. Furthermore, this study has focused on the elasto-plastic mechanical behaviour of soil, which has not been done before. The numerical results for settlement and excess pore water pressure demonstrate that the effectiveness of electro-osmosis consolidation may be significant compared to the normal surcharge consolidation.
- (v) The ratio of electro-osmosis permeability and hydraulic permeability k_{eo}/k_w is a key factor in electro-osmosis consolidation. In engineering design, in order to generate electro-osmosis consolidation effects, the ratio k_{eo}/k_w should be higher than 0.1 (Mohamedelhassan and Shang, 2001). Generally, electro-osmosis permeability and hydraulic permeability decrease with the decrease in void ratio and degree of water saturation, but the decrease in hydraulic conductivity is much faster than the decrease of electro-osmosis permeability, so the ratio k_{eo}/k_w increases during the consolidation process. Therefore, previous theories of electro-osmosis consolidation that considered constant transport parameters have some limitation. A field test of electro-osmosis consolidation (Bjerrum et al., 1967) has been analysed, showing excellent agreement between the computed and measured settlements. The results show that consideration of geometrical nonlinearity causes a reduction in the settlements relative to small strain simulations, and this effect increases with time as the consolidation progresses. However, the differences between the two solutions is relatively small in this example due to the strains being only moderate ($\approx 8\%$). The impact of the current intermittence and reversal on settlement during the field test have been well reproduced by the numerical simulation.
- (vi) The unsaturated conditions caused by the development of both negative pore water pressures and gas generated at the anodes are considered in the proposed model. The Barcelona Basic Model is employed within the formulation to simulate the elasto-plastic mechanical behaviour of unsaturated clays. Under unsaturated conditions, the transport parameters of the soil are strongly dependent on the degree of water saturation, with changes in the degree of water saturation resulting in changes in the ratio of k_{eo}/k_w , which is the governing factor for electro-osmosis consolidation. Furthermore, the efficiency of the gas production η is studied, showing that the pore water pressure drop at the anode becomes greater with an increase of η . On the other hand, the higher the amount of gas generated at the anode, the smaller the final surface settlement. The pore gas pressure near the anode increases due to the gas generation. The increase of pore gas pressure moves towards

the cathode with time. By employing the BBM, it has been shown that the soil becomes much stiffer due to desaturation at the anode, resulting in significantly less predicted settlement in this region compared to results obtained using the MCC model.

- (vii) The proposed governing equations are implemented into a finite element code based on the finite element programming strategy of [Smith and Griffiths \(2004\)](#). This numerical tool is able to simulate field applications with complicated boundary and geometry conditions, as well as practical applications such as current intermittence and polarity reversal, which are often employed in the field to achieve efficient and economical consolidation. This numerical tool also has potential use in engineering designs to identify and evaluate optimum approaches for field applications. Various electrode configurations, as well as current intermittence and current reversal approaches for electro-osmosis consolidation have been investigated using this numerical tool. 3D numerical simulation results indicate that a greater number of anodes installed around the central cathode leads to expedited consolidation and an increased settlement, albeit with greater energy consumption. From 2D simulations comparing the performance of intermittent and continuous currents, it is concluded that the efficiency of electro-osmosis consolidation is greater when using current intermittence than a continuous current. The results of numerical simulations have shown that, although the efficiency of consolidation with current reversal is only slightly greater than with continuous current, it enhances consolidation between the electrodes.

7

7.2. RECOMMENDATIONS FOR FUTURE WORK

There are many issues which have not been covered in this research. Some recommendations for further studies are listed as follows :

- (i) The proposed model is only validated against one analytical solution and one large strain experimental test. Laboratory tests of electro-osmosis need to be carried out to further verify the proposed numerical models.
- (ii) Although numerous field and laboratory tests of electro-osmosis consolidation have been reported in the literature, most of them were carried out under saturated conditions. However, formation of gas due to electrolysis at the electrodes leaves the soil unsaturated. More laboratory studies should be carried out under unsaturated conditions to understand electro-osmosis flow in unsaturated soil.
- (iii) Electro-osmosis is a complicated process involving electro-chemical reactions, and complex micro-structural behaviour of different clay minerals and chemical species under hydraulic, chemical and electrical gradients. For example, due to electrolysis at the electrodes, the pH value changes rapidly near the electrodes and this will affect the electro-osmosis permeability significantly. Therefore, a similar model should be developed for electro-osmosis consolidation to account for chemical species reaction and transport, in order to predict the modification of soil chemo-mechanical properties.

- (iv) The numerical model developed in this research assumes isothermal conditions. However, when current flows through the soil, thermal energy generated by resistive heating causes the soil temperature to rise. The magnitude of the heat energy generated is a function of the soil's electrical conductivity and the gradient of the electric potential. Although it is likely that heat could be dissipated quickly in a small scale laboratory test with limited current density, it is not true for field applications. Therefore, thermal effects should be accounted for in the numerical model.
- (v) Several changes in soil initial conditions (water content, initial stress, etc.), electrode spacing, processing time, levels of voltage or current, and optimization strategy can be examined through the numerical tool. Furthermore, numerical studies of electro-osmosis consolidation, combined with conventional consolidation techniques such as surcharge loading and vacuum preloading, are worth carrying out.

REFERENCES

- Abiera, H. O., Miura, N., Bergado, D. T., and Nomura, T. (1999). Effects of using electro-conductive pvd in the consolidation of reconstituted ariake clay. *Geotechnical Engineering*, 30(2):67–83.
- Alonso, E. E., Gens, A., and Josa, A. (1990). A constitutive model for partially saturated soils. *Géotechnique*, 40(3):405–430.
- Alshawabkeh, A. N. and Acar, Y. B. (1996). Electrokinetic remediation. ii: Theoretical model. *Journal of Geotechnical Engineering*, 122(3):186–196.
- Alshawabkeh, A. N. and Sheahan, T. C. (2003). Soft soil stabilisation by ionic injection under electric fields. *Ground Improvement*, 7(4):177–185.
- Andrade, J. E. and Borja, R. I. (2007). Modeling deformation banding in dense and loose fluid-saturated sands. *Finite Elements in Analysis and Design*, 43(5):361–383.
- Arnold, M. (1973). Laboratory determination of the coefficient of electro-osmotic permeability of soil. *Géotechnique*, 23:581–588.
- Asadi, A., Huat, B. B., Hassim, M., Mohamed, T. A., Hanafi, M. M., and Shariatmadari, N. (2009). Electroosmotic phenomena in organic soils. *American Journal of Environmental Sciences*, 5(3):310–314.
- Asavadorndeja, P. and Glawe, U. (2005). Electrokinetic strengthening of soft clay using the anode depolarization method. *Bulletin of Engineering Geology and the Environment*, 64(3):237–245.
- Bathe, K. J. (1996). *Finite Element Procedures*. Prentice Hall.
- Bergado, D. T., Balasubramaniam, A. S., Jonathan Fannin, R., and Holtz, R. D. (2002). Prefabricated vertical drains (pvd) in soft bangkok clay: A case study of the new bangkok international airport project. *Canadian Geotechnical Journal*, 39(2):304–315.
- Bergado, D. T., Sasanakul, I., and Horpibulsuk, S. (2003). Electro-osmotic consolidation of soft bangkok clay using copper and carbon electrodes with pvd. *Geotechnical Testing Journal*, 26(3):277–288.
- Biot, M. A. (1941). General theory of three-dimensional consolidation. *Journal of Applied Physics*, 12(2):155–164.
- Bjerrum, L., Moum, J., and Eide, O. (1967). Application of electro-osmosis to a foundation problem in a norwegian quick clay. *Géotechnique*, 17(3):214–235.

- Borja, R. I. and Alarcón, E. (1995). A mathematical framework for finite strain elasto-plastic consolidation part 1: Balance laws, variational formulation, and linearization. *Computer Methods in Applied Mechanics and Engineering*, 122(1-2):145–171.
- Borja, R. I., Tamagnini, C., and Alarcón, E. (1998). Elastoplastic consolidation at finite strain part 2: Finite element implementation and numerical examples. *Computer Methods in Applied Mechanics and Engineering*, 159(1-2):103–122.
- Burnotte, F., Lefebvre, G., and Grondin, G. (2004). A case record of electroosmotic consolidation of soft clay with improved soil-electrode contact. *Canadian Geotechnical Journal*, 41(6):1038–1053.
- Carter, J. P., Booker, J. R., and Small, J. C. (1979). Analysis of finite elasto-plastic consolidation. *International Journal for Numerical and Analytical Methods in Geomechanics*, 3(2):107–129.
- Carter, J. P., Small, J. C., and Booker, J. R. (1977). A theory of finite elastic consolidation. *International Journal of Solids and Structures*, 13(5):467–478.
- Casagrande, L. (1949). Electro-osmosis in soils. *Géotechnique*, 1(3):159–177.
- Casagrande, L. (1952). Electro-osmotic stabilization of soils. *Journal of the Boston Society of Civil Engineers*, 39(1):51–83.
- Casagrande, L. (1983). Stabilization of soils by means of electro-osmosis - state-of-the-art. *Journal of the Boston Society of Civil Engineers Section, American Society of Civil Engineers*, 69(2):255–302.
- Chang, J. H., Qiang, Z., and Huang, C. P. (2006). Remediation and stimulation of selected chlorinated organic solvents in unsaturated soil by a specific enhanced electrokinetics. *Colloids and Surfaces A: Physicochemical and Engineering Aspects*, 287(1-3):86–93.
- Chapman, D. L. (1913). Li. a contribution to the theory of electrocapillarity. *Philosophical Magazine Series 6*, 25(148):475–481.
- Chappell, B. A. and Burton, P. L. (1975). Electro-osmosis applied to unstable embankment. *ASCE J Geotech Eng Div*, 101(8):733–740.
- Chen, H., Mujumdar, A. S., and Raghavan, G. S. V. (1996). Laboratory experiments on electroosmotic dewatering of vegetable sludge and mine tailings. *Drying Technology*, 14(10):2435–2445.
- Chew, S. H., Karunaratne, G. P., Kuma, V. M., Lim, L. H., Toh, M. L., and Hee, A. M. (2004). A field trial for soft clay consolidation using electric vertical drains. *Geotextiles and Geomembranes*, 22(1):17–35.
- Chien, S. C. and Ou, C. Y. (2011). A novel technique of harmonic waves applied electro-osmotic chemical treatment for soil improvement. *Applied Clay Science*, 52(3):235–244.

- Chu, J., Yan, S. W., and Yang, H. (2000). Soil improvement by the vacuum preloading method for an oil storage station. *Géotechnique*, 50(6):625–632.
- Corapcioglu, M. Y. (1991). Formulation of electro-chemico-osmotic processes in soils. *Transport in porous media*, 6(4):435–444.
- De Borst, R., Crisfield, M. A., Remmers, J. J. C., and Verhoosel, C. V. (2012). *Nonlinear finite element analysis of solids and structures*. John Wiley & Sons.
- de Souza Neto, E. A., Peri, D., and Owen, D. R. J. (2008). *Computational methods for plasticity: theory and applications*. John Wiley & Sons, Ltd.
- Esrig, M. I. (1968). Pore pressures, consolidation and electrokinetics. *J. Soil Mech. Found. Div., Am. Soc. Civ. Eng.* 94(4 SM):899–921.
- Estabragh, A. R., Naseh, M., and Javadi, A. A. (2014). Improvement of clay soil by electro-osmosis technique. *Applied Clay Science*, 95:32–36.
- Feldkamp, J. R. and Belhomme, G. M. (1990). Large-strain electrokinetic consolidation: theory and experiment in one dimension. *Géotechnique*, 40(4):557–568.
- Fetzer, C. A. (1967). Electro-osmotic stabilization of west branch dam. *Journal of the Soil Mechanics and Foundations Division, ASCE*, 93(4):85–106.
- Fourie, A. B., Johns, D., and Jones, C. J. F. P. (2004). In-situ dewatering of mine tailings using electro-kinetic geosynthetics. In *Proceedings of the 11th International Conference on Tailings and Mine Waste, Colorado, USA*, pages 341–345, Colorado, USA.
- Fourie, A. B., Johns, D. G., and Jones, C. J. F. P. (2007). Dewatering of mine tailings using eletrokinetic geosynthetics. *Canadian Geotechnical Journal*, 44(2):160–172.
- Fourie, A. B. and Jones, C. J. F. P. (2010). Improved estimates of power consumption during dewatering of mine tailings using electrokinetic geosynthetics (ekgs). *Geotextiles and Geomembranes*, 28(2):181–190.
- Fourie, A. B., Pavlakis, J., and Jones, C. J. F. P. (2002). Stabilisation of mine tailings deposits using electro-kinetic geotextiles. In *Proceedings of the Seventh International Conference On Geosynthetics*, volume 3, pages 1031–1034.
- Gens, A. (2010). Soil-environment interactions in geotechnical engineering. *Geotechnique*, 60(1):3–74.
- Gens, A., Sánchez, M., and Sheng, D. (2006). On constitutive modelling of unsaturated soils. *Acta Geotechnica*, 1(3):137–147.
- Glendinning, S., Jones, C. J. F. P., and Pugh, R. C. (2005). Reinforced soil using cohesive fill and electrokinetic geosynthetics. *International Journal of Geomechanics*, 5(2):138–146.
- Glendinning, S., Lamont-Black, J., and Jones, C. J. F. P. (2007). Treatment of sewage sludge using electrokinetic geosynthetics. *Journal of Hazardous Materials*, 139(3):491–499.

- Glendinning, S., Lamont-Black, J., Jones, C. J. F. P., and Hall, J. (2008). Treatment of lagooned sewage sludge in situ using electrokinetic geosynthetics. *Geosynthetics International*, 15(3):192–204.
- Gouy, M. (1910). Sur la constitution de la charge électrique à la surface d'un électrolyte. *J. Phys. Theor. Appl.*, 9(1):457–468.
- Gray, D. H. (1970). Electrochemical hardening of clay soils. *Géotechnique*, 20(1):81–93.
- Hamir, R. B., Jones, C. J. F. P., and Clarke, B. G. (2001). Electrically conductive geosynthetics for consolidation and reinforced soil. *Geotextiles and Geomembranes*, 19(8):455–482.
- Hansbo, S., Jamiolkowski, M., and Kok, L. (1981). Consolidation by vertical drains. *Géotechnique*, 31(1):45–66.
- Hu, L. and Wu, H. (2014). Mathematical model of electro-osmotic consolidation for soft ground improvements. *Géotechnique*, 64(2):155–164.
- Hu, R., Chen, Y., and Zhou, C. (2011). Modeling of coupled deformation, water flow and gas transport in soil slopes subjected to rain infiltration. *Science China Technological Sciences*, 54(10):2561–2575.
- Indraratna, B., Rujikiatkamjorn, C., Ameratunga, J., and Boyle, P. (2011). Performance and prediction of vacuum combined surcharge consolidation at port of brisbane. *Journal of Geotechnical and Geoenvironmental Engineering*, 137(11):1009–1018.
- Iwata, M. and Jami, M. S. (2010). Analysis of combined electroosmotic dewatering and mechanical expression operation for enhancement of dewatering. *Drying Technology*, 28(7):881–889.
- Jommi, C. (2000). Remarks on the constitutive modelling of unsaturated soils. In Tarantino, A. and Mancuso, C., editors, *Experimental evidence and theoretical approaches in unsaturated soils*, pages 139–153, Rotterdam.
- Jones, C. J. F. P., Glendinning, S., Huntley, D. T., and Lamont-Black, J. (2006). Case history-in-situ dewatering of lagooned sewage sludge using electrokinetic geosynthetics (ekg). In *Geosynthetics. Proceedings of the 8th International Conference on Geosynthetics (8ICG)*, pages 539–542, Yokohama, Japan.
- Jones, C. J. F. P., Lamont-Black, J., and Glendinning, S. (2011). Electrokinetic geosynthetics in hydraulic applications. *Geotextiles and Geomembranes*, 29(4):381–390.
- Jones, C. J. F. P., Lamont-Black, J., Glendinning, S., Bergado, D., Eng, T., Fourie, A., et al. (2008). Recent research and applications in the use of electrokinetic geosynthetics. In *Proceedings of 4th Euro-Geo Conference*, number 329, Edinburgh, Scotland.
- Kaniraj, S. R., Huong, H. L., and Yee, J. H. S. (2011). Electro-osmotic consolidation studies on peat and clayey silt using electric vertical drain. *Geotechnical and Geological Engineering*, 29(3):277–295.

- Kaniraj, S. R. and Yee, J. H. S. (2011). Electro-osmotic consolidation experiments on an organic soil. *Geotechnical and Geological Engineering*, 29(4):505–518.
- Karunaratne, G. P. (2011). Prefabricated and electrical vertical drains for consolidation of soft clay. *Geotextiles and Geomembranes*, 29(4):391–401.
- Karunaratne, G. P., Chew, S. H., Lim, L. H., Toh, M. L., Poh, W. G., and Hee, A. M. (2002). Electroosmotic consolidation of soft clay based on laboratory and field trials. In *Proceedings of 7th International Conference on Geosynthetics, Nice*, volume 3, pages 1043–1046.
- Laloui, L., Klubertanz, G., and Vulliet, L. (2003). Solid-liquid-air coupling in multiphase porous media. *International Journal for Numerical and Analytical Methods in Geomechanics*, 27(3):183–206.
- Lamont-Black, J. (2001). Ekg: The next generation of geosynthetics. *Ground Engineering*, 34(10):22–23.
- Lamont-Black, J., Glendinning, S., Jones, C. J. F. P., Huntley, D., and Smith, R. (2005). The development of in-situ dewatering of lagooned sewage sludge using electrokinetic geosynthetics (ekg). In *Proceedings of Tenth European Bio-solids and Bio-wastes Conference*, pages 1–8.
- Lamont-Black, J., Hall, J. A., Glendinning, S., White, C. P., and Jones, C. J. F. P. (2012). Stabilization of a railway embankment using electrokinetic geosynthetics. *Geological Society Engineering Geology Special Publication*, 26(1):125–139.
- Lamont-Black, J. and Weltman, A. (2010). Electrokinetic strengthening and repair of slopes. *Ground Engineering April*, 43(4):28–31.
- Lefebvre, G. and Burnotte, F. (2002). Improvements of electroosmotic consolidation of soft clays by minimizing power loss at electrodes. *Canadian Geotechnical Journal*, 39(2):399–408.
- Lewis, R. W. and Garner, R. W. (1972). A finite element solution of coupled electrokinetic and hydrodynamic flow in porous media. *International Journal for Numerical Methods in Engineering*, 5(1):41–55.
- Lewis, R. W. and Humpheson, C. (1973). Numerical analysis of electro-osmotic flow in soils. *Journal of the Soil Mechanics and Foundations Division*, 99(8):603–616.
- Lewis, R. W. and Schrefler, B. A. (1998). *The finite element method in the static and dynamic deformation and consolidation of porous media*. John Wiley.
- Li, C., Borja, R. I., and Regueiro, R. A. (2004). Dynamics of porous media at finite strain. *Computer Methods in Applied Mechanics and Engineering*, 193(36-38):3837–3870.
- Liakopoulos, A. C. (1964). *Transient flow through unsaturated porous media*. PhD thesis, University of California, Berkeley.

- Liu, H.-l., Cui, Y.-l., Shen, Y., and Ding, X.-m. (2014). A new method of combination of electroosmosis, vacuum and surcharge preloading for soft ground improvement. *China Ocean Engineering*, 28:511–528.
- Lo, K. Y., Ho, K. S., and Inculet, I. I. (1991a). Field test of electroosmotic strengthening of soft sensitive clay. *Canadian Geotechnical Journal*, 28(1):74–83.
- Lo, K. Y., Inculet, I. I., and Ho, K. S. (1991b). Electroosmotic strengthening of soft sensitive clays. *Canadian Geotechnical Journal*, 28(1):62–73.
- Lo, K. Y., Micic, S., Shang, J. Q., Lee, Y. N., and Lee, S. W. (2000). Electrokinetic strengthening of a soft marine sediment. *International Journal of Offshore and Polar Engineering*, 10(2):137–144.
- Lockhart, N. C. (1983). Electroosmotic dewatering of clays. i. influence of voltage. *Colloids and Surfaces*, 6(3):229–238.
- Lockhart, N. C. (1992). Combined field dewatering: Bridging the science-industry gap. *Drying Technology*, 10(4):839–874.
- Lockhart, N. C. and Hart, G. H. (1988). Electro-osmotic dewatering of fine suspensions: The efficacy of current interruptions. *Drying Technology*, 6(3):415–423.
- Lockhart, N. C. and Stickland, R. E. (1984). Dewatering coal washery tailings ponds by electroosmosis. *Powder Technology*, 40(1-3):215–221.
- Mattson, E. D., Bowman, R. S., and Lindgren, E. R. (2002a). Electrokinetic ion transport through unsaturated soil: 1. theory, model development, and testing. *Journal of Contaminant Hydrology*, 54(1-2):99–120.
- Mattson, E. D., Bowman, R. S., and Lindgren, E. R. (2002b). Electrokinetic ion transport through unsaturated soil: 2. application to a heterogeneous field site. *Journal of Contaminant Hydrology*, 54(1-2):121–140.
- Meroi, E. A., Schrefler, B. A., and Zienkiewicz, O. C. (1995). Large strain static and dynamic semisaturated soil behaviour. *International Journal for Numerical and Analytical Methods in Geomechanics*, 19(2):81–106.
- Micic, S., Shang, J. Q., Lo, K. Y., Lee, Y. N., and Lee, S. W. (2001). Electrokinetic strengthening of a marine sediment using intermittent current. *Canadian Geotechnical Journal*, 38(2):287–302.
- Milligan, V. (1995). First application of electro-osmosis to improve friction pile capacity - three decades later. *Proceedings - ICE: Geotechnical Engineering*, 113(2):112–116.
- Mitchell, J. K. (1991). Conduction phenomena: from theory to geotechnical practice. *Géotechnique*, 41(3):299–340.
- Mitchell, J. K. (1993). *Fundamentals of Soil Behavior*. Wiley.
- Mitchell, J. K. and Soga, K. (2005). *Fundamentals of soil behavior*. John Wiley & Sons.

- Mohamedelhassan, E. and Shang, J. Q. (2001). Effects of electrode materials and current intermittence in electro-osmosis. *Ground Improvement*, 5(1):3–11.
- Mohamedelhassan, E. and Shang, J. Q. (2002). Feasibility assessment of electro-osmotic consolidation on marine sediment. *Ground Improvement*, 6(4):145–152.
- Nazem, M., Carter, J. P., Sheng, D., and Sloan, S. W. (2009). Alternative stress-integration schemes for large-deformation problems of solid mechanics. *Finite Elements in Analysis and Design*, 45(12):934–943.
- Nazem, M., Sheng, D., and Carter, J. P. (2006). Stress integration and mesh refinement for large deformation in geomechanics. *International Journal for Numerical Methods in Engineering*, 65(7):1002–1027.
- Nazem, M., Sheng, D., Carter, J. P., and Sloan, S. W. (2008). Arbitrary lagrangian-eulerian method for large-strain consolidation problems. *International Journal for Numerical and Analytical Methods in Geomechanics*, 32(9):1023–1050.
- Nettleton, I. M., Jones, C. J. F. P., Clarke, B. G., and Hamir, R. (1998). Electrokinetic geosynthetics and their applications. In *The Sixth International Conference on Geosynthetics*, pages 871–876, Atlanta, USA.
- Nicholls, R. L. and Herbst, R. L. (1967). Consolidation under electrical-pressure gradients. *Journal of the Soil Mechanics and Foundations Division*, 93(SM5):139–151.
- Nuth, M. and Laloui, L. (2008). Effective stress concept in unsaturated soils: Clarification and validation of a unified framework. *International Journal for Numerical and Analytical Methods in Geomechanics*, 32(7):771–801.
- Ou, C. Y., Chien, S. C., and Chang, H. H. (2009). Soil improvement using electroosmosis with the injection of chemical solutions: Field tests. *Canadian Geotechnical Journal*, 46(6):727–733.
- Prévost, J. H. (1980). Mechanics of continuous porous media. *International Journal of Engineering Science*, 18(6):787–800.
- Prévost, J. H. (1982). Nonlinear transient phenomena in saturated porous media. *Computer Methods in Applied Mechanics and Engineering*, 30(1):3–18.
- Rittirong, A. and Shang, J. Q. (2008). Numerical analysis for electro-osmotic consolidation in two-dimensional electric field. In *Proceedings of the International Offshore and Polar Engineering Conference*, pages 566–572.
- Roscoe, K. H. and Burland, J. B. (1968). On the generalized stress-strain behaviour of 'wet' clay. *Engineering Plasticity*, pages 535–609.
- Roscoe, K. H., Schofield, A. N., and Thurairajah, A. (1963). Yielding of clays in states wetter than critical. *Géotechnique*, 13(3):211–240.

- Sanavia, L., Schrefler, B. A., and Steinmann, P. (2002). A formulation for an unsaturated porous medium undergoing large inelastic strains. *Computational Mechanics*, 28(2):137–151.
- Schrefler, B. A. and Scotta, R. (2001). A fully coupled dynamic model for two-phase fluid flow in deformable porous media. *Computer Methods in Applied Mechanics and Engineering*, 190(24-25):3223–3246.
- Schrefler, B. A. and Zhan, X. Y. (1993). A fully coupled model for water flow and airflow in deformable porous media. *Water Resources Research*, 29(1):155–167.
- Segall, B. A. and Bruell, C. J. (1992). Electroosmotic contaminant-removal processes. *Journal of Environmental Engineering*, 118(1):84–100.
- Shang, J. Q. (1997a). Electrokinetic dewatering of clay slurries as engineered soil covers. *Canadian Geotechnical Journal*, 34(1):78–86.
- Shang, J. Q. (1997b). Zeta potential and electroosmotic permeability of clay soils. *Canadian Geotechnical Journal*, 34(4):627–631.
- Shang, J. Q. (1998a). Electroosmosis-enhanced preloading consolidation via vertical drains. *Canadian Geotechnical Journal*, 35(3):491–499.
- Shang, J. Q. (1998b). Two-dimensional electro-osmotic consolidation. *Ground Improvement*, 2(1):17–25.
- Shang, J. Q. and Lo, K. Y. (1997). Electrokinetic dewatering of a phosphate clay. *Journal of Hazardous Materials*, 55(1-3):117–133.
- Shang, J. Q., Lo, K. Y., and Huang, K. M. (1996). On factors influencing electro-osmotic consolidation. *Geotechnical Engineering*, 27(2):23–36.
- Shang, J. Q., Tang, M., and Miao, Z. (1998). Vacuum preloading consolidation of reclaimed land: A case study. *Canadian Geotechnical Journal*, 35(5):740–749.
- Sheng, D., Gens, A., Fredlund, D. G., and Sloan, S. W. (2008). Unsaturated soils: From constitutive modelling to numerical algorithms. *Computers and Geotechnics*, 35(6):810–824.
- Sheng, D. and Sloan, S. W. (2003). Time stepping schemes for coupled displacement and pore pressure analysis. *Computational Mechanics*, 31(1-2 SPEC.):122–134.
- Sheng, D., Sloan, S. W., Gens, A., and Smith, D. W. (2003a). Finite element formulation and algorithms for unsaturated soils. part i: Theory. *International Journal for Numerical and Analytical Methods in Geomechanics*, 27(9):745–765.
- Sheng, D., Smith, D. W., Sloan, S. W., and Gens, A. (2003b). Finite element formulation and algorithms for unsaturated soils. part ii: Verification and application. *International Journal for Numerical and Analytical Methods in Geomechanics*, 27(9):767–790.

- Smith, I. M. and Griffiths, D. V. (2004). *Programming the Finite Element Method*. John Wiley & Sons.
- Smoluchowski, M. (1921). Elektrische endosmose und stromungsströme. *Handbuch der Elektrizität und des Magnetismus*.
- Soderman, L. G. and Milligan, V. (1961). Capacity of friction piles in varved clay increased by electro-osmosis. In *Proceedings of the 5th International Conference on Soil Mechanics and Foundation Engineering*, volume 2, pages 143–147.
- Solowski, W. T. and Gallipoli, D. (2010). Explicit stress integration with error control for the barcelona basic model. part i: Algorithms formulations. *Computers and Geotechnics*, 37(1-2):59–67.
- Sprute, R. H. and Kelsh, D. J. (1976). *Dewatering and densification of coal waste by direct current-laboratory tests*. Report of investigations Bureau of Mines. US Department of the Interior, Bureau of Mines.
- Sprute, R. H., Kelsh, D. J., and Thompson, S. L. (1982). *Electrokinetic Densification of Solids in a Coal Mine Sediment Pond: A Feasibility Study*. US Department of the Interior, Bureau of Mines.
- Stanczyk, M. H. and Feld, I. L. (1964). *Electro-dewatering tests of Florida phosphate rock slime*. US Department of the Interior, Bureau of Mines.
- Stern, O. (1924). The theory of the electrolytic double-layer. *Zeit. Elektrochem*, 30:508–516.
- Tamagnini, C., Jommi, C., and Cattaneo, F. (2010). A model for coupled electro-hydro-mechanical processes in fine grained soils accounting for gas generation and transport. *Anais da Academia Brasileira de Ciencias*, 82(1):169–193.
- Uzuoka, R. and Borja, R. I. (2012). Dynamics of unsaturated poroelastic solids at finite strain. *International Journal for Numerical and Analytical Methods in Geomechanics*, 36(13):1535–1573.
- Van Gassen, W. and Sego, D. C. (1991). Electro-osmosis in a frozen soil. *Cold regions science and technology*, 19(3):253–259.
- Van Genuchten, M. T. (1980). Closed-form equation for predicting the hydraulic conductivity of unsaturated soils. *Soil Science Society of America Journal*, 44(5):892–898.
- Veal, C., Johnston, B., and Miller, S. (2000). The electroosmotic dewatering (eod) of mine tailings. In *Proceedings of the 14th Annual Conference of the American Filtration and Separations Society*, pages 14–16.
- Von Helmholtz, H. (1879). *Studien über elektrische Grenzschichten*.
- Wan, T. and Mitchell, J. K. (1976). Electroosmotic consolidation of soils. *J. Geotech. Eng. Div.*, 101(5):503–507.

- West, L. J. and Stewart, D. I. (2000). Effect of zeta potential on soil electrokinesis. In *Geoenvironment 2000: Characterization, Containment, Remediation, and Performance in Environmental Geotechnics*, pages 1535–1549. ASCE.
- Wieczorek, S., Weigand, H., Schmid, M., and Marb, C. (2005). Electrokinetic remediation of an electroplating site: Design and scale-up for an in-situ application in the unsaturated zone. *Engineering Geology*, 77(3-4 SPEC. ISS.):203–215.
- Yuan, J. and Hicks, M. A. (2013). Large deformation elastic electro-osmosis consolidation of clays. *Computers and Geotechnics*, 54:60–68.
- Yuan, J. and Hicks, M. A. (2014). Numerical modelling of electro-osmosis consolidation of unsaturated clay at large strain. In *Numerical Methods in Geotechnical Engineering - Proceedings of the 8th European Conference on Numerical Methods in Geotechnical Engineering, NUMGE 2014*, volume 2, pages 1061–1066.
- Yuan, J. and Hicks, M. A. (2015). Numerical simulation of elasto-plastic electro-osmosis consolidation at large strain. *Acta Geotechnica*, 10. (Inpress).
- Yuan, J., Hicks, M. A., and Dijkstra, J. (2012). Multi-dimensional electro-osmosis consolidation of clays. In *Proceedings of the International Symposium on Ground Improvement*, volume 2, pages 241–248.
- Yuan, J., Hicks, M. A., and Dijkstra, J. (2013). Numerical model of elasto-plastic electro-osmosis consolidation of clays. In *Poromechanics V - Proceedings of the 5th Biot Conference on Poromechanics*, pages 2076–2085.
- Zienkiewicz, O. C. and Shiomi, T. (1984). Dynamic behaviour of saturated porous media: The generalized biot formulation and its numerical solution. *International Journal for Numerical and Analytical Methods in Geomechanics*, 8(1):71–96.

A

**MATRICES AND VECTORS FOR
LARGE STRAIN FORMULATIONS**

For two dimensional plane strain, the shape function related matrices at the i th node in a finite element are defined as

$$\mathbf{N}_L = \begin{bmatrix} N_i & 0 \\ 0 & N_i \end{bmatrix} \quad (\text{A.1})$$

$$\mathbf{B}_L = \begin{bmatrix} \frac{\partial N_i}{\partial x} & 0 \\ 0 & \frac{\partial N_i}{\partial y} \\ \frac{\partial N_i}{\partial y} & \frac{\partial N_i}{\partial x} \end{bmatrix} \quad (\text{A.2})$$

$$\mathbf{B}_{NL} = \begin{bmatrix} \frac{\partial N_i}{\partial x} & 0 \\ \frac{\partial N_i}{\partial y} & 0 \\ 0 & \frac{\partial N_i}{\partial x} \\ 0 & \frac{\partial N_i}{\partial y} \end{bmatrix} \quad (\text{A.3})$$

$$\tilde{\mathbf{B}}_L = \begin{bmatrix} 0 & 0 \\ 0 & 0 \\ \frac{1}{2} \frac{\partial N_i}{\partial y} & -\frac{1}{2} \frac{\partial N_i}{\partial x} \end{bmatrix} \quad (\text{A.4})$$

The stress matrices for geometric stiffness are defined as

$$\hat{\boldsymbol{\sigma}} = \begin{bmatrix} \sigma'_{11} & \sigma'_{12} & 0 & 0 \\ \sigma'_{21} & \sigma'_{22} & 0 & 0 \\ 0 & 0 & \sigma'_{11} & \sigma'_{12} \\ 0 & 0 & \sigma'_{21} & \sigma'_{22} \end{bmatrix} \quad (\text{A.5})$$

$$\tilde{\boldsymbol{\sigma}} = \begin{bmatrix} 2\sigma'_{11} & 0 & 2\sigma'_{12} \\ 0 & 2\sigma'_{22} & -2\sigma'_{12} \\ \sigma'_{12} & \sigma'_{12} & \sigma'_{22} - \sigma'_{11} \end{bmatrix} \quad (\text{A.6})$$

$$\mathbf{p} = \begin{bmatrix} p & 0 & 0 & 0 \\ 0 & p & 0 & 0 \\ 0 & 0 & p & 0 \\ 0 & 0 & 0 & p \end{bmatrix} \quad (\text{A.7})$$

The internal nodal force vector, used in the Newton–Raphson iteration, is given by

$$\mathbf{F}^{int} = \int_{V^t} \mathbf{B}_L^T \boldsymbol{\sigma}' dV^t + \int_{V^t} \mathbf{B}_L^T \mathbf{I} p dV^t \quad (\text{A.8})$$

B

COEFFICIENT MATRICES AND LOAD VECTORS

The coefficient matrices in the set of discretized governing equations, Eq. 5.55, are defined as follows:

$$\mathbf{K}_{nl} = \int_V \mathbf{B}_L^T \mathbf{D}_{ep} \mathbf{B}_L dV + \int_V \mathbf{B}_L^T \bar{\boldsymbol{\sigma}} \bar{\mathbf{B}}_L dV + \int_V \mathbf{B}_{NL}^T \bar{\mathbf{p}} \mathbf{B}_{NL} dV + \int_V \mathbf{B}_{NL}^T \hat{\boldsymbol{\sigma}} \mathbf{B}_{NL} dV \quad (\text{B.1})$$

$$\mathbf{C}_{sw} = \int_V \mathbf{B}_L^T S_w \mathbf{I} \mathbf{N}_w dV - \int_V \mathbf{B}_L^T \mathbf{W}_{ep} \mathbf{N}_w dV \quad (\text{B.2})$$

$$\mathbf{C}_{sg} = \int_V \mathbf{B}_L^T (1 - S_w) \mathbf{I} \mathbf{N}_g dV + \int_V \mathbf{B}_L^T \mathbf{W}_{ep} \mathbf{N}_g dV \quad (\text{B.3})$$

$$\mathbf{C}_{ws} = \int_V \mathbf{N}_w^T S_w \mathbf{I}^T \mathbf{B}_L dV \quad (\text{B.4})$$

$$\mathbf{C}_{ww} = \int_V \mathbf{N}_w^T \left(\frac{n S_w}{K_w} - n \frac{\partial S_w}{\partial s} \right) \mathbf{N}_w dV \quad (\text{B.5})$$

$$\mathbf{C}_{wg} = \int_V \mathbf{N}_w^T \left(n \frac{\partial S_w}{\partial s} \right) \mathbf{N}_g dV \quad (\text{B.6})$$

$$\mathbf{K}_{ww} = \int_V (\nabla \mathbf{N}_w)^T \left(\frac{\mathbf{k}_w k_{rw}}{\gamma_w} \right) \nabla \mathbf{N}_w dV \quad (\text{B.7})$$

$$\mathbf{K}_{eo} = \int_V (\nabla \mathbf{N}_w)^T \mathbf{k}_{eo} k_{reo} \nabla \mathbf{N}_v dV \quad (\text{B.8})$$

$$\mathbf{C}_{gs} = \int_V \mathbf{N}_g^T (1 - S_w) \mathbf{I}^T \mathbf{B}_L dV \quad (\text{B.9})$$

$$\mathbf{C}_{gg} = \int_V \mathbf{N}_g^T \left(\frac{n(1 - S_w)}{K_g} - n \frac{\partial S_w}{\partial s} \right) \mathbf{N}_g dV \quad (\text{B.10})$$

$$\mathbf{K}_{gg} = \int_V (\nabla \mathbf{N}_g)^T \left(\frac{\mathbf{k}_g k_{rg}}{\gamma_g} \right) \nabla \mathbf{N}_g dV \quad (\text{B.11})$$

$$\mathbf{K}_{\sigma e} = \int_V (\nabla \mathbf{N}_v)^T \mathbf{k}_{\sigma e} \nabla \mathbf{N}_v dV \quad (\text{B.12})$$

$$\mathbf{F}^{ext} = \int_S \mathbf{N}_u^T \mathbf{t} dS + \int_V \mathbf{N}_u^T \mathbf{b} dV \quad (\text{B.13})$$

$$\mathbf{Q}_w^{ext} = \int_S \mathbf{N}_w^T \mathbf{q}_w dS + \int_V (\nabla \mathbf{N}_w)^T \frac{\mathbf{k}_w k_{rw}}{\gamma_w} \rho^w \mathbf{g} dV \quad (\text{B.14})$$

$$\mathbf{Q}_g^{ext} = \int_S \mathbf{N}_g^T \mathbf{q}_g dS + \int_V (\nabla \mathbf{N}_g)^T \frac{\mathbf{k}_g k_{rg}}{\gamma_g} \rho^g \mathbf{g} dV \quad (\text{B.15})$$

$$\mathbf{Q}_V^{ext} = \int_S \mathbf{N}_v^T \mathbf{q}_e dS \quad (\text{B.16})$$

SUMMARY

Consolidation of soft clay creates a lot of problems in foundation engineering, because of the very low clay permeability and high compressibility. Primary consolidation takes a long time to complete if the material is left consolidating under atmospheric evaporation, and traditional dewatering techniques, such as surcharge preloading, vacuum preloading or vertical drains, have been used for decades to shorten the consolidation time. Among new soft ground improvement technologies, electro-osmosis consolidation is receiving much attention as a possible time efficient solution. Electro-osmosis is a novel technique to consolidate soft clays, and involves the flow of pore fluid in a soil mass in response to an applied electrical field. The electrodes (positive and negative) are installed in pairs in the soil mass; the direct current then forces ions in the mobile part of the electric double layer (EDL) to move from the anode towards the cathode, causing water flow. Electro-osmosis is found to be more effective in clayey soils because the electro-osmosis permeability is independent of the grain size. This means that electro-osmosis can generate flow rates that are 100 to 1000 times greater than hydraulic flows in fine grained soft clays.

The purpose of this thesis is to develop a numerical model for simulating multi-dimensional and fully coupled multi-physics electro-osmosis consolidation, including the elasto-plastic behaviour of soil and time dependent transport parameters at large strain. Special attention is paid to the simulation of complicated geometries and boundary conditions, and to the inclusion of more advanced elasto-plastic constitutive models. The overall goal is to develop a more realistic numerical tool which addresses the main features of electro-osmosis consolidation, and that has potential use in the design and optimization of field applications.

In this thesis, numerical models for the electro-osmosis consolidation of soft clays in multi-dimensional domains at large strain are presented, which consider the full coupling of the soil mechanical behaviour, pore water transport, pore gas transport and electric flow. In particular, elasto-plastic constitutive models (i.e. the Modified Cam Clay model and Barcelona Basic Model) are employed to describe the mechanical behaviour of the clay, and some empirical expressions are employed to describe the non-linear transport parameters. The proposed models have been verified against analytical/numerical solutions and also evaluated with results obtained from laboratory experiments. Overall, excellent agreement has been found, which demonstrates the accuracy and efficiency of the proposed models. Updated Lagrangian formulations are employed to account for the geometric nonlinearity. The importance of considering large strains in a consistent and proper way is demonstrated, and differences with models based on small strain theory are highlighted.

As deformation is the key concern during consolidation behaviour, various numerical examples are investigated to study the deformation characteristics. The ratio of electro-osmosis permeability to hydraulic permeability k_{eo}/k_w is a key factor in electro-

osmosis consolidation. Generally, electro-osmosis permeability and hydraulic permeability decrease with a decrease in the void ratio and degree of water saturation, but the decrease in hydraulic conductivity is much faster than the decrease of electro-osmosis permeability, so the ratio k_{eo}/k_w increases during the consolidation process. A field test of electro-osmosis consolidation has been analysed, showing excellent agreement between the computed and measured settlements. Various electrode configurations, as well as current intermittence and current reversal approaches for electro-osmosis consolidation have also been investigated using the proposed model.

The particular contribution of this thesis is that it introduces a realistic numerical tool for the simulation of electro-osmosis consolidation. It is able to simulate field applications with complicated boundary and geometry conditions, as well as practical applications such as current intermittence and polarity reversal, which are often employed in the field to achieve efficient and economical consolidation. Feasibility studies and a proper design are important for the field application of electro-osmosis consolidation. Hence this numerical tool has potential use in the design and analysis of electro-osmosis consolidation, including the assessment of factors for achieving optimal dewatering effects and estimating the cost.

SAMENVATTING

De consolidatie van slappe klei kan tot problemen leiden in de funderingstechniek. Dit komt omdat klei een zeer lage doorlatendheid en een hoge samendrukbaarheid heeft. Primaire consolidatie duurt erg lang als het materiaal alleen consolideert onder atmosferische druk. Om dit proces te versnellen wordt al jarenlang gebruik gemaakt van verschillende ontwateringstechnieken zoals voorbelasten met een bovenbelasting of vacuüm consolidatie en verticale drains. Onder de nieuwste technologieën voor grondverbetering van slappe grond, wordt electro-osmose consolidatie gezien als een veelbelovende tijd besparende oplossing. Elektro-osmose is een nieuwe techniek om slappe klei te consolideren door poriënvloeistof in de ondergrond te laten stromen door een elektrisch veld toe te passen. De elektroden (positief en negatief) zijn als paren in de bodem geïnstalleerd. Door gelijkstroom verplaatsen de ionen in het mobiele gedeelte van de elektrische dubbele laag (EDL) van de anode naar de kathode waardoor het water gaat stromen. Elektro-osmose is erg effectief in kleilagen omdat de doorlatendheid door elektro-osmose los staat van de korrelgrootte. Hierdoor kan elektro-osmose een 100 tot 1000 keer grotere stroming genereren dan grondwaterstroming in slappe klei.

Het doel van deze thesis is om een numeriek model te ontwikkelen om multidimensionaal en volledig gekoppelde multi-fysische electro-osmose consolidatie te simuleren, inclusief het elasto-plastisch gedrag van de ondergrond en de tijdsafhankelijke transportparameters bij grote vervormingen. Speciale aandacht is besteed aan de simulatie van ingewikkelde geometrieën, grenswaarden en meer geavanceerde elasto-plastische constitutieve modellen. Het algemene doel is om een realistischer numeriek model te ontwikkelen dat de belangrijkste kenmerken van elektro-osmose consolidatie bevat en potentieel gebruikt kan worden voor het ontwerp en optimalisatie van toepassingen in de praktijk.

In deze thesis worden numerieke modellen gepresenteerd voor elektro-osmose consolidatie van slappe klei in multidimensionale domeinen onder hoge belasting. Deze modellen bevatten een volledige koppeling van het mechanische gedrag van de ondergrond, transport van poriënwater en -gas, en elektrische stroming. In het bijzonder zijn elasto-plastische constitutieve modellen (zoals het Modified Cam Clay Model en het Barcelona Basic Model) gebruikt om het mechanische gedrag van klei te beschrijven. Ook zijn empirische relaties gebruikt om niet-lineaire transport parameters te beschrijven. De voorgestelde modellen zijn gevalideerd tegen analytische/numerieke oplossingen en vergeleken met resultaten uit laboratoriumexperimenten. De uitstekende overeenkomsten tonen de nauwkeurigheid en efficiëntie van de voorgestelde modellen. Aangepaste Lagrangian formuleringen worden gebruikt om rekening te houden met geometrische niet-lineariteit. Er wordt aangetoond dat het belangrijk is om grote rekken consistent en realistisch te beschouwen en verschillen met modellen gebaseerd op de veronderstelling van kleine rekken worden belicht.

Omdat vervorming een essentiële zorg is tijdens consolidatie zijn er verscheidene

numerieke voorbeelden onderzocht om vervormingskarakteristieken te bestuderen. De ratio van elektro-osmose permeabiliteit en hydraulische permeabiliteit k_{eo}/k_w blijkt een sleutelfactor in elektro-osmose consolidatie. Normaal nemen elektro-osmose doorlatendheid en hydraulische doorlatendheid af met afnemend poriëngetal en verzadigingsgraad, maar omdat de hydraulische geleidbaarheid veel sneller afneemt dan de elektro-osmose doorlatendheid neemt de k_{eo}/k_w ratio toe tijdens consolidatie. Een veldproef van elektro-osmose consolidatie is geanalyseerd en laat uitstekende overeenkomsten zien tussen de berekende en afgemeten zettingen. Tevens zijn verschillende elektrode configuraties zoals geschakelde stroom en ompoling onderzocht met het voorgestelde model.

De bijdrage van deze thesis is dat het een realistisch numeriek model presenteert voor de simulatie van electro-osmose consolidatie. Met dit model is het mogelijk om toepassingen in de praktijk te simuleren met complexe grensvoorwaarden en geometrieën, en daarnaast ook praktische applicaties zoals welke vaak toegepast worden in de praktijk voor efficiënte en economische consolidatie. Haalbaarheidsstudies en een goed ontwerp zijn belangrijk voor het toepassen van electro-osmose consolidatie in het veld. Daarom heeft dit numeriek model de potentie om gebruikt te worden voor het ontwerp en de analyse van electro-osmose consolidatie. Tevens kan het model gebruikt worden voor onderzoek naar optimalisatie van het consolidatieproces en het schatten van kosten.

ACKNOWLEDGMENTS

The completion of my PhD dissertation has been a long journey. I have thoroughly enjoyed my life during this journey. I want to express my gratitude to all the people who made it possible for me to accomplish this dissertation and who made my stay in Delft very pleasant.

First and foremost, I would like to express my gratitude to my supervisor, Prof. Michael Hicks, whose expertise, understanding, and patience, added considerably to my PhD research. Michael, it has been a great pleasure to work with you; thanks for bringing me into the research field and offering me this challenging but great opportunity. Thank you for being so patient and dedicated for every meeting, spending countless time to revise my papers and dissertation and helping me to stay focused on the target of my research.

Besides my supervisor, I would like to thank my other committee members: Prof. Cristina Jommi, Prof. Timo Heimovaara, Prof. Bert Sluys, Prof. Tom Scarpas, Prof. Kenichi Soga and Prof. Claudio Tamagnini, for their insightful feedback and encouragement.

Sincerely thanks to TU Delft and the China Scholarship Council for their financial support of this PhD research.

My sincere thanks also goes to Dr. Phil Vardon, who provided me with the opportunity to continue my research in TU Delft as a Postdoc. I would also like to appreciate the assistance and support from my current and former colleagues in the Geo-Engineering Section: Patrick Arnold, Jelke Dijkstra, Yajun Li, Kang Liu, Rui Rui, Shuhong Tan, Bin Wang, Yutian Yao, Hongfen Zhao and others. I thank my fellow officemates: Michael Afanasyev, Shirishkavar Baviskar, Laura Konstantaki, Andre van Turnhout, Andriy Bun and Poly Buragohain. It was my pleasure to share the office with you all and I am very grateful for your help and kindness. Andriy and Sabrina, thanks for your help with the Dutch translation.

During these years in the Netherlands I met great people who shared special times with me: Mingliang Li, Junchao Shi, Hua Zhong, Wenchao Wang, Sizhu Zhang, Changyun Wei, Tao Hong, Yongjia Li, Yinfu Jin, Zhe Zhang, Wei Zhu, Ke Xu, Yunhe Zhang, Shuai Li, Jiakun Gong and others. I want to give my thanks to all the DCF team-mates; we shared pleasurable times on the pitch after work.

Last but not the least, I would like to express my faithful thanks to my parents, brother and my lovely little niece. Without your support I would not have been able to do this. Special thanks goes to my dear Lei. I feel very lucky to have you in my life; thanks for your understanding, encouragement and endless support.

Jiao Yuan

CURRICULUM VITÆ

Jiao Yuan was born on October 9, 1985 in Hunan province. In 2004, he started studying Water Conservancy and Hydro-power Engineering at Changsha University of Science & Technology in Changsha, China and obtained his Bachelor degree in 2008. After that he moved to Nanjing to continue his study in Hydraulic Structure Engineering at Hohai University and received his master degree in 2010. In December 2010 he received funding from the China Scholarship Council and started working as a PhD researcher in the Geo-Engineering section at TU Delft following the guidance of Prof. Michael Hicks. The results of his work on the large strain numerical modelling of electro-osmosis consolidation are described in this thesis. Since December 2014, he has been working as a researcher in the same section at TU Delft.

LIST OF PUBLICATIONS

JOURNAL PUBLICATIONS

1. **Yuan, J.**, Hicks, M. A., 2013. Large deformation elastic electro-osmosis consolidation of clays. *Computers and Geotechnics*. 54: 60-68. DOI: 10.1016/j.compgeo.2013.05.012
2. **Yuan, J.**, Hicks, M. A., 2015. Numerical simulation of elasto-plastic electro-osmosis consolidation at large strain. *Acta Geotechnica*. DOI: 10.1007/s1140-015-0366-z
3. **Yuan, J.**, Hicks, M. A., 2015. Numerical analysis of electro-osmosis consolidation: a case study. *Geotechnique Letters*. 5(July–September): 147-152. DOI: 10.1680/geolett.15.00045
4. **Yuan, J.**, Hicks, M. A., Large strain elasto-plastic electro-osmosis consolidation of unsaturated clays. (*International Journal for Numerical and Analytical Methods in Geomechanics*, under review).
5. **Yuan, J.**, Hicks, M. A., Numerical evaluation of optimal approaches for electro-osmosis consolidation. (ready to submit).

CONFERENCE PUBLICATIONS

1. **Yuan, J.**, Hicks, M. A., Dijkstra, J., 2012. Multi-dimensional electro-osmosis consolidation of clays. In N., Denies & N., Huybrechts (Eds.), *Recent Research Advances & Execution Aspects of Ground Improvement Works* (pp. 241-248). Brussel: ISS-MGE Technical Committee TC 211.
2. **Yuan, J.**, Hicks, M. A., Dijkstra, J., 2013. Numerical model of elasto-plastic electro-osmosis consolidation of clays. In Hellmich, C., Pichler, B., & Adam, D. (Eds.), *Proceedings of the 5th Biot conference on poromechanics* (pp. 2076-2085). Reston: ASCE.
3. **Yuan, J.**, Hicks, M. A., 2014. Numerical modelling of electro-osmosis consolidation of unsaturated clay at large strain. In Hicks, M. A., Brinkgreve, R. B. J., & Rohe, A. (Eds.), *Proceedings of the 8th European conference on numerical methods in geotechnical engineering* (pp. 1061-1066). London: Taylor & Francis Group.
4. **Yuan, J.**, Hicks, M. A., Jommi, C., 2015. Large strain consolidation of clays: numerical comparison between evaporation and electro-osmosis dewatering. In Oka, E., Uzuoka, R., & Kimoto, S. (Eds.), *Proceedings of the 14th International Conference of the International Association for Computer Methods and Advances in Geomechanics* (pp. 1655-1660). London: Taylor & Francis Group.

